OPTIMAL PROCESSING OF IMPULSE RADAR SIGNALS FOR BRIDGE DECK INSPECTION

By

ZHIJIAN HU, B.Sc., M.Eng.

A Thesis
Submitted to the School of Graduate Studies
in Partial Fulfilment of the Requirements
for the Degree
Doctor of Philosophy

McMaster University

May 1993

OPTIMAL PROCESSING OF IMPULSE RADAR SIGNALS

FOR BRIDGE DECK INSPECTION

DOCTOR OF PHILOSOPHY (1993)
(Electrical and Computer Engineering)

McMASTER UNIVERSITY
Hamilton, Ontario, Canada

TITLE: **Optimal Processing of Impulse Radar Signals for Bridge Deck Inspection**

AUTHOR: Zhijian Hu

B. Sc. (Fudan University)
M. Eng. (McMaster University)

SUPERVISORS: Professor Charles R. Carter
Department of Electrical and Computer Engineering

Professor Kon Max Wong
Department of Electrical and Computer Engineering

NUMBER OF PAGES: xiii, 153

Abstract

Impulse radar possesses some attractive features that make it particularly useful in probing objects that are buried, encased in other materials or structures. Testing has demonstrated its potential in the detection of deterioration in concrete bridge deck slabs that are covered with bituminous surfacing. In order to benefit fully from using impulse radar in the bridge deck inspection, however, it is necessary to take advantage of the progress in signal processing techniques. This thesis is an attempt to provide a comprehensive treatment of the optimal extraction of information from the reflected radar signals, as to determine the subsurface structure and condition of the bridge decks. Generally, it follows a statistical estimation approach to the problem.

In the thesis, a parametric representation is derived to approximate the radar-generated pulses for probing. The asphalt-covered bridge decks are regarded as a system of stratified, lossless, and horizontally layered media with each layer being homogeneous and isotropic. The propagation of electromagnetic waves in such a multi-layered media system can be completely determined by a set of characteristic parameters of the media. Under such assumptions, the reflected radar signals may be well described by a delayed sum model which is specified by the characteristic parameters of the media.

Based upon the parametric signal model, a maximum likelihood estimator is formulated to determine the parameters of reflected signals. Computer experiments show that the ML estimation is capable of resolving closely spaced returns in the received signal and producing very accurate parameter estimates. ML estimation of real radar signals reflected from a bridge deck is also performed with success. However, to carry out the ML estimation requires an explicit knowledge of the probability density function of received signal which may not be always available. Moreover, the search for the ML estimates usually involves a global, nonlinear optimization procedure which can be extremely costly in computation time.

To overcome the difficulties with the ML method, a new eigenstructure-based (EB) method for parameter estimation is developed in this thesis. The implementation of the new estimation method requires only the autocovariance of the reflected signal, and it is more efficient in computation than the ML method. Computer simulation demonstrates that the EB method results in very satisfactory estimates at high SNR levels, but it becomes inaccurate when the SNR level is low or the radar returns in the received signal are very close spaced in time.

The error performances of the parameter estimators under various conditions are evaluated and compared via computer simulation. A detailed analysis of the Cramér-Rao Lower Bound on the estimation error is performed to gain an insight into how various factors affect the estimation performance.

An alternative to the parameter estimation approach is predictive deconvolution which is developed on a nonparametric model of the reflected signals. In principle, it is an application of Wiener optimal filtering theory to the deconvolution problem. It is observed in Computer simulation that predictive deconvolution is able to resolve returns closely located in time. Its implementation is carried out by simply solving a set of linear, normal equations, and its operation involves only straightforward linear filtering which demands little computation. However, the performance of predictive deconvolution deteriorates quickly in the presence of even a moderate level of noise in the input signal. This weakness may severely restrict its usefulness in practice.

Acknowledgement

The author wishes to express his deep gratitude to Professor C. R. Carter for his constant guidance, support, patience and encouragement throughout the course of this work.

The author is equally indebted to Professor K. M. Wong for his valuable advice and constructive criticisms during the development of this thesis.

Professors P. C. Yip, W. S. F. Poehlman and J. P. Reilly have served on author's supervisory committee and offered many valuable comments on this work. Their time and efforts are sincerely appreciated.

The author is also very grateful to Q. T. Zhang, J. Qu, X Huang, T. Chung and N. Stralen, as well as many other researchers and fellow graduate students in the Communications Research Laboratory, for providing stimulating discussions, helpful suggestions and generous assistance.

Many thanks are due to J. Chen too, for his help in printing this thesis.

Contents

List of Figures

List of Tables

Chapter 1

Introduction

1.1 Impulse Radar for Bridge Deck Inspection

Impulse radar has been used in a wide variety of applications [Daniel, 1988], such as investigating geological structures, locating underground cables and utility pipes, measuring ice thickness, and detecting buried organic objects. Test results also demonstrated the capability of impulse radar to evaluate the subsurface condition of concrete bridge deck slabs that are covered with bituminous surfacing [Carter, 1986].

The bridge decks are of multi-layer structure, and Fig. 1.1 illustrates the typical bridge deck cross-section. Usually, two layers of asphalt are paved to cover the bridge deck, and their total thickness varies from site to site. Sometimes. a layer of rubber-based membrane is placed between the concrete and asphalt to protect the concrete from water damage caused by freeze-thaw cycles.

A large percentage of bridge decks across Ontario are now suffering from various forms of deterioration due to salt corrosion, freezing and thawing cycles, heavy traffic load and likes. The deterioration occurs mainly in the concrete or at the boundary between the concrete and asphalt. These faults include *debonding* where the asphalt layer separates from the concrete surface usually producing a small gap between them, *scaling* which is induced by the freeze-thaw process causing the disintegration of the concrete into a gravelly matrix, and *delamination* where cracks are formed between the concrete and the reinforcement as a result of the corrosion of the embedded reinforcing

bars. These faults are not detectable from a visual inspection.

The primary objectives of bridge deck inspection are therefore:

- to detect various types of deteriorations that may exist beneath the covering asphalt; and
- to estimate the thickness of the asphalt and the concrete cover over the rebars. These quantities are important in determining the amount of asphalt and concrete to be removed when repairing a damaged bridge deck.

These tasks can be carried out effectively by using impulse radar, which has the advantages of being a non-destructive inspection technique and that it is able to collect a large amount of data in a relatively short time. Impulse radar generates very narrow pulses with duration in the order of 1 ns and a repetition rate of 5 million pulses per second. The short temporal property not only permits a precise distance measurement but also provides a good separation of waves reflected from two closely-spaced boundaries in the bridge deck. Because of these attractive features, impulse radar is well suited for the bridge deck inspection, much superior to the conventional methods, such as drilling core samples and chain grag test. These conventional methods are costly, time-consuming and unreliable. Furthermore, the asphalt thickness and the concrete cover over reinforcing bars may vary on a bridge deck and no simple method has previously existed to measure these variations.

Figure 1.2 shows an actual pulse waveform transmitted by impulse radar, which is obtained by positioning the radar antenna directly over a thin metal plate that is much larger in extent than the antenna footprint. The radar-generated pulses are sent at normal incidence to the surface of the asphalt-covered bridge deck to be evaluated. These pulses are reflected and transmitted at the boundaries due to the impedance mismatch between different layers. The reflected signal received by the radar is depicted in Fig. 1.3. The highest peak at A represents the surface reflection from air-asphalt interface. The peak B is the reflection from the asphalt-membrane, and peak C and D are produced by the membrane-concrete and the concrete-steel bar interfaces, respectively. For digital storage and processing, the received signal is sampled in a fashion much like the sliding gate technique used in a sampling oscilloscope.

The reflected signal carries the information about the features of the bridge deck under investigation. What we need, then, is a proper signal processing procedure to extract the relevant information for evaluating the bridge deck, especially some 'high resolution' processing techniques which is capable of resolving the overlapping reflections from different interfaces, as illustrated in Fig. 1.3. This thesis attempts to offer a comprehensive treatment of these topics through developing and evaluat-

ing some optimal processing techniques for retrieving information from the reflected impulse radar signals. The information so obtained can be used to reveal the subsurface structures and determine the condition of the bridge decks. The studies in the thesis focus mainly on the statistical parameter estimation methods for the information extraction, though an in-depth discussion is also provided on the predictive deconvolution approach which is a class of nonparametric signal processing techniques.

1.2 Major Achievements of the Thesis

This thesis deals primarily with the modeling of reflected radar signals and the optimal estimation of characteristic parameters from reflected impulse radar signals for the evaluation of the the subsurface condition of a bridge deck. The following describes the major contributions made by this thesis along with a brief description of the techniques involved.

The multi-layer bridge deck can be described by a set of characteristic parameters, namely, the two-way travel time for the electromagnetic wave associated with the thickness of each layer and the reflection coefficient related to boundary between the adjacent layers. These parameters, once estimated from the reflected radar signals, can be used to determine the subsurface structures of a bridge deck. In the thesis, a mathematical representation of the radar-generated probing pulses is formulated in terms of a set of pulse shape parameters which can be estimated from measured radar pulses. Furthermore, a delayed sum model is established, successfully relating the reflected impulse radar waveforms with the characteristic parameters of the layered media. Based upon these signal models, the maximum likelihood method is applied, and a new eigenstructure-based estimation method is developed for determining the characteristic parameters from received radar signals.

The *method of maximum likelihood* (ML) is one of the most widely used techniques in parameter estimation problems. The principle of maximum likelihood estimation is that it takes the value of a parameter which maximizes a so-called likelihood function as the estimate of the parameter. The popularity of the ML method is largely due to the fact that it possesses some (mainly asymptotic) optimum properties. In the thesis, maximum likelihood estimators of the delay times and reflection coefficients are derived specifically for the reflected radar signals modeled by the delayed sum representation. To actually carry out the ML estimation, however, requires an explicit knowledge of the probability density function of the received signals, which may not be available in some cases. Another difficulty with the ML method is that it usually involves a nonlinear optimization procedure in which an iterative search for a globally optimal solution can be rather time-demanding.

The *eigenstructure-based* (EB) methods, on the other hand, are very efficient in computation and do not require the knowledge of probability density function. Moreover, their performance in terms of estimation accuracy is comparable to that of the ML in some circumstances [Stoica, 1989]. The eigenstructure-based methods, such as the well-known MUSIC algorithm [Schmidt, 1986], are a class of estimation techniques that make use of properties of the eigenstructure of data covariance matrix. They are extensively used in the direction-of-arrival (DOA) estimation, arising from array signal processing problems. The space spanned by the eigenvectors of the covariance matrix consists of 'signal subspace' and 'noise subspace', which are orthogonal to each other. The fact that the signal components of the received data are orthogonal to the noise subspace will lead to a solution to the estimation of signal parameters. A key step in these methods is the decomposition of data covariance matrix, that can be accomplished by very efficient algorithms which are readily available [Golub, 1983]. In spite of the high efficiency of the EB methods, they cannot be applied directly to the bridge deck problem, because the reflected radar signals do not satisfy some of the basic assumptions commonly made in their derivation. Failing to satisfy these assumptions results in rank deficiency of the data correlation matrix. Therefore, major modifications have to be made for the implementation of the EB methods in our problem. This thesis offers a simple, yet effective, solution and its implementation is almost as straightforward as the conventional EB methods. It should be noted that the new EB method imposes very few restrictions upon the signals therefore it can be applied to the more general problems of resolution and eastimation of overlapping echos.

A detailed evaluation of the estimators' error performance is also presented in the thesis, both by computer simulation and by an analysis of the Cramér-Rao Lower Bounds (CRLB) on the estimation errors. The analysis of CRLB not only predicts the best attainable performance of the estimators, but also provides us an insight into the dependence of the performance on the signal parameters and reveals the possible ways to improve our measurements. The computer simulation is also conducted, to assess the estimation errors under various circumstances.

Alternatively, the reflected signal may be described by a nonparametric, convolutional sum model. The information extraction can be achieved by *predictive deconvolution* procedures. The predictive deconvolution has been used successfully in the reflection seismology for geophysical exploration. In principle, it is direct application of Wiener optimal filtering theory to the inverse problem where the system output is known but the input is unknown and has to be determined from measured output. Due to the similarity between the reflection seismology and the radar testing of bridge decks, the predictive deconvolution methods are potentially applicable to the data processing of reflected radar

signals from the bridge decks. The implementation of the predictive deconvolution is simple and straightforward, which involves only solving a set of linear, normal equations and performing linear filtering of input signals. In the thesis, various forms of predictive deconvolution are derived, and computer simulation for both simulated and real signals is carried out to investigate the feasibility of the deconvolution techniques for the bridge deck problem.

1.3 Organization of the Thesis

Four chapters of this thesis, from Chapter 2 through Chapter 5, are devoted to the studies of parametric techniques for processing the reflected radar signals. Necessary assumptions are introduced in Chapter 2 to relate the problem of determining the bridge deck structure to the identification of a lossless, layered media system. Mathematical models are then established to approximate the radar-transmitted pulses and reflected signals in terms of a set of characteristic parameters. Based on these models, the ML method for estimation of the parameters is applied in Chapter 3. Examples are also given to test the ML method in estimating parameters from both simulated and real signal reflected from bridge decks. In Chapter 4, a new eigenstructure-based EB algorithm is derived, and applied to the estimation of the reflected signals. The error performances of the ML and the eigenstructure-based methods are evaluated in Chapter 5, and results are compared with the Cramér-Rao Lower Bounds (CRLB). Chapter 6 investigates the predictive deconvolution as a class of nonparametric techniques for processing the reflected signals, which is based upon a nonparametric, convolutional representation of the the reflected signals. Finally, Chapter 7 summarizes the major contributions and conclusions of the thesis. A detailed analysis of CRLB on the variances of parameter estimators is provided in the appendix.

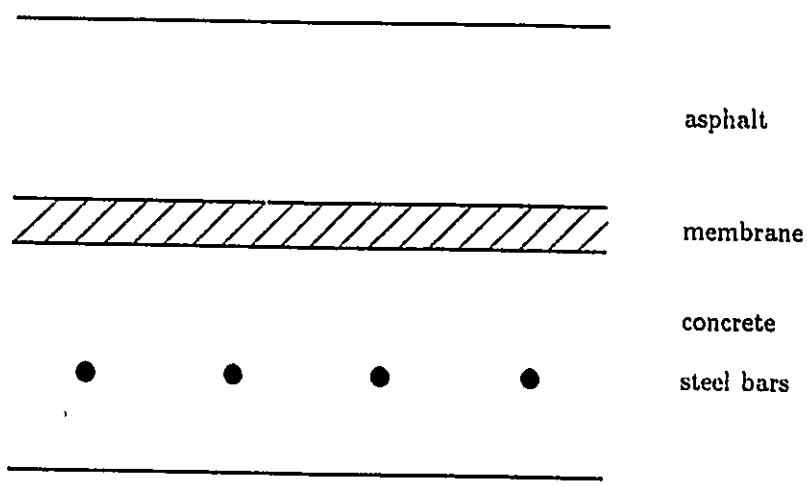

Figure 1.1: Sketch of a bridge deck cross-section.

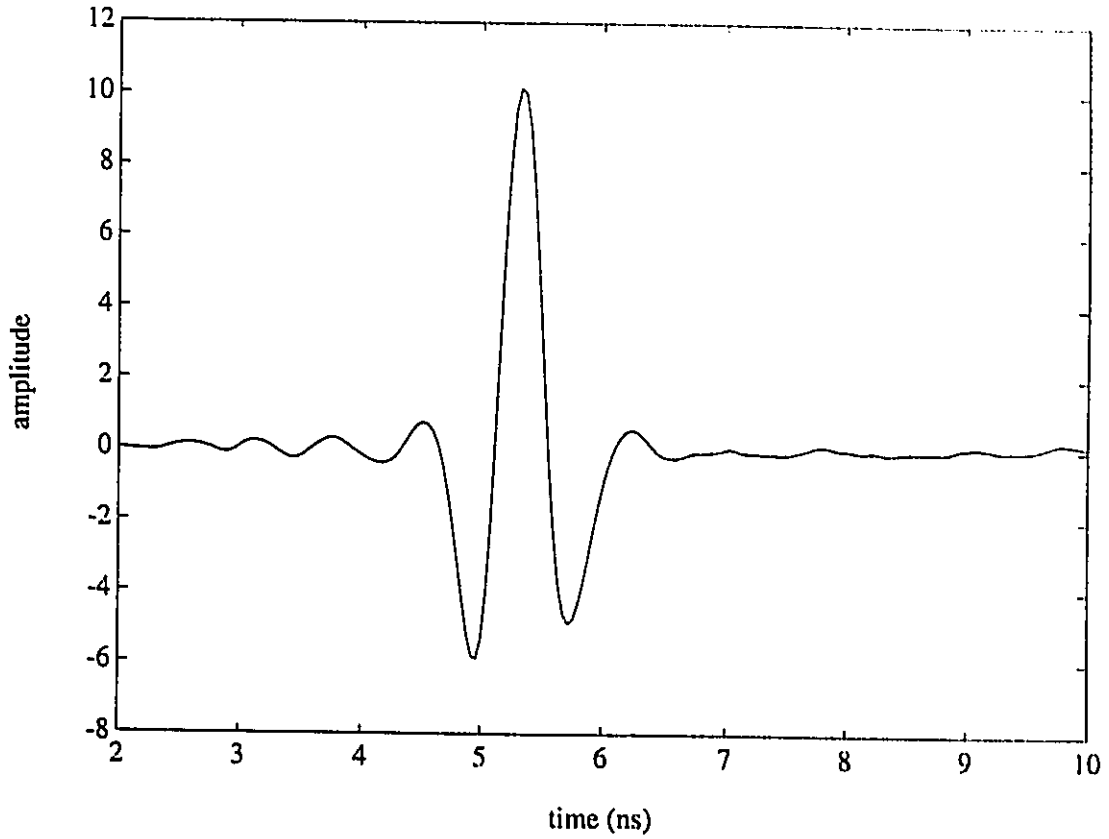

(Sampling period $T = 0.04$ ns.)

Figure 1.2: Measured waveform of radar-transmitted pulse for probing.

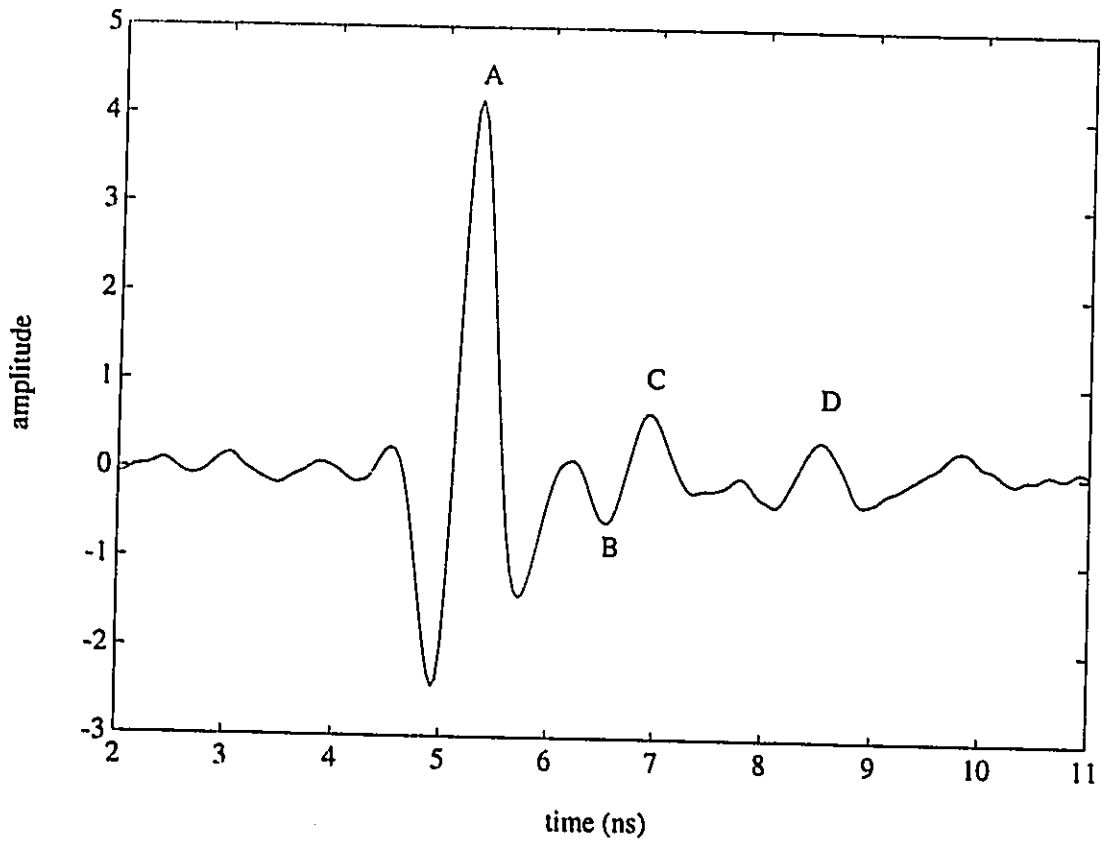

(Sampling period $T = 0.04$ ns.)

Figure 1.3: Measured waveform of reflected radar signal from bridge deck.

Chapter 2

Modeling of Reflected Radar Signals

2.1 Bridge Decks and Lossless Layered Media

As illustrated in Fig. 1.1, a bridge deck has a structure of multi-layered media consisting of asphalt, membrane, concrete and reinforcing steel bars (rebars). The objective of signal processing is to reveal the features of the bridge deck structures underneath the surface. If the bridge deck is viewed as a system, such a procedure may be regarded as a system identification or the *inverse* problem, where the radar-transmitted probing pulse (input) can be measured, and thus is known, and the system parameters are to be determined from reflected signals (output).

For simplicity, the inverse problem for multi-layered media is usually restricted to stratified, nonabsorptive (i.e., lossless) and horizontally layered media with each layer being homogeneous and isotropic [Mendel, 1980]. Figure 2.1 depicts such an idealized model for a layered media system consisting of K layers, where $s(t)$ and $y(t)$ denote, respectively, the incident radar pulse and reflected signal at surface, τ_k $(k = 1, 2, \ldots, K)$ the one-way travel time for electromagnetic wave in the kth layer, and r_k $(k = 1, 2, \ldots, K)$ the reflection coefficient associated with kth interface.

If we further assume that the probing radar signal is of normal incidence to the surface of

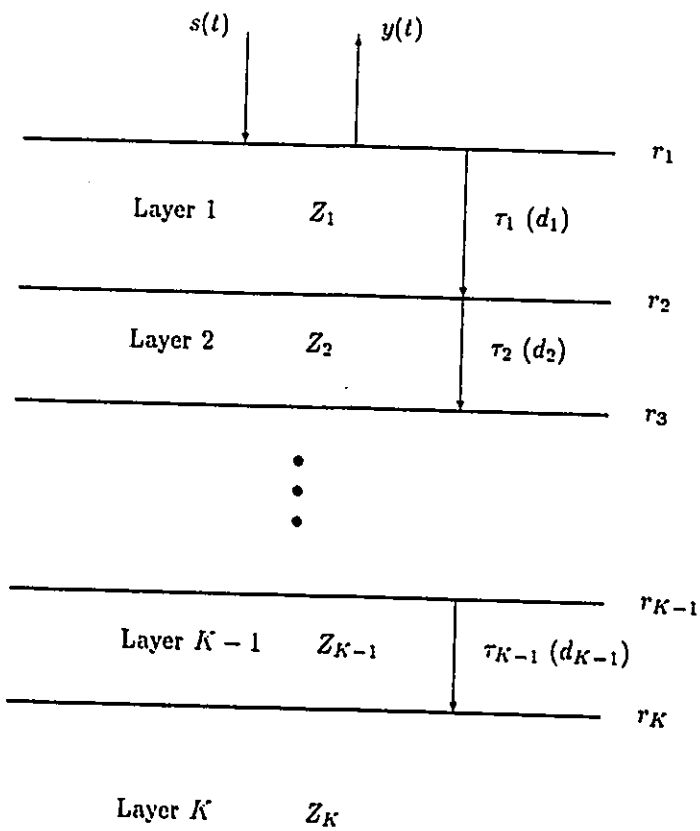

Figure 2.1: System of multi-layered media.

the layered media and it satisfies a one-dimensional wave equation (i.e., plane wave), then the propagation of electromagnetic wave in the layered media is completely determined by a set of characteristic parameters of the media, namely, the reflection coefficients and the one-way travel times. In other words, the layered media system under the above assumptions is completely described by these parameters in the context of electromagnetic properties [Mendel, 1980].

The travel time for the wave in the kth layer, τ_k, is related to d_k, the thickness of the layer, as well as the type of material. It can be written as [Kraus, 1991]

$$\tau_k = \frac{d_k}{v_k}, \tag{2.1}$$

where v_k is the group velocity of electromagnetic wave in the kth layer. For non-conducting medium the *conductivity* $\sigma = 0$, consequently, the velocity depends only on the *permittivity*, ϵ_k, and the *permeability*, μ_k, of the medium, such that

$$v_k = \frac{1}{\sqrt{\epsilon_k \mu_k}}. \tag{2.2}$$

The permittivity ϵ_k and permeability μ_k are complex in general, with their imaginary parts representing electromagnetic losses in the medium. They can be expressed as [Pozar, 1990]

$$\begin{aligned} \epsilon &= \epsilon_0 \epsilon_r - j\epsilon'', \\ \mu &= \mu_0 \mu_r - j\mu'', \end{aligned} \tag{2.3}$$

where

$\epsilon_0 = 8.854 \times 10^{-12}$ F/m is the permittivity of free-space;

$\mu_0 = 4\pi \times 10^{-7}$ H/m is the permeability of free-space;

$\epsilon_r \geq 1$ (dimensionless) is the dielectric constant;

μ_r (dimensionless) is the relative permeability, and for non-ferromagnetic materials $\mu_r \approx 1$;

$\epsilon'' \geq 0$ and $\mu'' \geq 0$ account for the losses.

For lossless and non-ferromagnetic media, $\sigma = \epsilon'' = \mu'' = 0$ and $\mu_r \approx 1$ [Cheng, 1983]. Thus, the permittivity for kth layer becomes $\epsilon_k = \epsilon_0 \epsilon_{r_k}$. From Eq.(2.2) we have

$$v_k = \frac{1}{\sqrt{\epsilon_0 \epsilon_{r_k} \mu_0 \mu_{r_k}}} \approx \frac{c}{\sqrt{\epsilon_{r_k}}},$$

where $c = 1/\sqrt{\epsilon_0 \mu_0} \approx 2.998 \times 10^8$ m/s is the velocity of light in free-space. Substituting this result into Eq.(2.1), we get

$$d_k = \frac{c\tau_k}{\sqrt{\epsilon_{r_k}}}, \qquad (k = 1, 2, \ldots, K). \tag{2.4}$$

Therefore, the thickness of each layer can be easily calculated if all the travel times τ_k's and dielectric constants ϵ_{r_k}'s are measured.

The electromagnetic wave impedance is an important parameter of a medium, and it is defined as the ratio of the electric field intensity to the magnetic field intensity in the medium [Pozar, 1990]. For plane waves, this impedance is also the *intrinsic* impedance of the medium. For a non-conducting medium, the intrinsic impedance, Z, is found to be

$$Z = \sqrt{\frac{\mu}{\epsilon}}.$$

Under the lossless assumption, Z is real and given by (for non-ferromagnetic medium)

$$Z = \sqrt{\frac{\mu_0\mu_r}{\epsilon_0\epsilon_r}} \approx \sqrt{\frac{\mu_0}{\epsilon_0\epsilon_r}} = \frac{\eta_0}{\sqrt{\epsilon_r}} \qquad (\Omega), \tag{2.5}$$

where $\eta_0 = \sqrt{\mu_0/\epsilon_0} \approx 377\Omega$ is the intrinsic impedance of free-space. Alternatively, Eq.(2.5) may be expressed as

$$\epsilon_r = \left(\frac{\eta_0}{Z}\right)^2. \tag{2.6}$$

Thus, the dielectric constant of the medium can be readily calculated, once the value of Z is known.

The reflection coefficient associated with the kth interface, r_k, is related to the intrinsic impedances of the materials of the kth and $(k-1)$th layers by the following equation [Cheng, 1983]:

$$r_k = \frac{Z_k - Z_{k-1}}{Z_k + Z_{k-1}}, \qquad (k = 1, 2, \ldots, K), \tag{2.7}$$

where Z_k and Z_{k-1} are the intrinsic impedances of kth and $(k-1)$th layer, respectively. The reflection coefficient r_k can be either positive or negative. Solving Eq.(2.7) for Z_k yields

$$Z_k = \frac{1 + r_k}{1 - r_k} Z_{k-1}, \qquad (k = 1, 2, \ldots, K). \tag{2.8}$$

It is noted that $Z_0 \approx \eta_0 \approx 377\Omega$ since the first layer is air in the bridge deck problem.

Therefore, the intrinsic impedances Z_k's may be calculated iteratively by Eq.(2.8), if the reflection coefficients, r_k's, can be estimated. The Z_k's so obtained can be then used to determine the dielectric constants ϵ_{r_k}'s by Eq.(2.6), and consequently, the thickness of all the layers, d_k's, can be obtained by Eq.(2.4), provided that the values of τ_k's are determined. It is clear now that if the bridge deck is modeled as the lossless layered media, then the whole identification problem is reduced to the estimation of a set of characteristic parameters, namely, the reflection coefficients $\{r_k\}$ and one-way travel times $\{\tau_k\}$, from the reflected radar signals.

2.2 Parametric Model for Radar-Generated Probing Pulses

2.2.1 Waveform of Probing Radar Pulse

For bridge deck inspection, the probing impulse radar must be able to resolve the reflections from the asphalt surface and the asphalt-membrane, the membrane-concrete and the concrete-rebar interfaces, since these reflections contain information relating to the bridge deck condition. Therefore, the probing radar pulse required for this purpose should be very short in duration, in order to achieve the required resolution.

The actual transmitted waveform of impulse radar, as depicted in Fig. 1.2, is very narrow in pulse-width (about 1 ns), which is necessary for high resolution probing of the bridge decks. A close examination of Fig. 1.2 reveals that the nearly symmetric probing signal has a waveform of damped oscillations which decay very rapidly with time. Mathematically, such a waveform may be approximated by a decaying cosine function $s(t)$ such that

$$s(t) = A\exp(-\beta|t|^m)\cos(2\pi f_c t), \tag{2.9}$$

where A, β, m, and f_c are the model parameters (constants) to be determined, and m is chosen to be an integer for analytic simplicity.

The measured radar pulse can be represented by

$$x(t) = s(t - t_d) + e(t),$$

where t_d is a time delay and $e(t)$ is an error term that may include measurement noise as well as modeling errors. For digital computer processing, the waveform is sampled, resulting in N data samples as

$$x(nT) = s(nT - t_d) + e(nT), \qquad n = 1, 2, \ldots, N. \tag{2.10}$$

The received radar waveforms in our problem are sampled at a period $T = 0.04$ ns, corresponding to a sampling frequency $f_s = 25$ GHz.

From the measured data samples $\{x(nT)\}$, the parameters in the model given by Eq.(2.9) can be determined by making use of optimization techniques. *Least Squares* is a commonly used criterion for such estimation problems. It states that the model parameters, A, β, m and f_c (and t_d, as well, if it is unknown), should be chosen such that they minimize the sum of squared errors, ε^2, defined as

$$\varepsilon^2(A, \beta, m, f_c, t_d) = \sum_{n=1}^{N}[x(nT) - s(nT - t_d)]^2. \tag{2.11}$$

Table 2.1: Estimated model parameters of radar pulse.

m	A	β	f_c	t_d	ε^2
1	12.014	2.271	1.104	5.336	31.78
2	10.357	3.574	1.100	5.335	6.47
3	9.873	6.787	1.088	5.335	9.96
4	10.807	1.063	1.756	5.337	436.8

This is a nonlinear least squares estimation problem. For the measured radar pulse as shown in Fig. 1.2, we set m to be 1, 2, 3 or 4 and then search for the values of A, β, f_c and t_d that minimize the quantity ε^2. The resulting estimates of the parameters are given in Table 2.1, and the corresponding waveforms approximated by the models (using these estimated parameters) are illustrated in Fig. 2.2.

As we can see from Table 2.1, the model produces the lowest error when m is set to 2. The same statement may be also made by observing Fig. 2.2. When $m = 2$, $s(t)$ is in fact a modulated Gaussian function, and the associated parameters are $A = 10.3570$ (V), $\beta = 3.5735\,(ns^{-2})$, and $f_c = 1.0998$ (GHz). The model corresponding to this set of parameters will be used to approximate the probing radar pulses for further studies in this thesis.

2.2.2 Spectrum of Probing Radar Pulse

The spectrum of $s(t)$, denoted as $S(j\omega)$, is obtained by taking the Fourier transform of Eq.(2.9) [Papoulis, 1977], namely,

$$S(j\omega) = \mathcal{F}[s(t)] = \int_{-\infty}^{\infty} s(t)e^{-j\omega t}dt. \tag{2.12}$$

Suppose that the Fourier transform of $f_1(t)$ and $f_2(t)$ are $F_1(j\omega)$ and $F_2(j\omega)$, respectively. Then, one property of the Fourier transform states that the Fourier transform of the product, $f_1(t)f_2(t)$,

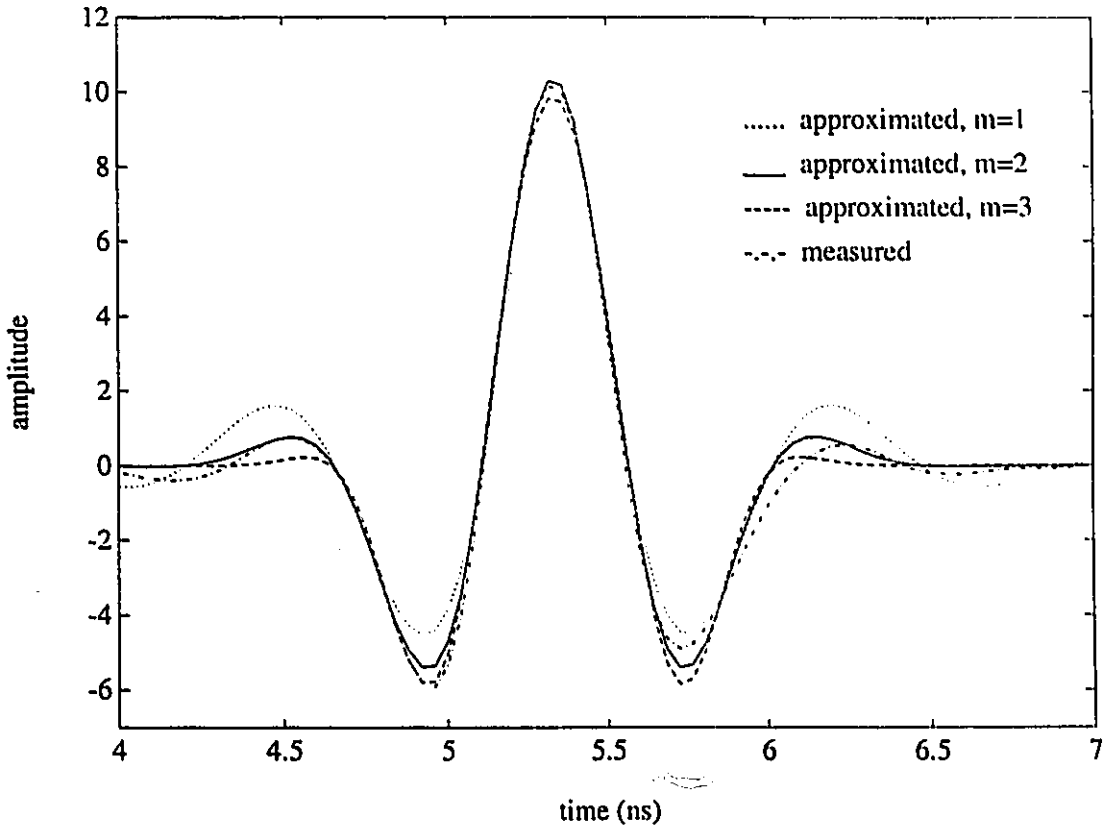

Figure 2.2: Approximation of probing radar pulse.

is equal to the convolution of $F_1(j\omega)$ and $F_2(j\omega)$, i.e.,

$$\mathcal{F}[f_1(t)f_2(t)] = \int_{-\infty}^{\infty} F_1(j\xi)F_1(j\omega - j\xi)\, d\xi. \tag{2.13}$$

If $m = 1$ is chosen in Eq.(2.9), the spectrum will be

$$S_1(j\omega) = \int_{-\infty}^{\infty} A\exp(-\beta|t|)\cos(\omega_c t)\, e^{-j\omega t}\, dt. \tag{2.14}$$

where $\omega_c = 2\pi f_c$. Let $f_1(t) = \cos(\omega_c t)$ and $f_2(t) = \exp(-\beta|t|)$. Then

$$F_1(j\omega) = \mathcal{F}[\cos(\omega_c t)] = \frac{1}{2}\delta(\omega - \omega_c) + \frac{1}{2}\delta(\omega + \omega_c), \tag{2.15}$$

and

$$F_2(j\omega) = \mathcal{F}[A\exp(-\beta|t|)] = \frac{2\beta A}{\omega^2 + \beta^2}.$$

From Eq.(2.13) we have

$$\begin{aligned} S_1(j\omega) &= \int_{-\infty}^{\infty} F_2(j\xi)F_1(j\omega - j\xi)\, d\xi \\ &= \beta A\left\{\frac{1}{(\omega-\omega_c)^2+\beta^2} + \frac{1}{(\omega+\omega_c)^2+\beta^2}\right\}, \end{aligned} \tag{2.16}$$

Similarly, for the case $m = 2$, the spectrum is

$$S_2(j\omega) = \int_{-\infty}^{\infty} A\exp(-\beta t^2)\cos(\omega_c t)\, e^{-j\omega t}\, dt. \tag{2.17}$$

Define $f_3(t) = A\exp(-\beta t^2)$. Its Fourier transform is

$$F_3(j\omega) = \mathcal{F}[f_3(t)] = \frac{A}{\sqrt{2\beta}}\exp\left(-\frac{\omega^2}{4\beta}\right).$$

From Eq.(2.15), the spectrum of $s(t)$ is found to be

$$\begin{aligned} S_2(j\omega) &= \int_{-\infty}^{\infty} F_3(j\xi)F_1(j\omega - j\xi)\, d\xi \\ &= \frac{A}{2\sqrt{2\beta}}\left\{\exp\left[-\frac{(\omega-\omega_c)^2}{4\beta}\right] + \exp\left[-\frac{(\omega+\omega_c)^2}{4\beta}\right]\right\}. \end{aligned} \tag{2.18}$$

It is noted that both $S_1(j\omega)$ and $S_2(j\omega)$ are real and positive for all $\omega \in (-\infty, \infty)$. The power spectrum of $s(t)$ is defined as $|20\log S(j\omega)|$. The power spectra of $s(t)$ for $m = 1, 2$ and 3 are plotted in Fig. 2.3 along with the power spectrum of the real radar-transmitted pulse. The latter is computed by performing Discrete Fourier Transform (DFT) on the sampled data of measured radar pulse (as shown in Fig. 1.2).

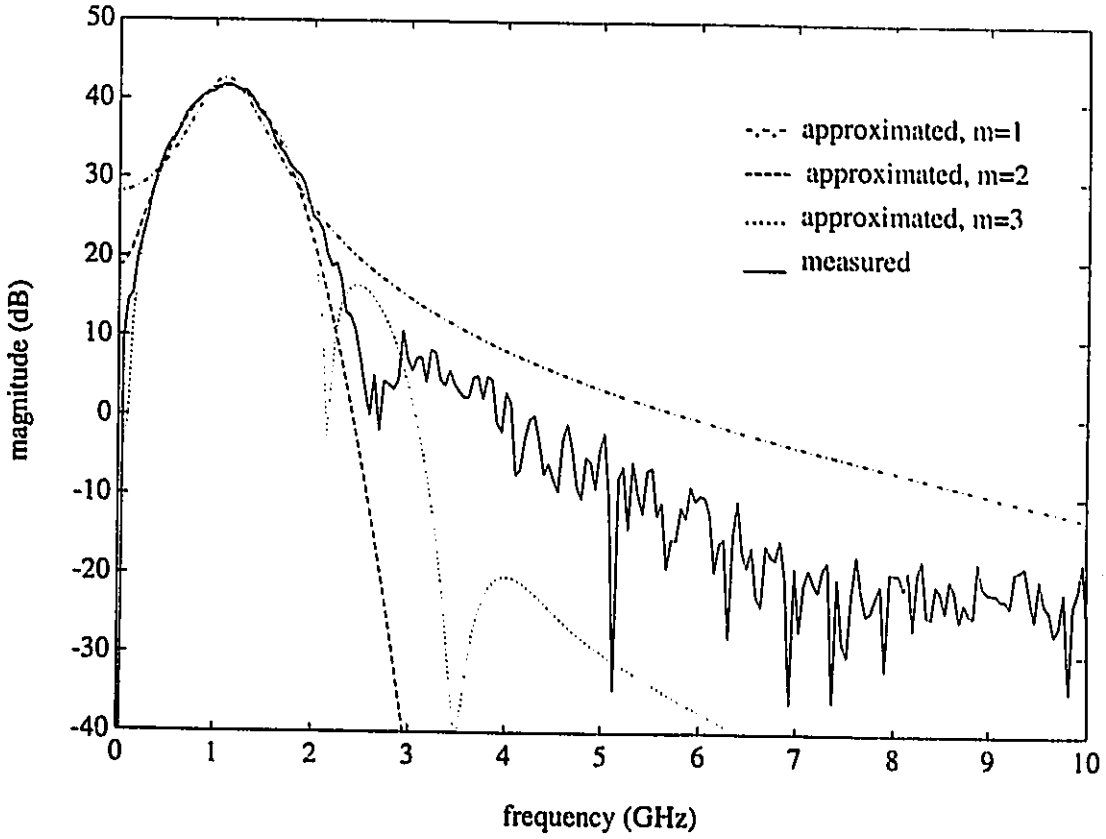

Figure 2.3: Spectra of probing radar pulses.

It is observed that the power spectra reach their peak values at a frequency of about $f_c = 1.1$ GHz. The model-approximated spectrum, for $m = 2$, agree with that of the real radar pulse reasonably well up to approximately 2.5 GHz (or down to about −30 dB from its peak value), however, beyond that the measured data becomes dominated by noise and other components that are not taken into account by the model, and the real spectrum deviates noticeably from that predicted by the model.

2.3 Delayed Sum Model for Reflected Signals

If the layered media are assumed to be non-dispersive, then, the individual frequency components of $s(t)$ maintain their original phase relationship as they propagate in the media. Hence, the shape of probing radar pulse, $s(t)$, will remain constant along its propagation path (or, no distortion) [Pozar,1990]. This implies that the reflected signal from a bridge deck modeled as a layered media will be a superposition of delayed replicas of the probing pulse, $s(t)$ [Mendel, 1983]. For lossless media with plane wave incidence (no spherical divergence), these reflected pulses are scaled simply according to the reflectivities associate with different interfaces in the media. Therefore, the reflected radar signal from a multi-layered bridge deck, $y(t)$, may be written as

$$y(t) = \sum_{k=1}^{K'} a_k s(t - t_k), \tag{2.19}$$

where $s(t)$ is given by Eq.(2.9) and a_k $(-1 \leq a_k \leq 1)$ is a scaling factor related to the kth interface of a multi-layered bridge deck as illustrated in Fig. 2.1. Note that the number of terms for the summation, K', is not necessarily equal to the number of layers of the media, K .

The reflected radar signals can be classified into prime and multiple reflections according to their propagation paths. As shown in Fig. 2.4, the prime reflections are those reflected directly from the interfaces, whereas the multiple reflections (or simply, multiples) are those reflected between different interfaces more than once before they reach the receiving antenna.

Obviously, the received signal $y(t)$, in general, consists of both the prime and multiple reflections. The latter can be ignored, however, when the interface reflection coefficients $\{r_k\}$ are sufficiently small [Robinson, 1980,1984]. As we will see later in the thesis, the reflection coefficients of the bridge deck interfaces are indeed quite small (well below 0.1, except for the air-asphalt interface). Such being the case, the value of a_k will be very close to that of the reflection coefficient r_k, and therefore, the scaling factor a_k's will be also referred to as reflection coefficients hereafter. Furthermore, the number of terms in the summation of Eq.(2.19) can be regarded equal to the number of layers, i.e.,

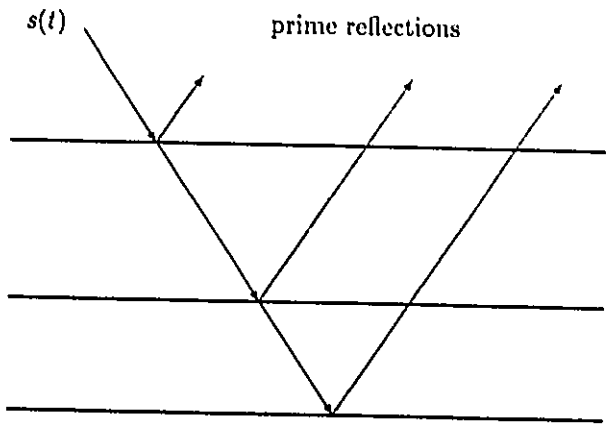

(a) Prime reflections

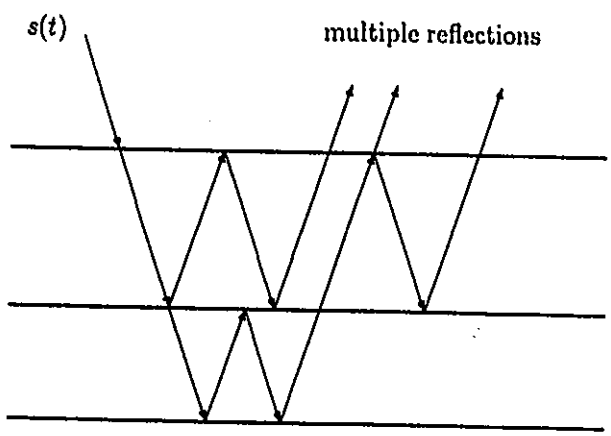

(b) Multiple reflections

Figure 2.4: Prime and multiple reflections.

$K' = K$, under such circumstances.

The delay time t_k appeared in Eq.(2.19) is related to one-way travel time τ_k in Fig. 2.1 by

$$t_k = 2\sum_{j=0}^{k-1} \tau_j. \qquad k = 1, 2, \ldots, K, \tag{2.20}$$

or, equivalently,

$$\tau_k = \frac{t_{k+1} - t_k}{2}. \qquad k = 0, 1, \ldots, K-1, \tag{2.21}$$

where $t_0 \equiv 0$, and $t_1 = 2\tau_0$ is the two-way travel time from the radar antenna to the surface of asphalt. Once the t_k's are known, τ_k's can be easily calculated. The relationship between the parameters associated with each layer or interface are illustrated in Fig. 2.5. Note that the quantity τ_K and hence d_K, the thickness of the Kth layer, is not measurable in Fig. 2.5, since we have neither knowledge on nor interest in the $(k+1)$th interface of the media.

Since the observed signal, reflected from a bridge deck, will also contain a certain amount of measurement noise and effects that are not described by the model as given by Eq.(2.19), the reflected signal $y(t)$ can be expressed more completely as

$$y(t) = \sum_{k=1}^{K} a_k s(t - t_k) + v(t), \tag{2.22}$$

where the noise $v(t)$ is usually assumed to be a stationary, white Gaussian random process. If $y(t)$ is sampled at every T second, we will have

$$y(nT) = \sum_{k=1}^{K} a_k s(nT - t_k) + v(nT), \tag{2.23}$$

where $n = 1, 2, \ldots, N$ and N is the total number of data samples.

It is noted that, in order for reflected radar signals to be described closely by the delayed sum model of 2.22, the boundaries between the layers of a bridge deck should be well defined such that the reflected signal at each interface is a replica of the probing radar pulse. In other words, the bridge deck is in either fairly good condition or not severely damaged. Fortunately, radar data, collected in 1991 from a total of 16 bridge decks in Ontario, have shown that many (7) bridge decks fall into this category. A summary of the data is presented in Table 2.2 (courtesy of Dr. T. Chung). Several bridge decks (3) have some damage and 6 decks have waveform features that cannot be presently analysed due to special construction materials. Of great importance is the ability of the impulse radar to distinguish among these categories.

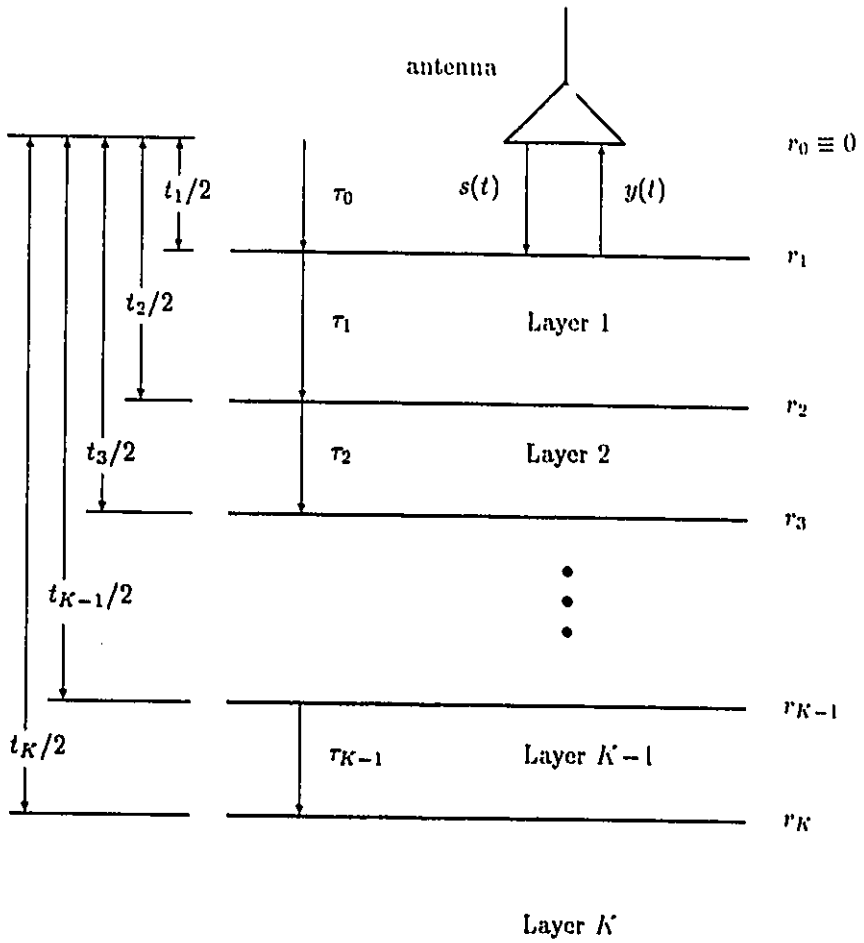

Figure 2.5: Parameters of multi-layered media.

Table 2.2: Radar testing of bridge decks in Ontario.

Condition	Bridge deck
GOOD	Constant Creek, site 29-98
	Avonmore Road, site 31-177
	Church Street, site 22-120
	Bonnechere River, site 29-192
	CRP O'head/Hwy 417, site 3-301
	South bound QEW/CPR, site 32-27
	Allen Exp Bridge #6, site 37-287
GOOD with some damage	Shook's Hill, site 24-194
DAMAGED	Jordan Harbor, site 18-19
	Glengarry, site 31-295
GOOD with undetermined	Krug St./Hwy 7&8, site 33-233
DAMAGED with undetermined	First Ave., site 33-223
	Allen Exp Bridge #5, site 37-286
UNDETERMINED	Bissett Creek, site 29-003
	King St. O'pass, site 33-222
	Weber Street, site 33-230

2.4 Simulation of Reflected Signals

2.4.1 Simulated Signal Without Noise

Since the shape of radar pulse $s(t)$ is known and approximated by Eq.(2.9), the reflected signal can be simulated by Eq.(2.19) for any given set of reflection coefficients $\{a_k\}$ and delay times $\{t_k\}$. Figure 2.6 shows an example of simulated reflection from a bridge deck by using the model given by Eq.(2.19) (ignoring the noise effect). The parameters used for approximating radar pulse $s(t)$ are: $m = 2$, $A = 10.357$, $\beta = 3.574\,(ns^{-2})$, and $f_c = 1.1$ (GHz). The values of travel times $\{\tau_k\}$ are: 5.32, 5.7, 6.56, 6.94 and 8.5 ns; and values of reflection coefficients $\{a_k\}$ are: 0.43, 0.075, -0.03, 0.05 and 0.042. These values are so chosen that the corresponding waveform gives an approximation of the real, reflected radar signal. (The issue of how to estimate the parameters from reflected signals will be the focus of the next two chapters.) The real reflected waveform from a bridge deck (as shown in Fig. 1.3) is also plotted in Fig. 2.6 for a comparison. It it noted that the simulated waveform fits tightly to the real reflected signal. This suggests that the delayed sum model as given by Eq.(2.19) is a good approximation of the reflected signals from the bridge decks.

Equation (2.22) indicates that the reflected waveform from a layered bridge deck $y(t)$ can be indeed described (other than a random noise component) by a set of characteristic parameters of the media, namely, the reflection coefficients $\{a_k\}$ and time delays $\{t_k\}$. In practice, however, these parameters are unknown and have to be estimated from the received signal $y(t)$. If a_k's and t_k's can be estimated, then we will be able to determine the subsurface characteristics of the bridge deck based on these parameters. The estimation of these parameters can be effectively accomplished by maximum likelihood or eigenstructure-based methods which will be introduced in the following chpaters.

2.4.2 Simulated Signals with Noise

We have shown in the last section that the reflected signal from a multi-layered bridge deck can be very closely approximated by a delay-sum model as described by Eq.(2.19). The discrepancies between the real and simulated signal, as exhibited in Fig. 2.6, can be attributed to the noise term $v(t)$ in Eq.(2.22) or Eq.(2.23).

As seen from Eq.(2.9) and Eq.(2.19), the magnitude of reflected signal $|y(t)|$ decreases to zero as time t goes to infinity. This implies that $y(t)$ is an energy type signal, i.e., of finite energy, but

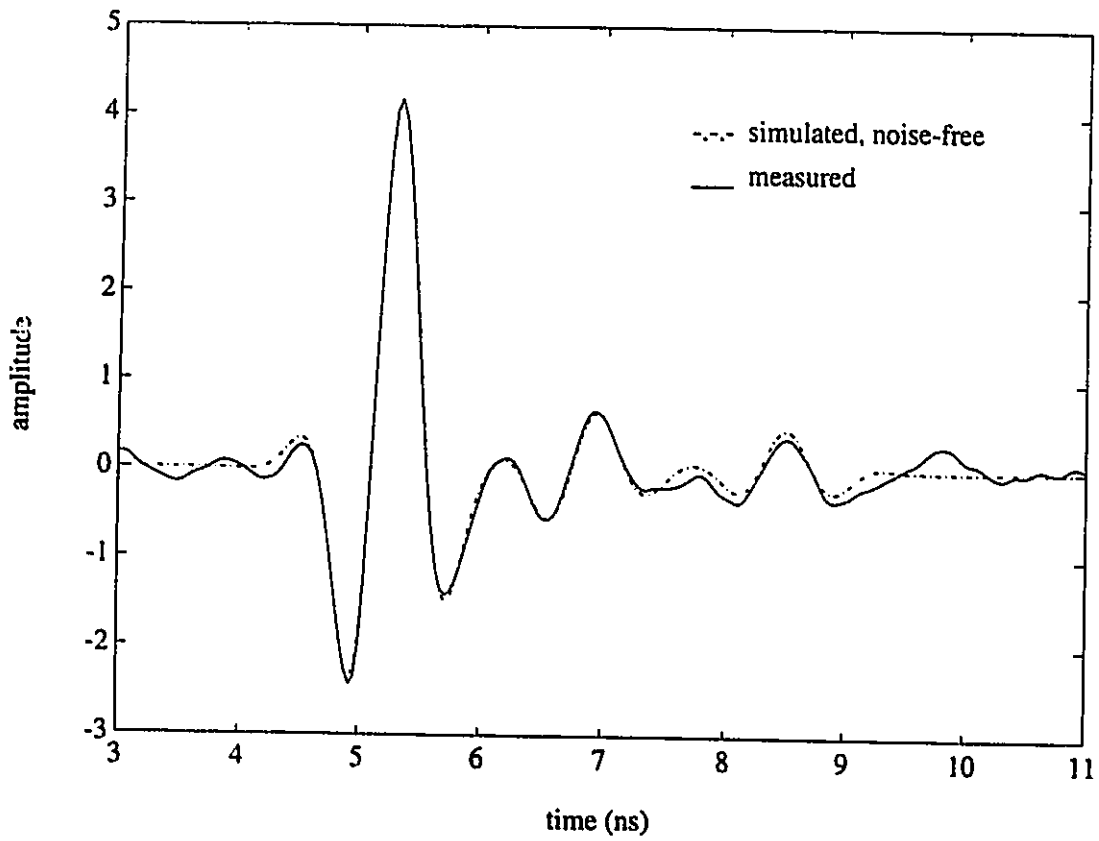

Figure 2.6: Approximation of reflected radar signal.

zero average power. On the other hand, the continuous, white random process is of infinite power in theory, but its power spectrum density (PSD) is of finite value. Therefore, it is appropriate to define the signal-to-noise ratio (SNR) as the ratio of signal energy to the noise power density. It should be noted, however, that for a fixed level of noise power, the signal-to-noise ratio varies from time to time because the amplitudes of reflections differ from layer to layer, depending on the reflection coefficients of the interfaces. In other words, we will have a signal-to-noise ratio, ρ for each reflected radar pulse. Suppose that the PSD of the white noise is $N_0/2$. For kth reflected pulse (arrival), ρ_k can be defined as the ratio of kth pulse energy (Es_k) to the noise power density $N_0/2$ [Haykin, 1983], namely,

$$\begin{aligned}
\rho_k &\stackrel{\text{def}}{=} 2Es_k/N_0 \\
&= \frac{2}{N_0}\int_{-\infty}^{\infty} a_k^2 s^2(t)\,dt \\
&= \frac{2a_k^2}{N_0}\int_{-\infty}^{\infty} e^{-2\beta t^2}\cos^2\omega_c t\,dt \\
&= \frac{a_k^2 A^2}{N_0}\sqrt{\frac{\pi}{2\beta}}\left\{1+\exp(-\omega_c^2/2\beta)\right\},
\end{aligned} \tag{2.24}$$

where A, β, $\omega_c = 2\pi f_c$ are all model parameters of the probing radar pulse $s(t)$ as listed in Table 2.1 for $m = 2$. Note that the integral $\int_{-\infty}^{\infty} s^2(t)\,dt$ in Eq.(2.24) gives the total energy of the probing signal E_s, i.e.,

$$E_s = \int_{-\infty}^{\infty} s^2(t)\,dt = \frac{A^2}{2}\sqrt{\frac{\pi}{2\beta}}\left\{1+\exp(-\omega_c^2/2\beta)\right\}. \tag{2.25}$$

As a convention, the signal-to-noise ratio, SNR_k, is usually expressed in dB, which is related to ρ_k by

$$\mathrm{SNR}_k = 10\log_{10}(\rho_k) \tag{2.26}$$

In this thesis, the level of SNR is usually specified with respect to the weakest arrival in the reflected signal if it is not explicitly indicated.

An example of simulated reflection from a bridge deck is illustrated in Fig. 2.7, which corresponds to a 0 dB signal-to-noise ratio with respected to the 3rd arrival (the weakest reflected pulse). The values of reflection coefficients and time delays are also given in Fig. 2.7. The power spectra of the real and two simulated signals are shown in Fig. 2.8. It is noted that the spectra of simulated signals are in a good agreement with the real one up to about 2.5 GHz.

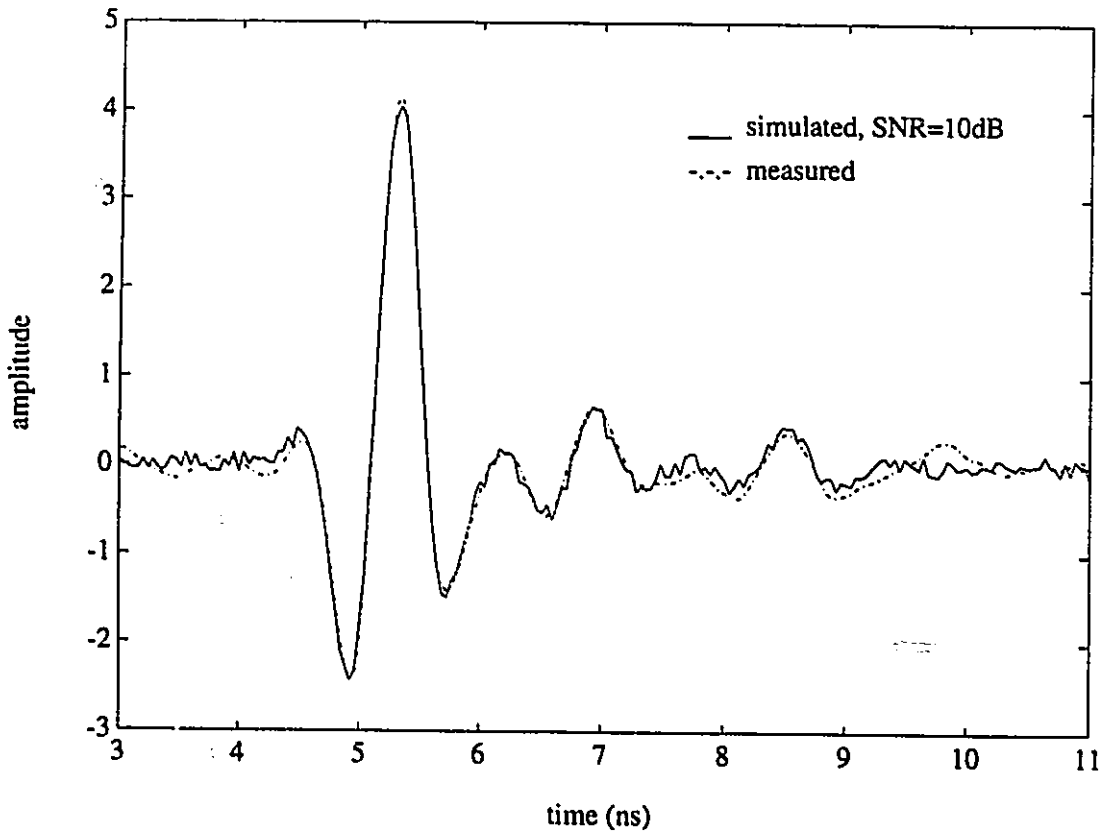

Figure 2.7: Simulated signal with noise.

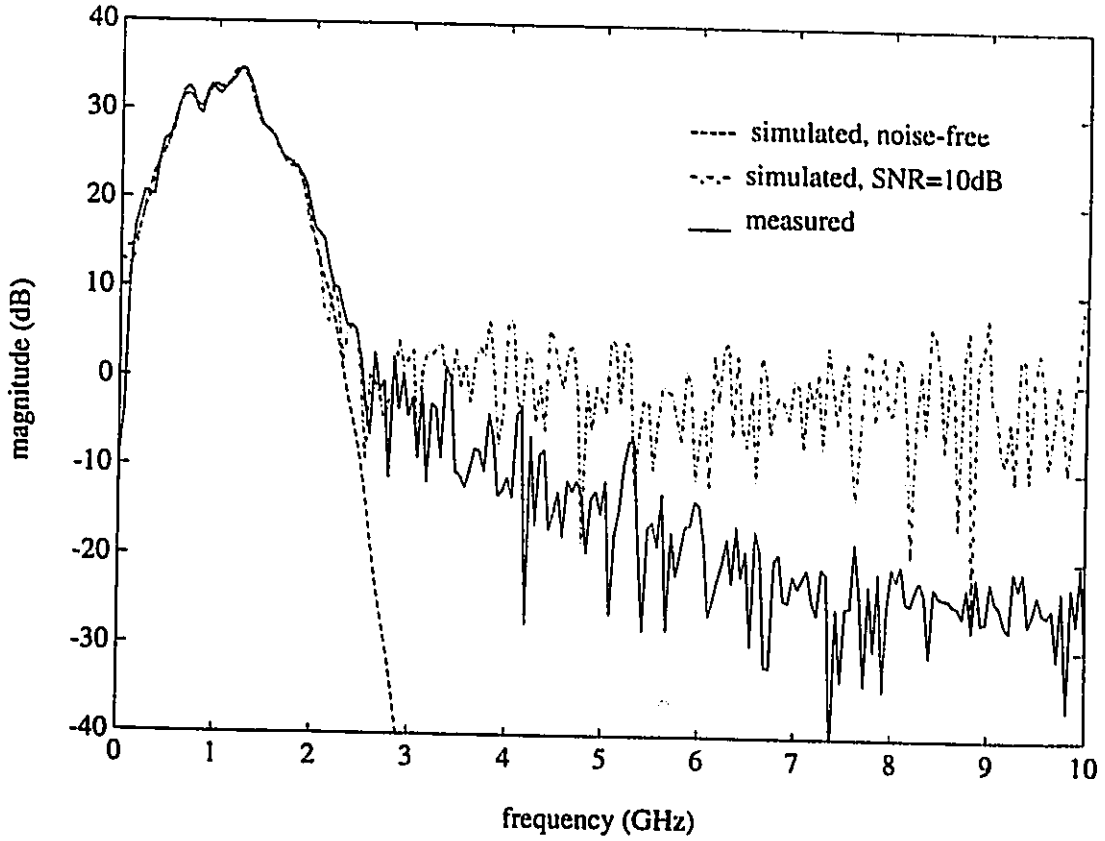

Figure 2.8: Spectra of reflected signals.

2.5 Summary

This chapter addresses the problem of modeling reflected radar signals. The bridge deck under our consideration may be regarded as media of multiple layers, consisting of asphalt, membrane, concrete and rebars. For simplicity, the media are assumed to be stratified, lossless, and horizontally layered with each layer being homogeneous and isotropic. Such a multi-layered media system is completely described by a set of characteristic parameters of the media, namely, the reflection coefficients associated with the interfaces and the one-way travel times for electromagnetic wave in the layers. It is further demonstrated that the waveform of radar-generated pulses can be closely approximated by a modualted Gaussian function, $s(t)$. Consequently, for the normal incidence and non-dispersive media, the received signal at surface is a superposition of scaled and delayed replicas of the probing pulse, $s(t)$. This leads to the delayed sum model for the reflected signal. In addition, the scaling factors in the model will be very close to the reflection coefficients and the number of reflected pulses equal to the number of layers when the reflection coefficients are sufficient small, or equivalently, when the multiple reflections can be ignored. The effectiveness of the suggested signal model is also supported by the simulation examples.

Chapter 3

Maximum Likelihood Estimation of Reflected Signal Parameters

The method of maximum likelihood (ML) has been extensively used in a large variety of statistical estimation problems since the original work of Fisher [Kendall, 1976]. In this chapter, we will first give a review of the maximum likelihood method for parameter estimation and some of its important properties. Then, ML parameter estimators will be derived for the reflected radar signals, and examples of maximum likelihood estimation will be presented for both simulated and real signals.

3.1 Maximum Likelihood Estimation: Principle and Properties

Suppose that $\{x_i; i = 1, 2, \ldots, n\}$ are the observed samples of random variables $\{X_i; i = 1, 2, \ldots, n\}$. The likelihood function is defined as a non-negative, real valued function on the parameter space Θ, which is proportional to the probability density function of $(X_1, X_2, \ldots, X_n)$ at $(x_1, x_2, \ldots, x_n)$.

Therefore if $f(x_1, \ldots, x_n|\theta)$ is the joint probability density function (p.d.f.) of $(X_1, X_2, \ldots, X_n)$ for the parameter $\theta \in \Theta$, the likelihood function of θ, given $(x_1, x_2, \ldots, x_n)$, is

$$\ell(\theta \mid x_1, \ldots, x_n) = \alpha f(x_1, \ldots, x_n \mid \theta), \tag{3.1}$$

where the proportionality factor $\alpha\,(0 < \alpha < \infty)$ could depend on $(x_1, x_2, \ldots, x_n)$ but is independent of θ [Kendall, 1976]. Note that the likelihood function is treated as a function of θ for a given set of observed samples $(x_1, x_2, \ldots, x_n)$. In practice, the value of the parameter θ is unknown, and therefore it has to be estimated from the given observables $\{x_i\}$. This is one of the most commonly encountered issues in statistical inference. An *estimator* of the parameter θ is, in general, a function of the random variables $(X_1, X_2, \ldots, X_n)$, that is, $\hat{\theta} = \hat{\theta}(X_1, X_2, \ldots, X_n)$. The value that $\hat{\theta}$ takes at the observed values of the random variables, $\hat{\theta}(x_1, x_2, \ldots, x_n)$, is called an *estimate* of θ.

The principle of maximum likelihood states that the estimate, $\hat{\theta}_{ml}$, of the parameter θ should be chosen within its admissible range such that $\hat{\theta}_{ml}$ maximizes the likelihood function, i.e.,

$$\ell(\hat{\theta}_{ml} \mid x_1, \ldots, x_n) \geq \ell(\theta \mid x_1, \ldots, x_n), \quad \text{for all possible } \theta \in \Theta. \tag{3.2}$$

Suppose that $\ell(\theta \mid x_1, \ldots, x_n)$ is differentiable with respect to θ. Then, a necessary condition for $\ell(\theta \mid x_1, \ldots, x_n)$ to achieve the maximum is that $\hat{\theta}_{ml}$ satisfies the equation

$$\frac{\partial}{\partial\theta}\ell(\theta) \mid_{\theta=\hat{\theta}_{ml}} = 0. \tag{3.3}$$

where $\ell(\theta)$ is a short notation for $\ell(\theta \mid x_1, \ldots, x_n)$.

The likelihood function given by Eq.(3.1) for many problems can be a rather complicated function of the parameter θ, and it may contain a number of local maxima. In such cases, we must employ a global search procedure to obtain the maximum likelihood estimate. There exist several algorithms that can deal with this global maximization problem, such as the grid search method [IMSL, 1990], Simulated Annealing [Kirkpatrick, 1983; Laarhoven, 1987], and Genetic Algorithm [Goldberg, 1986]. These techniques provide globally optimal solution with various degrees of accuracy, yet they all demand great amount of computation time.

The superiority of the maximum likelihood estimation is largely due to the fact that the resulting estimators possess excellent asymptotic performance, i.e., the limiting performance as the number of data samples n approaches to infinity. Before giving these properties, we introduce the concepts of *unbiasedness*, *consistency* and *efficiency* that are commonly used to describe the estimator performance. Let $\mathbf{X} = (X_1, X_2, \ldots, X_n)$ and $\mathbf{x} = (x_1, x_2, \ldots, x_n)$.

Definition 1. If the expected value of $\hat{\theta}$ is equal to θ, i.e., $E(\hat{\theta}) = \theta$, then $\hat{\theta}$ is called an *unbiased* estimator of θ.

Definition 2. The estimator $\hat{\theta}$ is *consistent* if the mean squared error (MSE) of $\hat{\theta}$, $MSE(\hat{\theta}) = E[(\hat{\theta} - \theta)^2]$, approaches to zero as the sample size n becomes infinitely large, *i.e.*,

$$\lim_{n \to \infty} MSE(\hat{\theta}) = 0.$$

Definition 3. An unbiased estimator $\hat{\theta}$ is said to be *efficient* if its variance, $Var(\hat{\theta}) = E[(\hat{\theta} - E(\theta))^2]$, attains the Cramér-Rao Lower Bound, or

$$Var(\hat{\theta}) = \left\{ E\left[\left(\frac{\partial \log \ell(\theta)}{\partial \theta} \right)^2 \right] \right\}^{-1}.$$

What follows is a brief summary of some important properties of the maximum likelihood estimator $\hat{\theta}_{ml}$ under fairly general conditions (for more details, see the references [Kendall, 1976; Lehmann, 1983; Zacks, 1971].

Property 1. The maximum likelihood estimator $\hat{\theta}_{ml}$ is consistent, Therefore, $\hat{\theta}_{ml}$ is asymptotically unbiased.

Property 2. If an efficient estimator of θ exists, then it is the same as $\hat{\theta}_{ml}$.

Property 3. $\hat{\theta}_{ml}$ is asymptotically efficient.

Property 4. $\hat{\theta}_{ml}$ is asymptotically normally distributed.

Property 5. (*Invariance principle*) If $\hat{\theta}_{ml}$ is the maximum likelihood estimator of θ, then $g(\hat{\theta}_{ml})$ is the maximum likelihood estimator of $g(\theta)$ for any function of θ, $g(\theta)$.

These attractive properties make the maximum likelihood method an extremely popular technique for statistical parameter estimation.

3.2 ML Estimators of Signal Parameters

In the Section 2.3, we have demonstrated that the reflected signal $y(t)$ from bridge deck can be represented by a superposition of delayed radar pulses. After being sampled, it can be expressed as

$$y(nT) = \sum_{k=1}^{K} a_k s(nT - t_k) + v(nT), \tag{3.4}$$

where the probing radar pulse $s(t)$ is given by

$$s(t) = A\exp(-\beta t^2)\cos(2\pi f_c t). \tag{3.5}$$

The values of parameters A, β, and f_c are all given in Table 2.1 in the last chapter.

Equation (3.4) may be also expressed more compactly in a matrix form as follows:

$$\mathbf{y} = \mathbf{S}(\mathbf{t})\mathbf{a} + \mathbf{v}, \tag{3.6}$$

where $\mathbf{a}$, $\mathbf{t}$ are K-by-1 vectors and $\mathbf{y}$, $\mathbf{v}$ N-by-1 vectors, defined as

$$\begin{aligned} \mathbf{a} &= (a_1, \ldots, a_K)^T, \\ \mathbf{t} &= (t_1, \ldots, t_K)^T, \\ \mathbf{y} &= [y(T), \ldots, y(nT)]^T, \\ \mathbf{v} &= [v(T), \ldots, v(nT)]^T, \end{aligned} \tag{3.7}$$

and $\mathbf{S}(\mathbf{t})$ a N-by-K matrix,

$$\mathbf{S} = \mathbf{S}(\mathbf{t}) = \begin{pmatrix} s(T-t_1) & s(T-t_2) & \cdots & s(T-t_K) \\ s(2T-t_1) & s(2T-t_2) & \cdots & \\ \vdots & \vdots & & \vdots \\ s(NT-t_1) & & \cdots & s(NT-t_K) \end{pmatrix}. \tag{3.8}$$

Here, the superscript $(\cdot)^T$ denotes vector or matrix transpose.

If the noise $v(nT)$ is assumed to be a white Gaussian process with zero-mean and unknown variance σ^2, then its probability density function is given by

$$f_v(x) = \frac{1}{\sqrt{2\pi\sigma^2}}\exp(-\frac{x^2}{2\sigma^2}). \tag{3.9}$$

From the relationship given by Eq.(3.4) and the fact that the noise sequence $\{v(nT)\}$ is uncorrelated, or independent for a Gaussian process, we may readily obtain the joint probability density function of the observables $\{y(nT),\ n = 1, \ldots, N\}$ as

$$\begin{aligned} f_{\mathbf{y}}(y(T), \ldots, y(nT)) &= \prod_{n=1}^{N} f_v(y(nT) - \sum_k a_k s(nT - t_k)) \\ &= \frac{1}{(2\pi\sigma^2)^{N/2}}\exp\left\{-\frac{1}{2\sigma^2}\sum_{n=1}^{N}\left[y(nT) - \sum_{k=1}^{K} a_k s(nT - t_k)\right]\right\}. \end{aligned}$$

Following the the notation introduced in Eq.(3.6), the above joint p.d.f. may be presented in a matrix form, i.e.,

$$f_{\mathbf{y}}(\mathbf{y}) = \frac{1}{(2\pi\sigma^2)^{N/2}} \exp\left\{-\frac{1}{2\sigma^2}[\mathbf{y} - \mathbf{S}(\mathbf{t})\mathbf{a}]^T[\mathbf{y} - \mathbf{S}(\mathbf{t})\mathbf{a}]\right\}. \tag{3.10}$$

Consequently, the likelihood function of the unknown parameters $\{a_k\}$, $\{t_k\}$ and σ^2, defined by Eq.(3.1), for the given data samples $\{y(nT),\ n = 1, \ldots, N\}$ can be written as

$$\ell(\mathbf{a}, \mathbf{t}, \sigma^2) = \frac{1}{(2\pi\sigma^2)^{N/2}} \exp\left\{-\frac{1}{2\sigma^2}[\mathbf{y} - \mathbf{S}(\mathbf{t})\mathbf{a}]^T[\mathbf{y} - \mathbf{S}(\mathbf{t})\mathbf{a}]\right\}. \tag{3.11}$$

Taking the logarithm of Eq.(3.11) and ignoring constant terms results in the log-likelihood function of $\{\mathbf{a}, \mathbf{t}\}$

$$\begin{aligned} L(\mathbf{a}, \mathbf{t}, \sigma^2) &= \ln \ell(\mathbf{a}, \mathbf{t}, \sigma^2) \\ &= -\frac{N}{2}\ln\sigma^2 - \frac{1}{2\sigma^2}[\mathbf{y} - \mathbf{S}(\mathbf{t})\mathbf{a}]^T[\mathbf{y} - \mathbf{S}(\mathbf{t})\mathbf{a}]. \end{aligned} \tag{3.12}$$

To compute the maximum likelihood estimates of the parameters, we have to maximize the log-likelihood function $L(\mathbf{a}, \mathbf{t}, \sigma^2)$ with respect to all the unknown parameters, i.e., a_k's, t_k's and σ^2 [Van Trees, 1968]. Let us first fix $\mathbf{a}$ and $\mathbf{t}$, and maximize L with respect to σ^2 by setting

$$\frac{\partial L(\mathbf{a}, \mathbf{t}, \sigma^2)}{\partial \sigma^2} = 0,$$

which yields

$$-\frac{N}{2\sigma^2} + \frac{1}{2(\sigma^2)^2}[\mathbf{y} - \mathbf{S}(\mathbf{t})\mathbf{a}]^T[\mathbf{y} - \mathbf{S}(\mathbf{t})\mathbf{a}] = 0.$$

Solving this equation for σ^2 gives the estimate $\hat{\sigma}^2$ in terms of $\mathbf{a}$ and $\mathbf{t}$, namely,

$$\hat{\sigma}^2 = \frac{1}{N}[\mathbf{y} - \mathbf{S}(\mathbf{t})\mathbf{a}]^T[\mathbf{y} - \mathbf{S}(\mathbf{t})\mathbf{a}]. \tag{3.13}$$

Substituting this result back into Eq.(3.12), and again ignoring constant terms, then we have

$$L(\mathbf{a}, \mathbf{t}) = -\frac{N}{2}\ln([\mathbf{y} - \mathbf{S}(\mathbf{t})\mathbf{a}]^T[\mathbf{y} - \mathbf{S}(\mathbf{t})\mathbf{a}]). \tag{3.14}$$

Therefore, the ML estimates of $\{a_k\}$ and $\{t_k\}$ may be obtained by maximizing Eq.(3.14) with respect to these parameters.

Since the logarithm is a monotonic function, the above maximization problem is equivalent to the following minimization problem:

$$\begin{aligned} \min_{\mathbf{a},\mathbf{t}} \mathcal{E}(\mathbf{a}, \mathbf{t}) &\stackrel{\text{def}}{=} \min_{\mathbf{a},\mathbf{t}} \| \mathbf{y} - \mathbf{S}(\mathbf{t})\mathbf{a} \|^2 \\ &= \min_{\mathbf{a},\mathbf{t}} \{[\mathbf{y} - \mathbf{S}(\mathbf{t})\mathbf{a}]^T[\mathbf{y} - \mathbf{S}(\mathbf{t})\mathbf{a}]\}. \end{aligned} \tag{3.15}$$

To carry out this minimization, we first fix t and minimize the error function $\mathcal{E}$ with respect to a by setting

$$\frac{\partial}{\partial a_k}\mathcal{E}(\mathbf{a},\mathbf{t}) = 0,$$

for all $k = 1, 2, \ldots, K$. The estimate $\hat{\mathbf{a}}$ is then obtained by solving these K simultaneous equations for $a_1, a_2, \ldots, a_K$. To simplify the notation , we define the differentiation of a scalar-valued function $g(\mathbf{x})$ with respect to the column vector $\mathbf{x} = (x_1, x_2, \ldots, x_n)^T$ as

$$\frac{dg(\mathbf{x})}{d\mathbf{x}} \stackrel{\text{def}}{=} \begin{pmatrix} \frac{\partial g(\mathbf{x})}{\partial x_1} \\ \frac{\partial g(\mathbf{x})}{\partial x_2} \\ \vdots \\ \frac{\partial g(\mathbf{x})}{\partial x_n} \end{pmatrix}. \tag{3.16}$$

Then, for any n-by-1 vector $\mathbf{b}$, we have

$$\frac{d}{d\mathbf{x}}(\mathbf{b}^T\mathbf{x}) = \frac{d}{d\mathbf{x}}(\mathbf{x}^T\mathbf{b}) = \mathbf{b}, \tag{3.17}$$

and, for any n-by-n matrix $\mathbf{A}$,

$$\frac{d}{d\mathbf{x}}(\mathbf{x}^T\mathbf{A}\mathbf{x}) = 2\mathbf{A}\mathbf{x}. \tag{3.18}$$

Now, expand $\mathcal{E}(\mathbf{a},\mathbf{t})$,

$$\begin{aligned} \mathcal{E}(\mathbf{a},\mathbf{t}) &= \mathbf{y}^T\mathbf{y} - \mathbf{a}^T\mathbf{S}^T\mathbf{y} - \mathbf{y}^T\mathbf{S}\mathbf{a} + \mathbf{a}^T\mathbf{S}^T\mathbf{S}\mathbf{a} \\ &= \mathbf{y}^T\mathbf{y} - 2\mathbf{a}^T\mathbf{S}\mathbf{y} + \mathbf{a}^T\mathbf{S}^T\mathbf{S}\mathbf{a}. \end{aligned} \tag{3.19}$$

Note that every term in Eq.(3.19) is scalar-valued. We differentiate $\mathcal{E}(\mathbf{a},\mathbf{t})$ with respect to a by using the formulas in Eq.(3.17) and Eq.(3.18), and then set the results to 0 (null vector). This gives

$$-2\mathbf{S}\mathbf{y} + 2\mathbf{S}^T\mathbf{S}\mathbf{a} = 0.$$

The solution for a yields the estimate $\hat{\mathbf{a}}$ in term of t and y, i.e.,

$$\hat{\mathbf{a}} = [\mathbf{S}^T(\mathbf{t})\mathbf{S}(\mathbf{t})]^{-1}\mathbf{S}^T(\mathbf{t})\mathbf{y}. \tag{3.20}$$

Substitution of Eq.(3.20) into Eq.(3.15) gives the error function $\mathcal{E}$ in term of t only, and the MLE of t can be thus attained by solving following minimization problem:

$$\hat{\mathbf{t}} = \arg\min_{\mathbf{t}} \mathcal{E}(\mathbf{a},\mathbf{t})\,|_{\mathbf{a}=\hat{\mathbf{a}}}$$

$$= \arg\min_{\mathbf{t}} \| \mathbf{y} - \mathbf{S}(\mathbf{t})[\mathbf{S}^T(\mathbf{t})\mathbf{S}(\mathbf{t})]^{-1}\mathbf{S}^T(\mathbf{t})\mathbf{y} \|$$

$$= \arg\min_{\mathbf{t}} \mathbf{y}^T \left\{ \mathbf{I}_N - \mathbf{S}(\mathbf{t})[\mathbf{S}^T(\mathbf{t})\mathbf{S}(\mathbf{t})]^{-1}\mathbf{S}^T(\mathbf{t}) \right\} \mathbf{y}, \tag{3.21}$$

where $\mathbf{I}_N$ is a N-by-N identity matrix. In general, the estimate $\hat{\mathbf{t}}$ can be calculated iteratively from Eq.(3.21) for given data vector $\mathbf{y}$.

Based on above discussion, the procedure of maximum likelihood estimation of $\{a_k\}$ and $\{t_k\}$ may be carried out in two steps:

1. first solve Eq.(3.21) to obtain the time delay estimate $\hat{\mathbf{t}}$, and then
2. substitute $\hat{\mathbf{t}}$ into Eq.(3.20) to obtain the estimate of reflection coefficients $\hat{\mathbf{a}}$.

Examples will be given in the following sections to demonstrate the feasibility of MLE of the characteristic parameters of bridge decks.

3.3 ML Estimation for Simulated Signals

Once the reflected signal $\{y(nT)\}$ has been simulated in the way as described in Section 2.4, the parameters, $\{a_k\}$ and $\{t_k\}$ may be estimated from the simulated signal by the maximum likelihood method developed in the previous sections.

A comparison between the estimated and true values of these parameters will indicate the feasibility of the MLE in our problem. To compute the ML estimates of $\{a_k\}$ and $\{t_k\}$ for the given data samples $\{y(nT)\}$, we follow the procedure outlined in Section 3.2, i.e., (1) solve Eq.(3.21) for $\hat{t}_k$'s; and then (2) substitute $\hat{t}_k$'s into Eq.(3.20) to obtain $\hat{a}_k$'s. A grid search subroutine in the Fortran IMSL Library [IMSL, 1990] is performed to find the globally optimal solution of the parameters which maximize the likelihood function.

For simulating the reflected signal $y(nT)$, we choose the set of parameters, $\mathbf{a}$, $\mathbf{t}$, as given in Fig. 2.6, and white Gaussian noise is added on the simulated waveform. The maximum likelihood estimation algorithm is then performed on the simulated, noise-contaminated signals to determine these parameters. Table 3.1 presents the resulting ML estimates at various levels of signal-to-noise ratio (SNR), which is defined as the ratio of signal energy of the weakest peak over the noise power density as give by Eq.(2.26). In this simulation, the third peak is the weakest one. Here we assume that K, the number of reflected pulses (or, the number of layers in a bridge deck), is known in the search for ML solution.

A few observations may be made based on these results. Firstly, the ML estimates of the parameters agree with the true values to a considerable degree, even at lower level of signal-to-noise ratio. Secondly, the accuracy of these estimates does improve, as expected, with the increase of SNR, and the estimation error is almost negligible at high SNR. Thirdly, as SNR decreases, the estimation accuracy for the weaker reflections in the received signal deteriorates much faster than that for the stronger reflections. This suggests that, below certain level of SNR, there is a so-called threshold effect for the maximum likelihood estimation, where a slight decrease in SNR can cause a significant increase in estimation error. This usually occurs at low SNR level. Note that for a given level of noise power, the weaker reflections will have lower SNR value than the stronger reflections. We will have more detailed discussion on this threshold effect later in the Chapter 5, when we study the performance of various estimators.

From the estimated parameters as given in Table 3.1, we may reconstruct the reflected waveforms by substituting the estimated $\hat{a}_k$'s and $\hat{t}_k$'s back into Eq.(3.4) (ignoring the noise term). This waveform is referred to as estimated waveform, denoted as $\hat{y}(t)$, and can be written as

$$\hat{y}(t) = \sum_{k=1}^{K} \hat{a}_k s(t - \hat{t}_k), \tag{3.22}$$

where $s(t)$ is given by Eq.(3.5). The waveforms so obtained for three different levels of SNR are illustrated in Fig. 3.1, Fig. 3.2, and Fig. 3.3, where the true (noise-free) and the noisy input waveforms are plotted along with the estimated waveform for a comparison.

The error, defined as the difference between the estimated and the true waveforms, is given by

$$e(t) = \hat{y}(t) - \sum_{k=1}^{K} a_k s(t - t_k).$$

The errors associated with the waveforms in Fig. 3.1, Fig. 3.2 and Fig. 3.3 are all depicted in Fig. 3.4. Again, we can see that there is a high degree of agreement between the true and the estimated waveforms, and in fact, there is no noticeable discrepancy between the two when the simulated input signal contains no visible noise as shown in Fig. 3.1 or Fig. 3.4. With the decrease in SNR, the the estimates become less accurate, as shown clearly in Fig. 3.4. The observations made on the Table 3.1 are also applicable here.

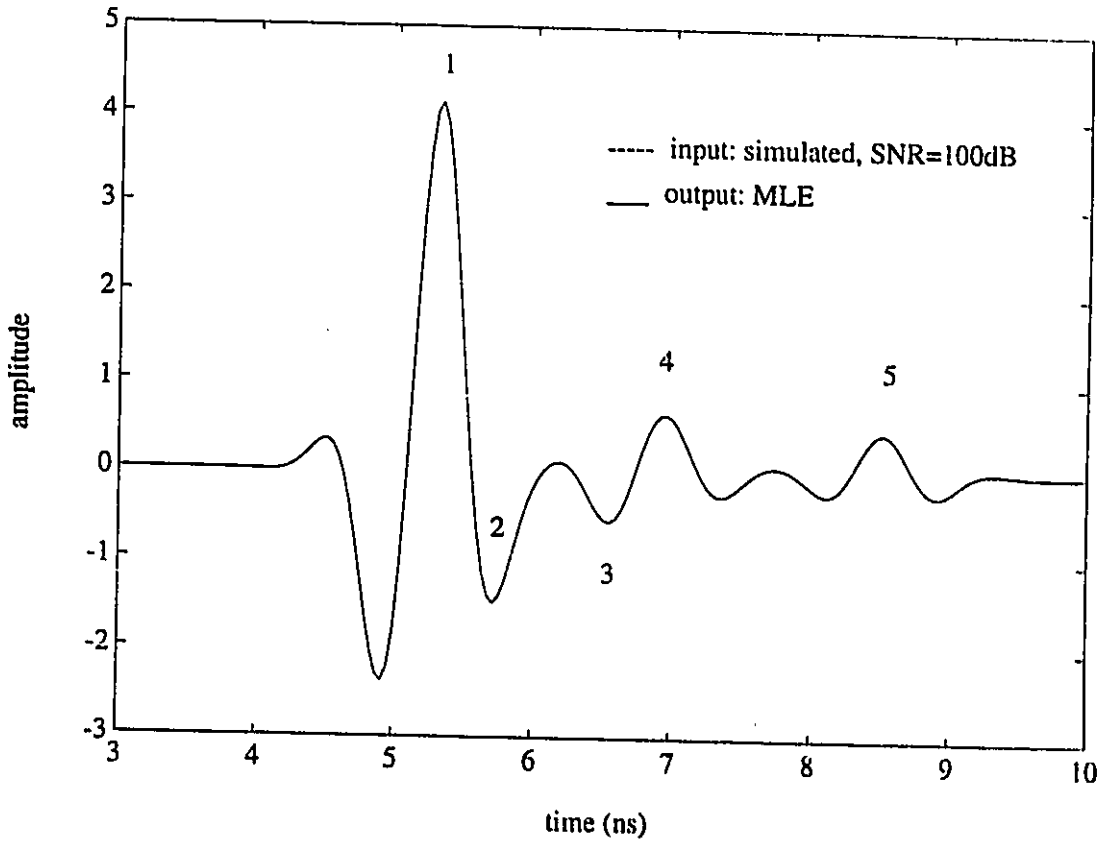

(The numbers mark the peak locations in the input.)

Figure 3.1: ML estimation of simulated waveform (SNR_3=100 dB).

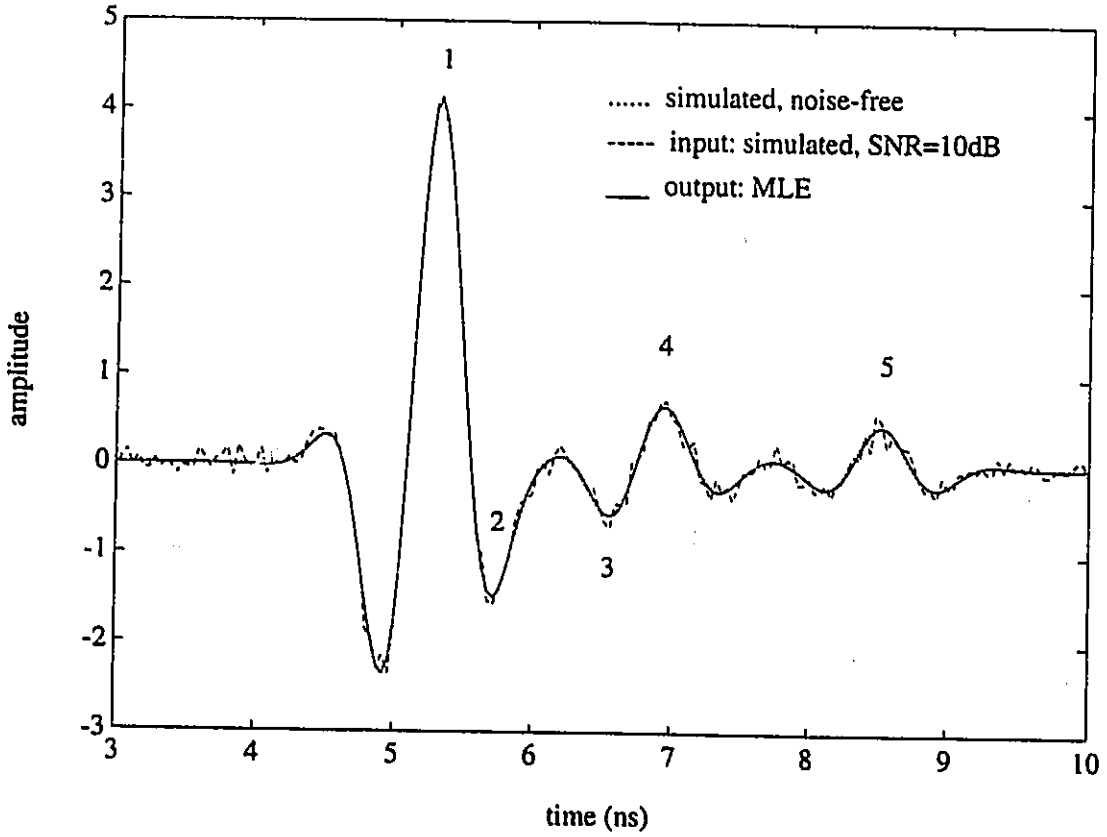

(The numbers mark the peak locations in the input.)

Figure 3.2: ML estimation of simulated waveform (SNR_3=10 dB).

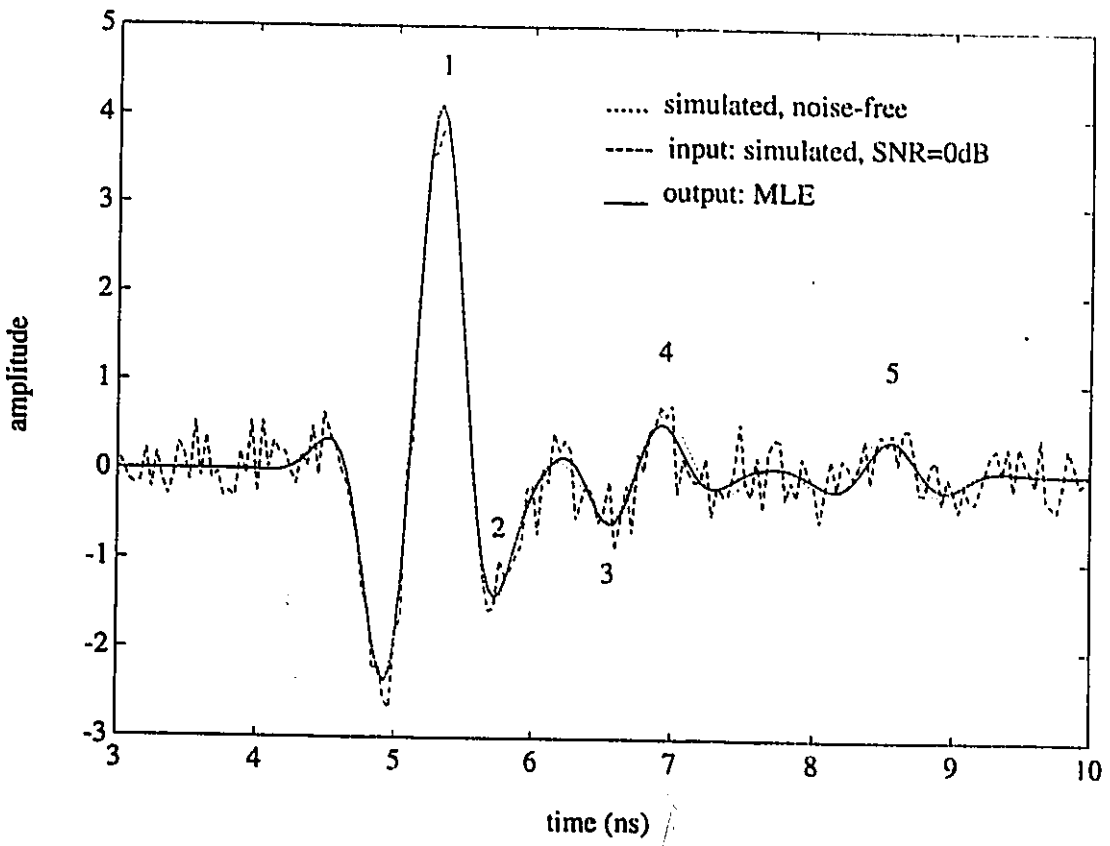

(The numbers mark the peak locations in the input.)

Figure 3.3: ML estimation of simulated waveform (SNR_3=0 dB).

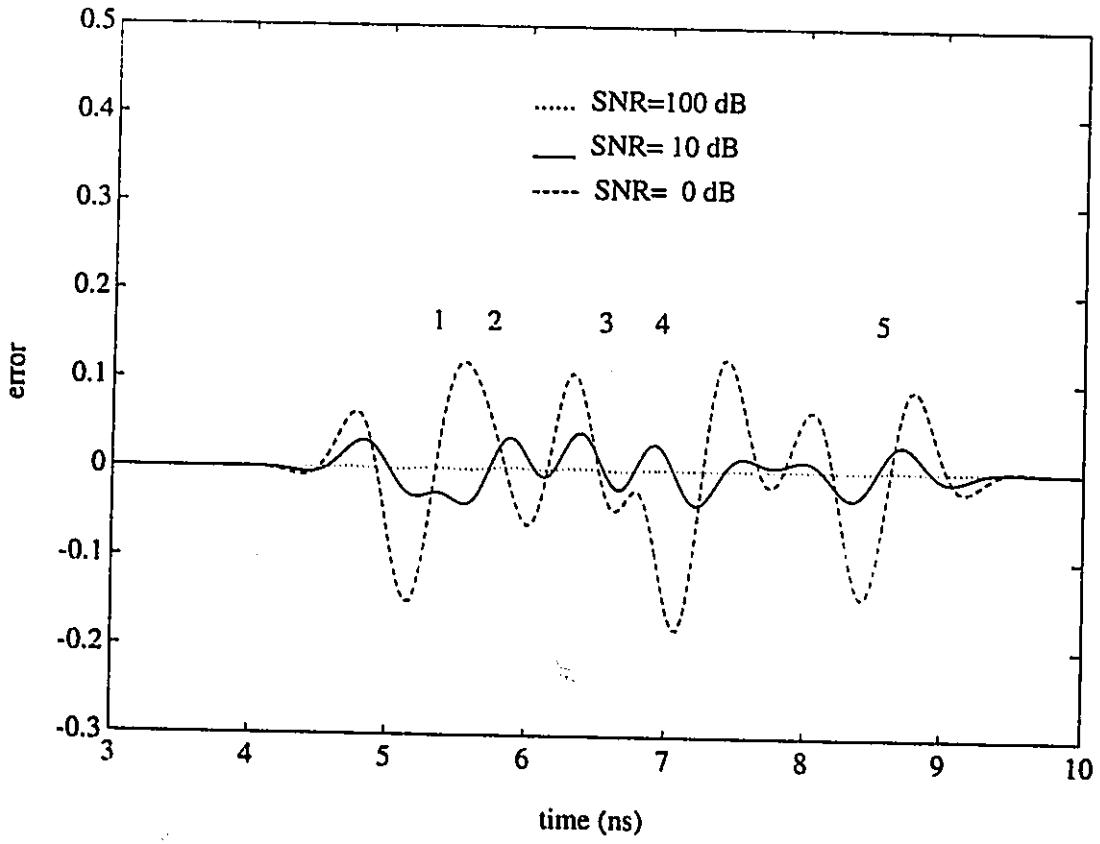

(The numbers mark the peak locations in the input.)

Figure 3.4: Error in the estimated waveforms.

Table 3.1: ML estimated parameters of simulated signals.

Peak no.		1	2	3	4	5
true	t_k	5.310	5.690	6.530	6.960	8.510
parameters	a_k	0.450	0.097	-.037	0.044	0.045
estimated	$\hat{t}_k$	5.3101	5.6906	6.5310	6.9596	8.5102
$\mathrm{SNR}_3 = 100dB$	$\hat{a}_k$	0.4501	.09698	-.03700	.04399	.04500
estimated	$\hat{t}_k$	5.3119	5.7028	6.5671	6.9369	8.5207
$\mathrm{SNR}_3 = 10dB$	$\hat{a}_k$	.4457	.09277	-.03520	.04745	.04477
estimated	$\hat{t}_k$	5.3148	5.7251	6.6730	6.8739	8.5449
$\mathrm{SNR}_3 = 0dB$	$\hat{a}_k$	.4355	.08547	-.04965	.06843	.04521

3.4 ML Estimation for Real Reflected Signals

In this section, we will give an example of applying the maximum likehood method to the estimation of reflection coefficients and time delays for real reflected signal from a bridge deck. The real signal here, as shown in Fig. 3.5, is the same one that is displayed in Fig. 1.3. Note that the MLE procedure outlined in Section 3.2 is also applicable to the estimation for real signals.

The resulting estimates of a_k's and t_k's are summarized in Table 3.2. Here, the value of K is tentatively set to be 5 in searching for the maximum likelihood solution. Since the true values of the signal parameters are unknown in this case, no comparison can be made between the estimated and true values. Nevertheless, we may still reconstruct the reflected waveform from the estimated parameters by using Eq.(3.22), as we have done for the simulated signals. The waveform so obtained is illustrated in Fig. 3.5, along with the real reflected signal. As shown in Fig. 3.6, the difference between the two is insignificant. This example demonstrates the capability of the maximum likelihood method.

Table 3.2: ML estimated parameters of real signal.

Peak no.	1	2	3	4	5
$\hat{t}_k$	5.314	5.694	6.534	6.961	8.508
$\hat{a}_k$	0.04510	0.09659	-.03665	0.04422	0.04533

3.5 Summary

Based on the the parametric model of the reflected signals developed in Chapter 2, the maximum likelihood method is formulated and applied to estimating the characteristic parameters of the signal, namely, a_k's and t_k's. The ML method is a widely used parameter estimation technique because of its superior statistical properties. The computer simulation results demonstrate that the ML method is capable of resolving very closely spaced arrivals in the reflected signals. For the simulated signals, the

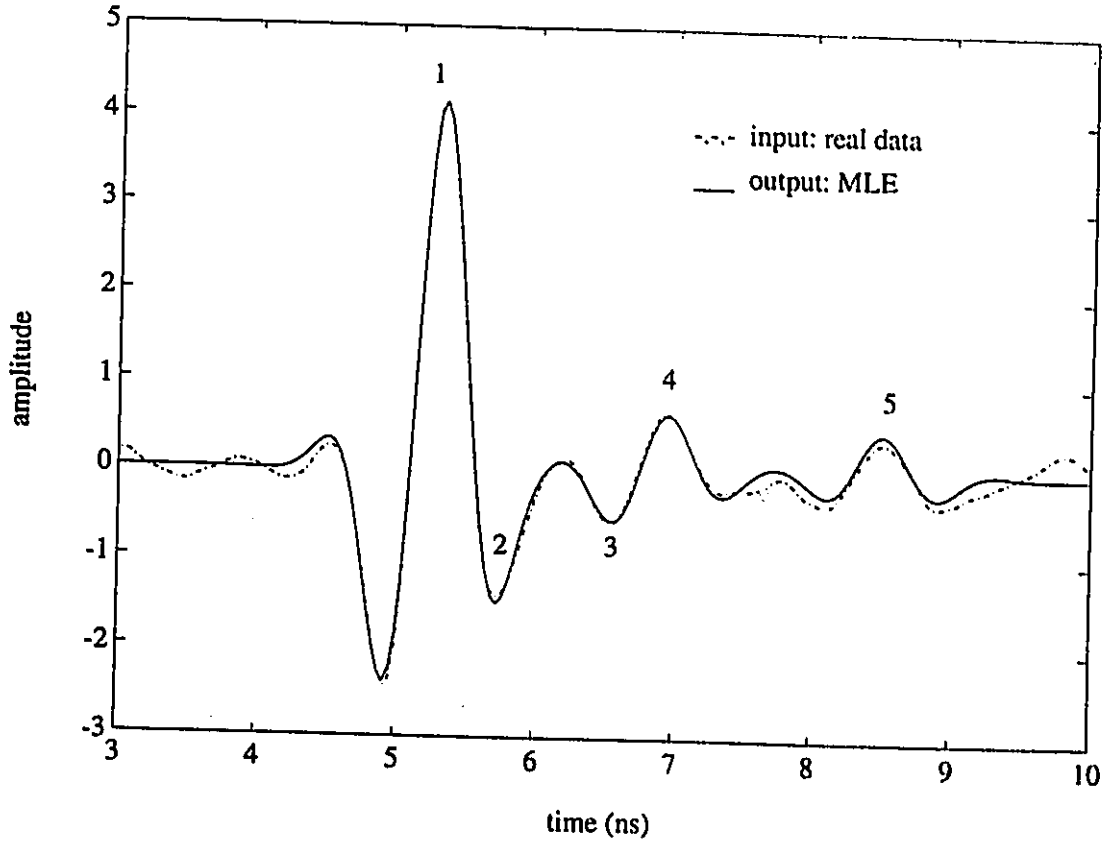

(The numbers mark the peak locations in the output.)

Figure 3.5: ML estimation of real radar waveform.

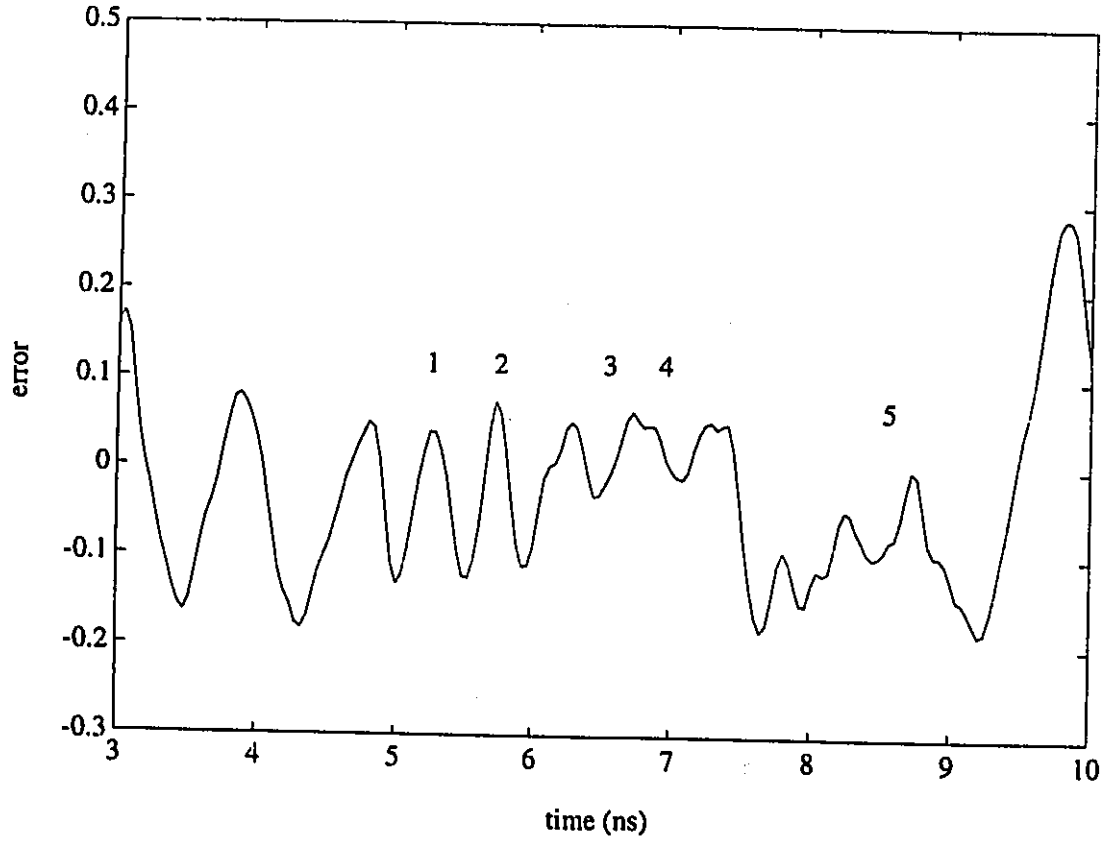

(The numbers mark the peak locations in the output.)

Figure 3.6: Difference between the real and estimated waveforms in Fig. 3.5.

ML method gives very accurate estimates of the signal parameters, even at a low SNR level. Moreover, the ML method is also shown to be applied successfully to the estimation of parameters of the real radar signal reflected from a bridge deck. Despite the superior performance of the ML method, there are two major difficulties in its effective use in practice: firstly, it requires the explicit knowledge of the probability density function of the received signals which may not be always available; and secondly, the ML estimation usually involves a nonlinear optimization procedure where the iterative search for a globally optimal solution can be quite time-consuming. Therefore, it is desirable to develop a new estimation technique which is able to provide a performance comparable to that of the ML method, yet computationally more efficient.

Chapter 4

Eigenstructure-Based Method for Parameter Estimation

A very important topic in array signal processing is the determination of the directions of arrival (DOA) of incident signals to an array of sensors. Many techniques have been proposed for the estimation of DOA [Nickel, 1987]. Among them, the MUSIC (for MUtiple SIgnal Classification) algorithm [Schmidt, 1986] offers a very elegant and efficient solution to the problem, and is capable of providing estimation performance that is comparable to that of the ML method. Yet, it does not suffer from the requirement of the large amount of computation and the initial value problem, which are the two major obstacles to the effective use of ML methods in many applications. A brief description of the MUSIC algorithm will be provided in the context of a linear sensor array. The success of the MUSIC algorithm is largely due to its exploitation of the eigenstructure of signal covariance matrix. This principle may be extended to the problem of our concern. A step by step account will be given to illustrate the development of a new eigenstructure-based estimation technique for the reflected radar signal under consideration. Examples will be also presented to validate the new method.

4.1 Eigenstructure-Based Estimation in Array Signal Processing

4.1.1 Statement of Problem

Consider a linear uniform array composed of M sensors placed at equal intervals, d, as illustrated in Fig. 4.1. Assume that K narrowband plane wave signals, of wavelength λ, impinge on the array from different directions $\theta_1, \theta_2, \ldots, \theta_K$. As required by spatial sampling theorem [Steinberg, 1976], the inter-sensor distance, d, is usually chosen such that $d \leq \lambda$ to eliminate spatial ambiguity. Let $x_k(t)$ denote the waveform of the kth impinging signal, $y_m(t)$ the signal received at the mth sensor, and $v_m(t)$ the noise at the mth sensor. It follows that the complex envelopes of the received signals can be expressed by

$$\mathbf{y}(t) = \sum_{k=1}^{K} \mathbf{a}(\theta_k)\, x_k(t) + \mathbf{v}(t), \tag{4.1}$$

where

$$\begin{aligned}
\mathbf{y}(t) &= [y_1(t), \ldots, y_M(t)]^T \in C^{M\times 1}, \\
\mathbf{v}(t) &= [v_1(t), \ldots, v_M(t)]^T \in C^{M\times 1}, \\
\mathbf{a}(\theta_k) &= [1, e^{-j\phi_k}, \ldots, e^{-j(M-1)\phi_k}]^T \in C^{M\times 1}.
\end{aligned}$$

where $C^{m\times n}$ denotes the set of all $m \times n$ matrices with complex elements, $\mathbf{a}(\theta_k)$ is the 'steering vector' of the array towards direction θ_k, and

$$\phi_k = \frac{2\pi d}{\lambda} \sin\theta_k. \tag{4.2}$$

is related to the propagation delay between two adjacent sensors for the signal arriving from the direction θ_k.

Define a source signal vector $\mathbf{x}(t)$ and steering matrix $\mathbf{A}(\Theta)$ as

$$\begin{aligned}
\mathbf{x}(t) &= [x_1(t), \ldots, x_q(t)]^T \in C^{K\times 1}, \\
\mathbf{A}(\Theta) &= [\mathbf{a}(\theta_1), \ldots, \mathbf{a}(\theta_K)] \in C^{M\times K}.
\end{aligned}$$

Then, Eq.(4.1) can be rewritten in matrix notation, i.e.,

$$\mathbf{y}(t) = \mathbf{A}(\Theta)\mathbf{s}(t) + \mathbf{v}(t). \tag{4.3}$$

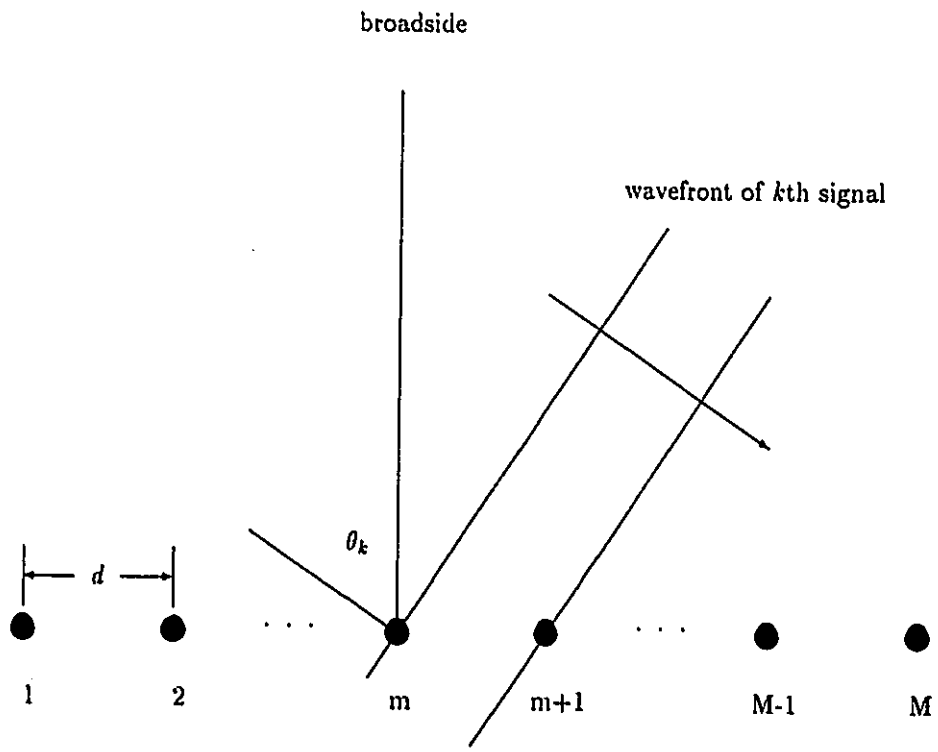

Figure 4.1: Geometry of a linear, uniform sensor array.

Suppose that the received signal vector $\mathbf{y}(t)$ is sampled at N time instances $t_1, \ldots, t_N$ (or, N snapshots, not necessarily in equal sampling intervals). The primary goal of DOA estimation is to determine the incident angles, $\theta_1, \ldots, \theta_K$, of the source signals for given observed data samples $\{\mathbf{y}(t_n),\ n = 1, 2, \ldots, N\}$.

4.1.2 Eigen-decomposition and Noise Subspace

In order to solve the problem of DOA estimation as addressed above, we make following assumptions:

A1. The number of signals is known and is smaller than the number of senors, namely, $K < M$.

A2. The source signal $\mathbf{x}(t)$ is a stationary random process, with zero mean and positive definite covariance matrix $\mathbf{R_X} = \mathrm{E}[\mathbf{x}(t)\mathbf{x}^\dagger(t)]$, where the superscript $\dagger$ designates the operation of complex-conjugate transpose (or, Hermitian transpose).

A3. The noise process $\mathbf{v}(t)$ is stationary and uncorrelated both temporally and spatially, and is independent of the signal $\mathbf{x}(t)$. It is of zero mean and covariance matrix $\mathbf{R_V} = \mathrm{E}[\mathbf{v}(t)\mathbf{v}^\dagger(t)] = \sigma^2\mathbf{I}$, with σ^2 being the noise variance.

Under these assumptions, the spatial covariance matrix of received signal $\mathbf{y}(t)$ is found to be

$$\begin{aligned} \mathbf{R_Y} &= \mathrm{E}[\mathbf{y}(t)\mathbf{y}^\dagger(t)] \\ &= \mathbf{A}(\Theta)\mathbf{R_X}\mathbf{A}^\dagger(\Theta) + \sigma^2\mathbf{I}. \end{aligned} \tag{4.4}$$

Because the covariance matrix $\mathbf{R_V}$ is Hermitian, i.e., $\mathbf{R_Y^\dagger} = \mathbf{R_Y}$, and positive definite (as long as $\sigma^2 \neq 0$), all its eigenvalues are real and positively valued and its eigenvectors are mutually orthogonal [Lancaster, 1985]. Let $\lambda_1 \geq \lambda_2 \geq \cdots \geq \lambda_M > 0$ be the eigenvalues of $\mathbf{R_Y}$, and $\mathbf{q}_1, \ldots, \mathbf{q}_M$ be the corresponding orthonormal eigenvectors, namely,

$$< \mathbf{q}_i, \mathbf{q}_j >= \mathbf{q}_i^\dagger \cdot \mathbf{q}_j = \delta_{ij}$$

where δ_{ij} is the Kronecker delta. Since $\mathbf{A}\mathbf{R_X}\mathbf{A}^\dagger$ is positive semi-definite with rank $= K$, it follows that

$$\begin{aligned} \lambda_m &= \alpha_m + \sigma^2, \qquad \text{for } m = 1, \ldots, K; \\ \lambda_m &= \sigma^2, \qquad \text{for } m = K+1, \ldots, M; \end{aligned}$$

where $\alpha_m \geq 0$, $m = 1, \ldots, K$, are the non-zero eigenvalues of matrix $\mathbf{A}\mathbf{R_X}\mathbf{A}^\dagger$.

Also define

$$\begin{aligned} \mathbf{Q_a} &= (\mathbf{q}_1, \ldots, \mathbf{q}_K); \\ \mathbf{Q_v} &= (\mathbf{q}_{K+1}, \ldots, \mathbf{q}_M); \\ \mathbf{Q} &= (\mathbf{Q_a}, \mathbf{Q_v}) = (\mathbf{q}_1, \ldots, \mathbf{q}_M). \end{aligned} \tag{4.5}$$

Let $\mathbf{\Lambda_a} = \mathrm{diag}(\alpha_1, \ldots, \alpha_K, 0, \ldots, 0)$ $\mathbf{Q_a} = (\mathbf{q}_1, \ldots, \mathbf{q}_K)$, $\mathbf{Q_v} = (\mathbf{q}_{K+1}, \ldots, \mathbf{q}_M)$, and $\mathbf{Q} = (\mathbf{q}_1, \ldots, \mathbf{q}_M)$. By the definition of eigen-decomposition,

$$\mathbf{Q}^\dagger \mathbf{R_y} \mathbf{Q} = \mathbf{\Lambda_a} + \sigma^2 \mathbf{I}. \tag{4.6}$$

From Eq.(4.4) and the fact $\mathbf{Q}^\dagger\mathbf{Q} = \mathbf{I}$, we have

$$\mathbf{Q}^\dagger \mathbf{R_y} \mathbf{Q} = \mathbf{Q}^\dagger \mathbf{A}\mathbf{R_X}\mathbf{A}^\dagger \mathbf{Q} + \sigma^2 \mathbf{I}. \tag{4.7}$$

Therefore,

$$\mathbf{Q}^\dagger \mathbf{A}\mathbf{R_X}\mathbf{A}^\dagger \mathbf{Q} = \mathbf{\Lambda_a}. \tag{4.8}$$

On the other hand,

$$\begin{aligned} \mathbf{Q}^\dagger \mathbf{A}\mathbf{R_X}\mathbf{A}^\dagger \mathbf{Q} &= [\mathbf{Q_a}, \mathbf{Q_v}]^\dagger \mathbf{A}\mathbf{R_X}\mathbf{A}^\dagger [\mathbf{Q_a}, \mathbf{Q_v}] \\ &= \begin{bmatrix} \mathbf{Q_a^\dagger}\mathbf{A}\mathbf{R_X}\mathbf{A}^\dagger\mathbf{Q_a} & \mathbf{Q_a^\dagger}\mathbf{A}\mathbf{R_X}\mathbf{A}^\dagger\mathbf{Q_v} \\ \mathbf{Q_v^\dagger}\mathbf{A}\mathbf{R_X}\mathbf{A}^\dagger\mathbf{Q_a} & \mathbf{Q_v^\dagger}\mathbf{A}\mathbf{R_X}\mathbf{A}^\dagger\mathbf{Q_v} \end{bmatrix}. \end{aligned} \tag{4.9}$$

Compare the right-hand sides of Eq.(4.8) and Eq.(4.9). It is obvious that

$$\mathbf{Q_v^\dagger}\mathbf{A}\mathbf{R_X}\mathbf{A}^\dagger\mathbf{Q_v} = 0.$$

Because $\mathbf{R_X}$ is positive definite by assumption A2, this is equivalent to

$$\mathbf{A}^\dagger \mathbf{Q_v} = 0. \tag{4.10}$$

In other words, the space spanned by $(\mathbf{q}_{K+1}, \ldots, \mathbf{q}_M)$ (noise subspace $\mathcal{N}$) is orthogonal to the space spanned by $(\mathbf{a}(\theta_1), \ldots, \mathbf{a}(\theta_K))$ (signal subspace $\mathcal{S}$).

The operator that projects an M-dimensional vector ($\in C^{M\times 1}$) onto the noise subspace $\mathcal{N}$ is given by

$$\mathbf{P}_N = \mathbf{Q_v}[\mathbf{Q_v^\dagger}\mathbf{Q_v}]^{-1}\mathbf{Q_v^\dagger} \tag{4.11}$$

Therefore, from the orthogonality of the signal and noise subspaces, it follows that

$$\mathbf{Q_V}[\mathbf{Q_V^\dagger Q_V}]^{-1}\mathbf{Q_V^\dagger}\mathbf{a}(\theta) = 0, \qquad \text{for } \theta = \theta_1, \ldots, \theta_K,$$

or equivalently,

$$\mathbf{a}^\dagger(\theta)\mathbf{Q_V}[\mathbf{Q_V^\dagger Q_V}]^{-1}\mathbf{Q_V^\dagger}\mathbf{a}(\theta) = 0, \qquad \text{for } \theta = \theta_1, \ldots, \theta_K. \tag{4.12}$$

For a M-sensor array, the left hand side of Eq.(4.12) may be regarded as a $(2M-1)$th order polynomial of $e^{-j\phi}$ with known coefficients since all the elements of matrix $\mathbf{Q_V}$ are known. Once the values of ϕ are computed, then the estimates of θ can be readily obtained, as ϕ and θ are related by Eq.(4.2). This approach is commonly referred to as *root-MUSIC* [Wong, 1988; Bhaskar, 1989]. Solving the polynomial is relatively easier and it does not require very extensive computation as in the case of maximum likelihood estimation where some nonlinear, global maximization (minimization) procedure is involved. This is indeed a major advantage of MUSIC algorithm over the maximum mikelihood method in the DOA estimation.

4.1.3 Computation Procedure of MUSIC Algorithm

In practice, however, the exact signal covariance matrix $\mathbf{R_y}$ is rarely known in advance, and thus has to be estimated from the received data $\{\mathbf{y}(t)\}$. A commonly used estimator of $\mathbf{R_y}$ is given by

$$\hat{\mathbf{R}}_\mathbf{y} = \frac{1}{N}\sum_{t=1}^{N}\mathbf{y}(t)\mathbf{y}^\dagger(t). \tag{4.13}$$

Based on the discussion above, the procedure of using MUSIC algorithm to estimate the angles of arrival from measured data samples can be summarized in the following four steps.

1. Estimate the data covariance matrix $\hat{\mathbf{R}}_\mathbf{y}$ by Eq.(4.13);
2. Eigendecompose $\hat{\mathbf{R}}_\mathbf{y}$, and take the eigenvectors which correspond to the smallest $M-K$ eigenvalues to construct the matrix $\mathbf{Q_V}$ as defined by Eq.(4.5);
3. Form the projection matrix $\mathbf{P}_N$ from $\mathbf{Q_V}$, as given in Eq.(4.11);
4. Solve Eq.(4.12) for the K angular parameters $\theta_1, \theta_2, \ldots, \theta_K$.

4.2 Derivation of Eigenstructure-Based Estimation Method

4.2.1 Structure of Reflected Radar Signals

Now, we turn our attention back to the problem of parameter estimation from reflected radar signals. Our goal is to develop a MUSIC-like, eigenstructure-based algorithm for an efficient processing of received data.

Recall that the model of reflected radar waveform can be expressed as

$$y(nT) = \sum_{k=1}^{K} a_k s(nT - t_k) + v(nT), \qquad n = 1, \ldots, N_s. \tag{4.14}$$

Let $S(e^{j\omega}), Y(e^{j\omega})$, and $V(e^{j\omega})$ be the Fourier transform of $y(nT), s(nT)$ and $v(nT)$, respectively. Taking the discrete Fourier transform (DFT) of both sides of Eq.(4.14) yields

$$Y(e^{jn\omega_0}) = \sum_{k=1}^{K} a_k e^{-jn\phi_k} S(e^{jn\omega_0}) + V(e^{jm\omega_0}), \qquad n = 1, \ldots, N_s, \tag{4.15}$$

or, in a short notation,

$$Y(n) = \sum_{k=1}^{K} a_k z_k^n S(n) + V(n), \tag{4.16}$$

where $\omega_0 = 2\pi/N_s$, $\phi_k = \omega_0 t_k/T$, and $z_k^n = e^{-jn\phi_k}$. By comparing Eq.(4.15) with Eq.(4.1), we realize immediately that there are three differences between our signal model and that for the MUSIC algorithm. Firstly, the source signals in our case, $a_k S(e^{jn\omega_0})$, are not narrowband random processes; instead, they are all deterministic with known spectrum $S(e^{jn\omega})$ as given by Eq.(2.18). Secondly, $a_k S(e^{jn\omega_0})$ are linearly dependent for different k's. Thirdly, the sequence $\{Y(e^{jn\omega_0})\}$ is equivalent to only a single snapshot as in the case of array signal collection. The last two differences prevent us from obtaining a full-rank data covariance matrix $\mathbf{R_y}$ directly from Eq.(4.13). This rank deficiency problem is also encountered in the DOA estimation when the source signals are coherent [Evens, 1981; Pillai, 1989]. To overcome this problem, some spatial smoothing operation may be performed before the implementation of MUSIC algorithm. Here, we apply the idea of spatial smoothing to our problem. Nevertheless, it is performed in the frequency domain, instead of in the spatial domain. By carrying out the 'spectral averaging', we can overcome the difficulties arising from the last two differences.

4.2.2 Frequency Domain Smoothing

Partition the sequence $\{Y(e^{jn\omega_0}), n = 1, 2, \ldots, N_s\}$ into M overlapping segments (subsequences), with $N\,(K < N < N_s)$ data samples in each segment and $M = N_s - N + 1$. Now, define $\mathbf{y}_m$ as the data vector of samples $\{Y(n)\}$ from the mth subsequence, namely,

$$\mathbf{y}_m = [Y(m), \ldots, Y(m+N-1)]^T, \qquad m = 1, \ldots, M. \tag{4.17}$$

Similarily, we can define, for $m = 1, \ldots, M$,

$$\begin{aligned} \mathbf{v}_m &= [V(m), \ldots, V(m+N-1)]^T, \\ \mathbf{S}_m &= \mathrm{diag}[S(m), \ldots, S(m+N-1)], \end{aligned}$$

and

$$\begin{aligned} \mathbf{a} &= [a_1, \ldots, a_K]^T, \\ \mathbf{Z} &= \mathrm{diag}[z_1, \ldots, z_K], \\ \mathbf{d}(t_k) &= [z_k, z_k^2, \ldots, z_k^N]^T, \\ \mathbf{D} &= \mathbf{D}(\mathbf{t}) = [\mathbf{d}(t_1), \ldots, \mathbf{d}(t_K)]. \end{aligned} \tag{4.18}$$

Then, the signal vector $\mathbf{y}_m$ can be written as

$$\mathbf{y}_m = \mathbf{S}_m \mathbf{D} \mathbf{Z}^{m-1} \mathbf{a} + \mathbf{v}_m. \tag{4.19}$$

Recall that $S(e^{j\omega})$ is real, and non-zero for any ω, hence $\mathbf{S}_m$ is real and non-singular. Pre-multiplying $\mathbf{y}_m$ by $\mathbf{S}_m^{-1}$ results in

$$\mathbf{x}_m = \mathbf{S}_m^{-1}\mathbf{y}_m = \mathbf{D}\mathbf{Z}^{m-1}\mathbf{a} + \mathbf{u}_m^{-1}, \tag{4.20}$$

where $\mathbf{u}_m = \mathbf{S}_m^{-1}\mathbf{v}_m$. Note that $\mathbf{Z}_m^{\dagger} = \mathbf{Z}_m^{-1}$, and $\mathrm{E}[\mathbf{v_m}\mathbf{v_m}^{\dagger}] = \sigma^2\mathbf{I}_N$. Then the covariance matrix of $\mathbf{x}_m$ can be found to be

$$\begin{aligned} \mathbf{R}_{\mathbf{x}_m} &= \mathrm{E}[\mathbf{x}_m\mathbf{x}_m{}^{\dagger}] \\ &= \mathbf{D}\mathbf{Z}^{m-1}\mathbf{a}\mathbf{a}^{\dagger}\mathbf{Z}^{-m+1}\mathbf{D}^{\dagger} + \sigma^2\mathbf{S}_m^{-2}. \end{aligned} \tag{4.21}$$

Since the rank of $\mathbf{D}\mathbf{Z}^{m-1}\mathbf{a}\mathbf{a}^{\dagger}\mathbf{Z}^{-m+1}\mathbf{D}^{\dagger}$ is only one, 'spectral averaging' is performed over M subsequences. This results in a modified data covariance matrix given by

$$\mathbf{R}_{\mathbf{x}} = \frac{1}{M}\sum_{m=1}^{M}\mathbf{R}_{\mathbf{x}_m} = \mathbf{D}\mathbf{R}_{\mathbf{s}}\mathbf{D}^{\dagger} + \sigma^2\mathbf{G}, \tag{4.22}$$

where

$$\mathbf{G} = \frac{1}{M}\sum_{m=1}^{M} \mathbf{S}_m^{-2};$$

$$\mathbf{R_S} = \frac{1}{M}\sum_{m=1}^{M} \mathbf{Z}^{m-1}\mathbf{a}\mathbf{a}^{\dagger}\mathbf{Z}^{-m+1}.$$

It can be shown that the modified covariance matrix $\mathbf{R_S}$ is nonsingular with rank=K, if the number of subsequences, M, is greater than or equal to the number of source signals, K [Shan, 1985; Reddi. 1987]. This requirement can be readily satisfied since the number of data sample from a reflected waveform are usually much greater than the number of reflected pulses.

4.2.3 Eigen-decomposition and Projection to Noise Subspace

Equation (4.22) resembles Eq.(4.4) except that $\mathbf{G}$ is not an identity matrix (but diagonal). This can be treated as a colored noise situation, and the generalized eigen-decomposition may be performed on $\mathbf{R_X}$ to determine its noise subsapce. An alternative approach, which we will follow here, is to introduce a pre-whitening operation before the eigen-decomposition. Since $\mathbf{G}$ is positive definite, it can be factorized as $\mathbf{G} = (\mathbf{F}^{-1})^{\dagger}\mathbf{F}^{-1}$. Then the whitening operation can be carried out by simply pre-multiplying Eq.(4.22) by $\mathbf{F}^{\dagger}$, and post-multiplying by $\mathbf{F}$, such that

$$\mathbf{F}^{\dagger}\mathbf{R_X}\mathbf{F} = \mathbf{F}^{\dagger}\mathbf{D}\mathbf{R_S}\mathbf{D}^{\dagger}\mathbf{F} + \sigma^2\mathbf{I}. \tag{4.23}$$

Since rank$(\mathbf{F}^{\dagger}\mathbf{D}\mathbf{R_S}\mathbf{D}^{\dagger}\mathbf{F}) = K < N$, the eigenvalues of $\mathbf{F}^{\dagger}\mathbf{R_X}\mathbf{F}$ satisfy $\lambda_1 \geq \lambda_2 \geq \cdots \geq \lambda_K \geq \lambda_{K+1} = \lambda_{K+2} = \cdots = \lambda_N = \sigma^2$. Let $\mathbf{q_1}, \mathbf{q_2}, \ldots, \mathbf{q}_N$ be the eigenvectors associated with corresponding eigenvalues, and define $\mathbf{Q_V} = [\mathbf{q}_{K+1}, \mathbf{q}_{K+2}, \ldots, \mathbf{q}_N]$. By following the derivation in Section 4.1, it can be shown that

$$\mathbf{Q_V}\mathbf{F}^{\dagger}\mathbf{R_X}\mathbf{F}\mathbf{Q_V} = \mathbf{Q_V}\mathbf{F}^{\dagger}\mathbf{D}\mathbf{R_S}\mathbf{D}^{\dagger}\mathbf{F}\mathbf{Q_V} + \sigma^2\mathbf{I} = \sigma^2\mathbf{I}.$$

Because $\mathbf{R_S}$ is nonsingular, this suggests that

$$\mathbf{D}^{\dagger}\mathbf{F}\mathbf{Q_V} = \mathbf{0}. \tag{4.24}$$

Obviously, the noise subspace spanned by $\mathbf{F}\mathbf{q}_{K+1}, \mathbf{F}\mathbf{q}_{K+2}, \ldots, \mathbf{F}\mathbf{q}_N$ is orthogonal to the signal subspace spanned by the columns of the matrix $\mathbf{D}$. The projection of an N-dimensional vector onto the noise space can be carried out by the operator

$$\begin{aligned}\mathbf{P}_N &= \mathbf{F}\mathbf{Q_V}[(\mathbf{F}\mathbf{Q_V})^{\dagger}\mathbf{F}\mathbf{Q_V}]^{-1}(\mathbf{F}\mathbf{Q_V})^{\dagger} \\ &= \mathbf{F}\mathbf{Q_V}[\mathbf{Q_V}^{\dagger}\mathbf{G}^{-1}\mathbf{Q_V}]^{-1}\mathbf{Q_V}^{\dagger}\mathbf{F}^{\dagger}.\end{aligned} \tag{4.25}$$

It follows that

$$\mathbf{d}^{\dagger}(t)\mathbf{F}\mathbf{Q}_{\mathbf{V}}[\mathbf{Q}_{\mathbf{V}}^{\dagger}\mathbf{G}^{-1}\mathbf{Q}_{\mathbf{V}}]^{-1}\mathbf{Q}_{\mathbf{V}}^{\dagger}\mathbf{F}^{\dagger}\mathbf{d}(t) = 0, \qquad \text{for } t = t_1, \ldots, t_K. \tag{4.26}$$

Equation 4.26 can be easily solved for the parameters, t_k's, in the same way as in the root-MUSIC algorithm for the DOA problem [Wong, 1988; Bhaskar, 1989].

In summary, the eigenstructure-based parameter estimation of the reflected signals can be carried out in following steps.

1. Perform FFT (Fast Fourier Transform) on the sampled radar waveform.
2. Partition the Fourier series into M overlapping segments.
3. Compute the estimate of modified data covariance matrix by

$$\hat{\mathbf{R}}_{\mathbf{X}} = \frac{1}{M}\sum_{m=1}^{M} \mathbf{x}_m \mathbf{x}_m^{\dagger}, \tag{4.27}$$

   where $\mathbf{x}_m$ is defined by Eq.(4.20) .
4. Carry out pre-whitening of $\hat{\mathbf{R}}_{\mathbf{X}}$ by Eq.(4.23).
5. Eigen-decompose $\hat{\mathbf{R}}_{\mathbf{X}}$ and form the projection operator $\mathbf{P}_N$ by Eq.(4.25).
6. Solve Eq.(4.26) for the parameters estimates $\hat{t}_1, \hat{t}_2, \ldots, \hat{t}_K$.
7. Substitute the estimated $\hat{t}_k$'s into Eq.(3.20) to obtain the estimates $\hat{a}_1, \hat{a}_2, \ldots, \hat{a}_K$.

In the derivation of the EB method, the only assumption on the probing pulse is that its Fourier coefficients are non-zero. Therefore, the new algorithm can be directly applied to the more general problems of resolution and estimation of overlapping signals in noise.

4.3 EB Parameter Estimation for Simulated Signals

In this section we apply the eigenstructure-based method developed in the last section to estimating parameter from simulated signals. The signal model as described in Chapter 2 is used for the simulation of the reflected waveforms. The parameters of the simulated signal, as shown in Table 4.1, are chosen to be the same as those in Table 3.1. In the simulation, the given signal samples $\{y(nT)\}$ is first Fourier transformed and partitioned into $M = 20$ overlapping segments to form the signal

covariance matrix R_x. Then, the procedure of the eigenstructure-based algorithm, as outlined in Section 4.2, is followed to estimate the parameters, $\{a_k\}$ and $\{t_k\}$. The resulting parameter estimates under various levels of signal-to-noise ratio are presented in Table 4.1. Note that the levels of SNR in the table are given with respect to the weakest peak, i.e., the 3rd reflected pulse, in the simulated waveform. The number of reflected pulses, K, or, the number of layers in the media, are assumed to be known in the computation for the parameter estimates.

Some observations may be made based on the results as shown in Table 4.1. When the reflected signal contains essentially no noise (SNR=100 dB), the eigenstructure-based method gives the estimates with no error up to 6 digits after decimal point. This result is comparable to, if not better than, the estimates obtained by the ML method which are given in Table 3.1. However, a small amount of noise in the input will increase the estimation error remarkably, as can be seen from the results in the case of SNR=30 dB. At SNR=10 dB, the new method manages to locate 4 out of 5 reflected pulses with good accuracy, but misses the 3rd pulse which is the weakest in the input signal. When the level of SNR drops further to 0 dB, only those relatively strong or well-separated pulses are located, and the estimated parameters are inaccurate. Generally, as the SNR decreases, the estimation error of the eigenstructure-based method deteriorates faster than that of the ML method. A more thorough assessment of estimators error performance will be given in Chapter 5.

As before, we may plot the noise-free reflected waveform with the estimated waveform, to illustrate the effects of estimates' errors on the waveform. The estimated waveform is obtained by Eq.(3.22) using the the estimated parameters $\{\hat{a}_k\}$ and $\{\hat{t}_k\}$ which are given in Table 4.1. These estimated waveforms are illustrated in Fig. 4.2 to Fig. 4.5 for four different levels of SNR.

At SNR=100 dB, the simulated input signal has no visible noise, and the estimated waveform is virtually identical to the true, noise-free waveform. As SNR decreases, the discrepancy between the true waveform and estimated waveform becomes apparent, particularly at the weaker or closely located peaks, as it is evident in Fig. 4.4 and Fig. 4.5. The errors in the estimated waveforms are depicted in Fig. 4.6. They are significantly larger than those of maximum likelihood estimated waveforms.

Table 4.1: Estimated parameters of simulated signals.

Peak no.		1	2	3	4	5
true	t_k	5.310	5.690	6.530	6.960	8.510
parameters	a_k	0.450	0.097	-.037	0.044	0.045
estimated	$\hat{t}_k$	No error observed up to 5 digits.				
SNR_3=100dB	$\hat{a}_k$	No error observed up to 5 digits.				
estimated	$\hat{t}_k$	5.3013	5.6176	6.6052	6.8542	8.5118
SNR_3=30dB	$\hat{a}_k$	.4244	.0877	-.0452	.0463	.0446
estimated	$\hat{t}_k$	5.2795	5.6130	6.8153	8.5199	11.5707
SNR_3=10dB	$\hat{a}_k$	.4423	.1260	.0380	.0451	.0003
estimated	$\hat{t}_k$	.9168	5.2780	6.5773	6.7572	8.5016
SNR_3=0dB	$\hat{a}_k$	.0190	.3709	-.0515	.0262	.0569

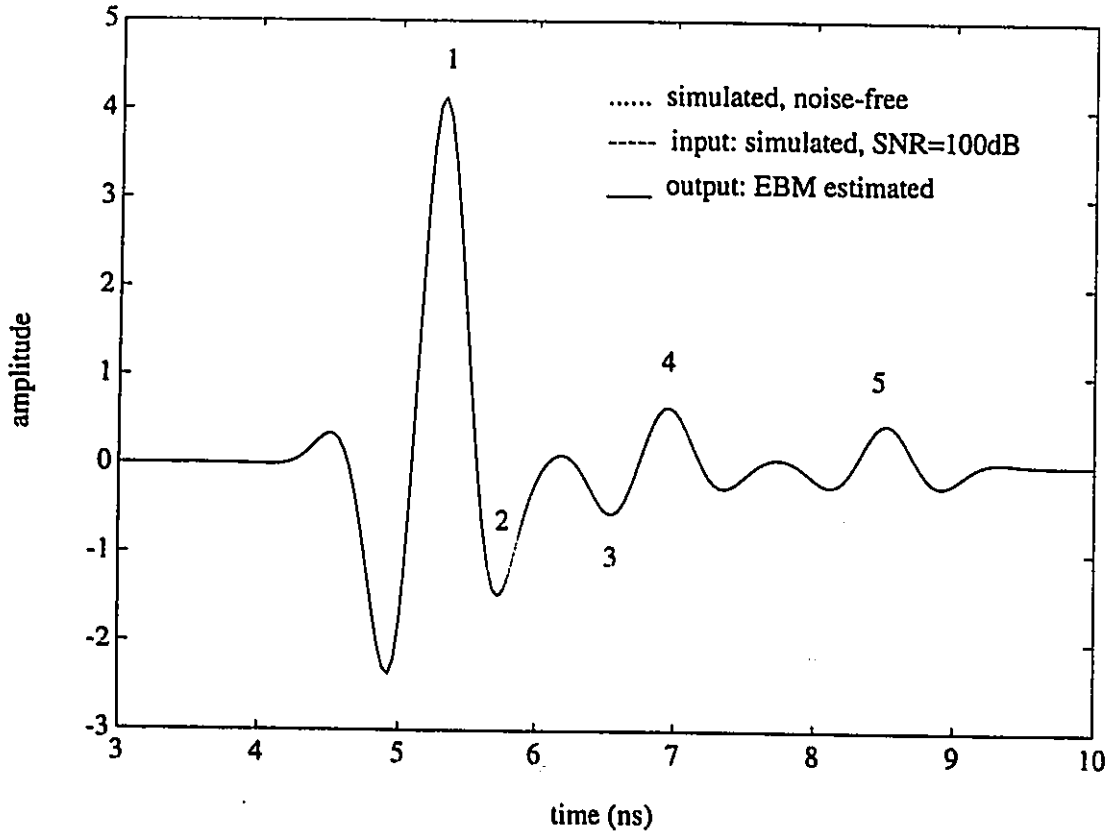

(The numbers mark the peak locations in the input.)

Figure 4.2: EB estimation of simulated waveform (SNR_3=100dB).

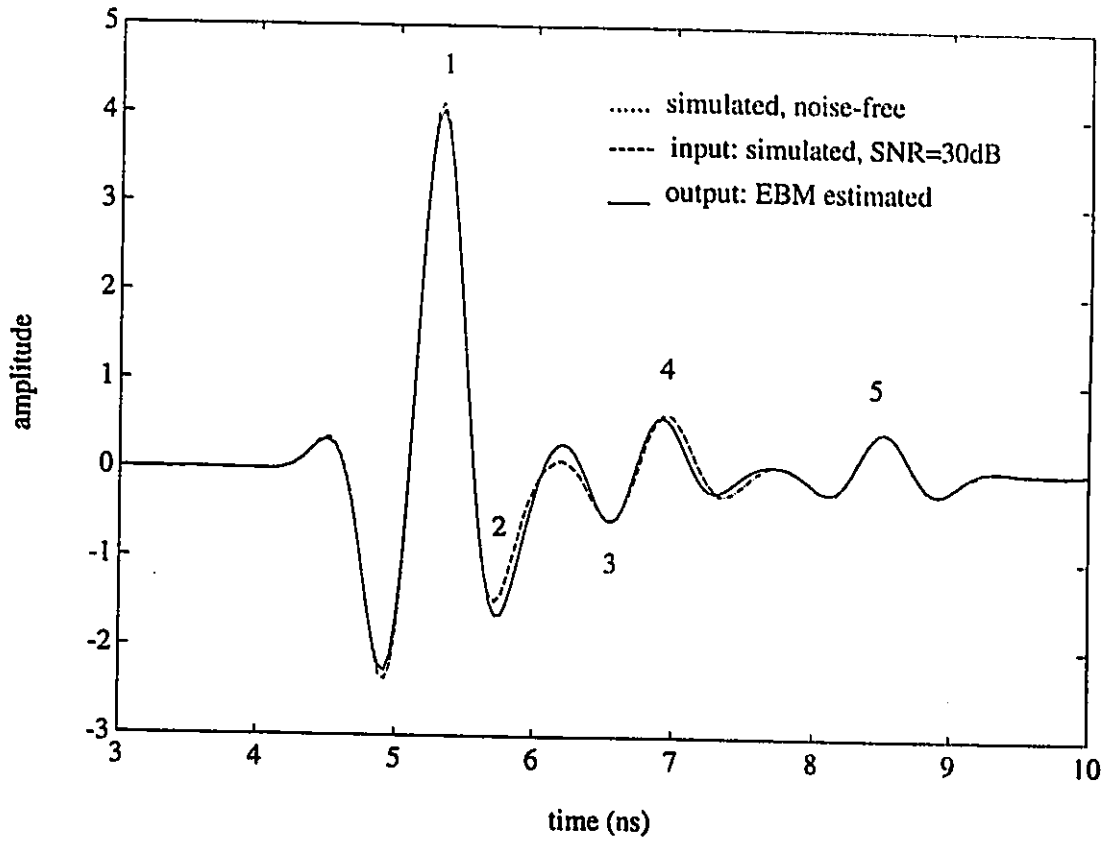

(The numbers mark the peak locations in the input.)

Figure 4.3: EB estimation of simulated waveform (SNR_3=30dB).

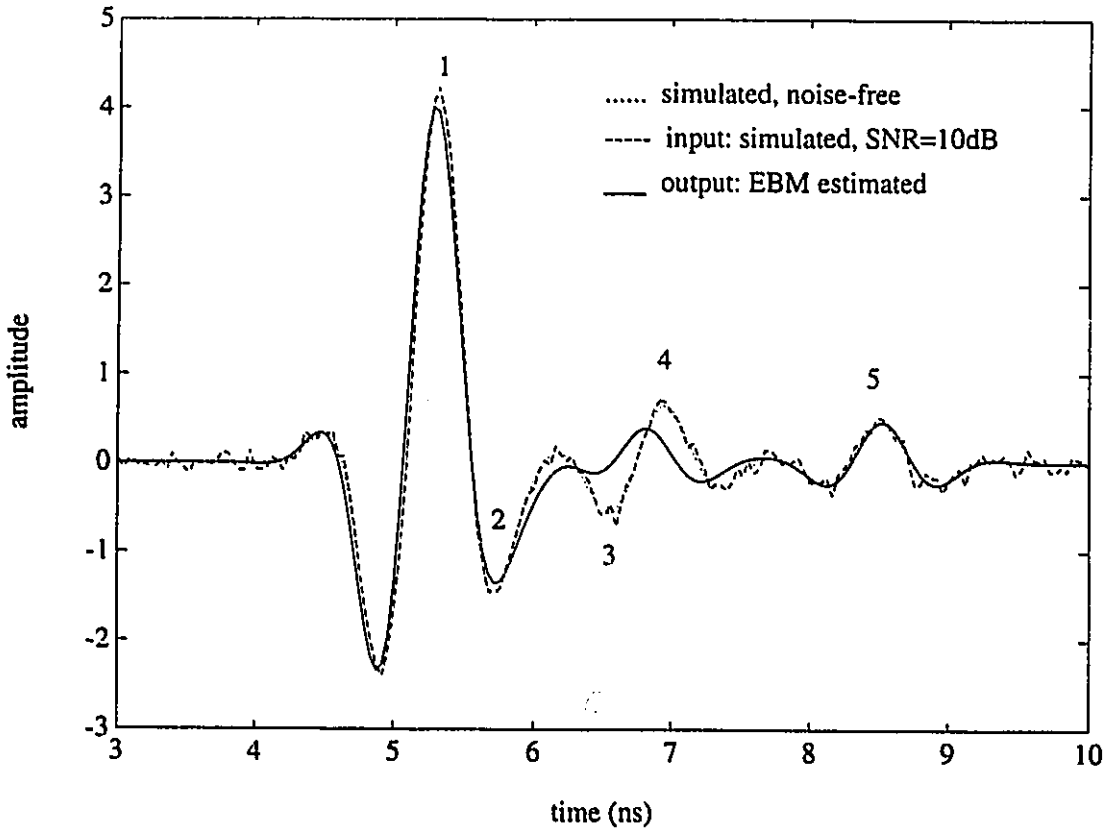

(The numbers mark the peak locations in the input.)

Figure 4.4: EB estimation of simulated waveform (SNR_3=10dB).

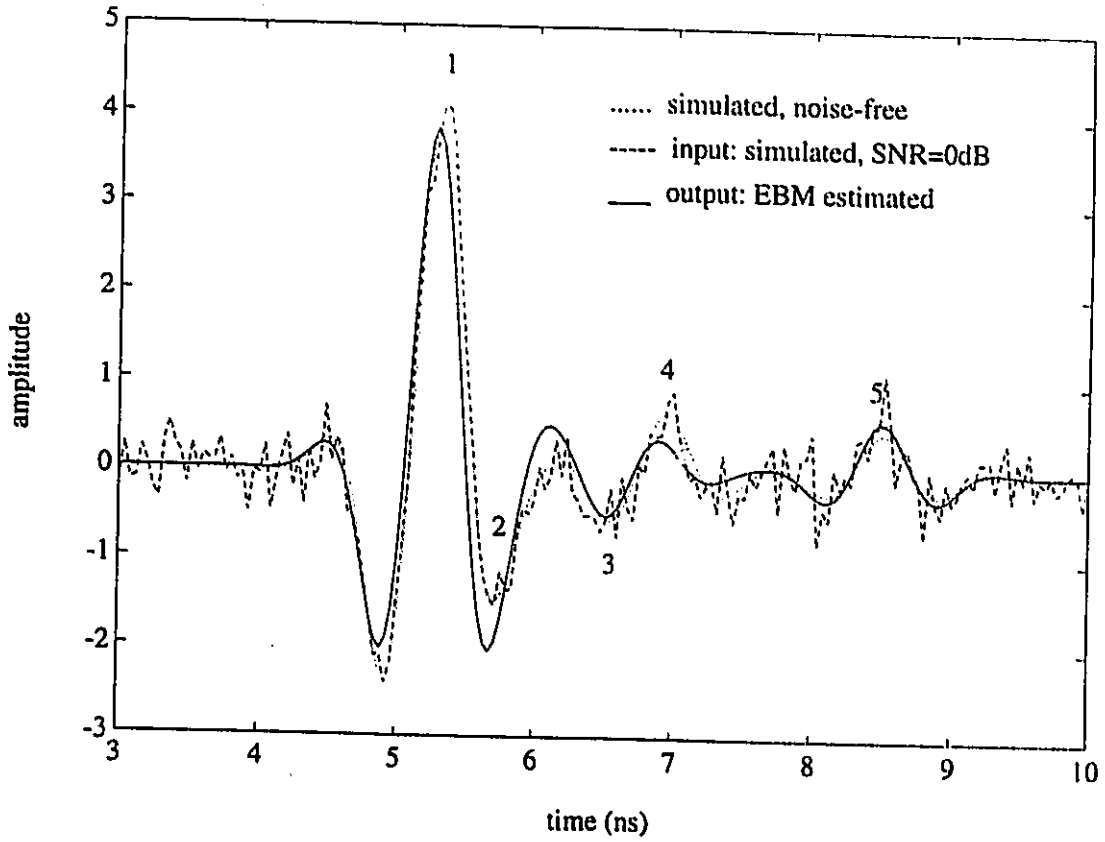

(The numbers mark the peak locations in the input.)

Figure 4.5: EB estimation of simulated waveform (SNR_3=0dB).

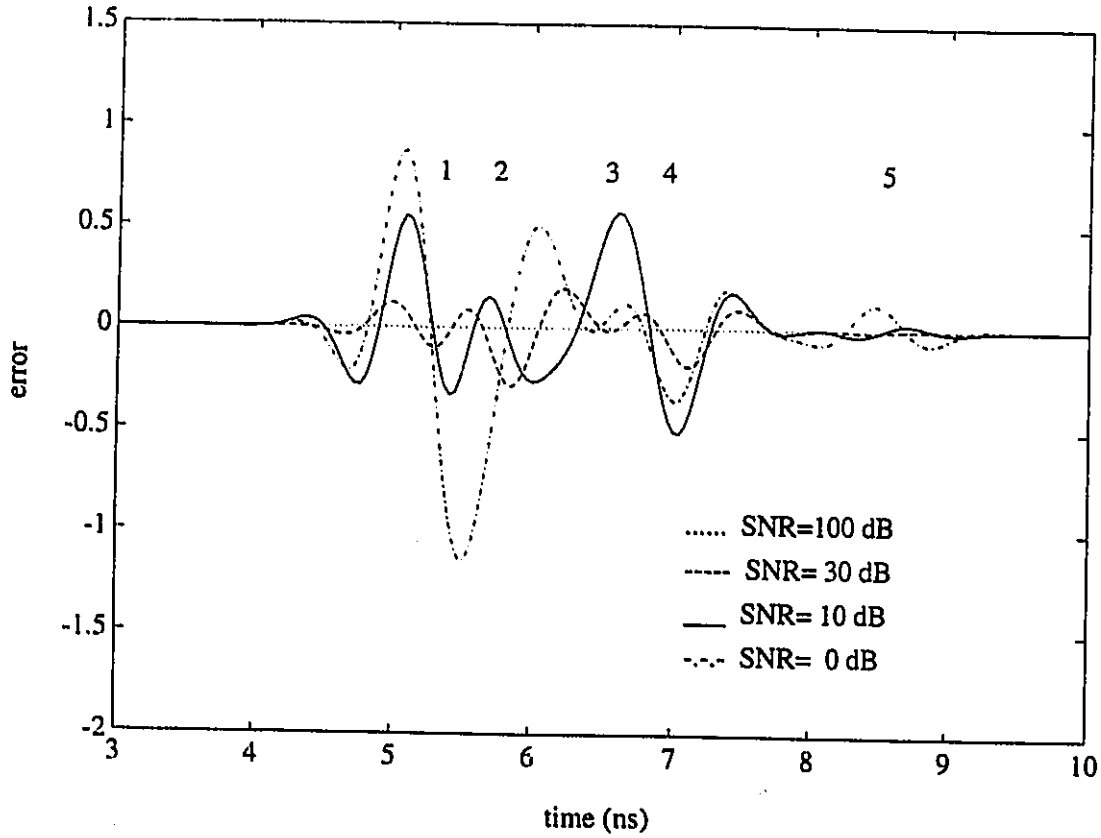

(The numbers mark the peak locations in the input.)

Figure 4.6: Error in the EBM estimated waveforms.

4.4 EB Parameter Estimation for Real Reflected Signals

In this section, we give an example of performing the eigenstructure-based method to the estimation of reflection coefficients and time delays for real reflected signal from a bridge deck. The real signal here, as depicted in Fig. 4.7, is again the same as shown in Fig. 1.3. The estimation procedure outlined in Section 4.2 is also applicable to the estimation for real signals. The number of overlapping segments M is chosen to be 20 in forming the data covariance matrix.

The resulting estimates of a_k's and t_k's are summarized in Table 4.2. Here, the value of K is again assumed to be 5 in the determination of the dimension of the noise subspace. Since the true values of the signal parameters are unknown in this case, no comparison can be made between the estimated and true values. Instead, we reconstruct the reflected waveform from the estimated parameters by using Eq.(3.22), as for the simualted signals. The waveform so obtained is illustrated in Fig. 4.7, along with the measured real data. It is observed that the eigenstructure-based method is able to locate the strong peaks in the reflected signal, but failed to locate some of the weaker peaks, just as in case of simulated signal. Comparison between Fig. 4.7 and Fig. 3.5 3.5 shows that the ML method offers a more accurate estimation of the waveform. However, this gain is achieved at the cost of large amount of computation. The eigenstructure-based method requires far less computation time.

Table 4.2: Estimated parameters of real signal.

Peak no.	1	2	3	4	5
$\hat{t}_k$	4.6994	5.2713	6.8573	8.3880	9.4170
$\hat{a}_k$	.0689	.3892	.0489	.0290	-.0019

4.5 Summary

The MUSIC algorithm represents a class of estimation techniques for the DOA problem in the array signal processing. It makes use of the eigenstructure of the signal covariance matrix to separate the

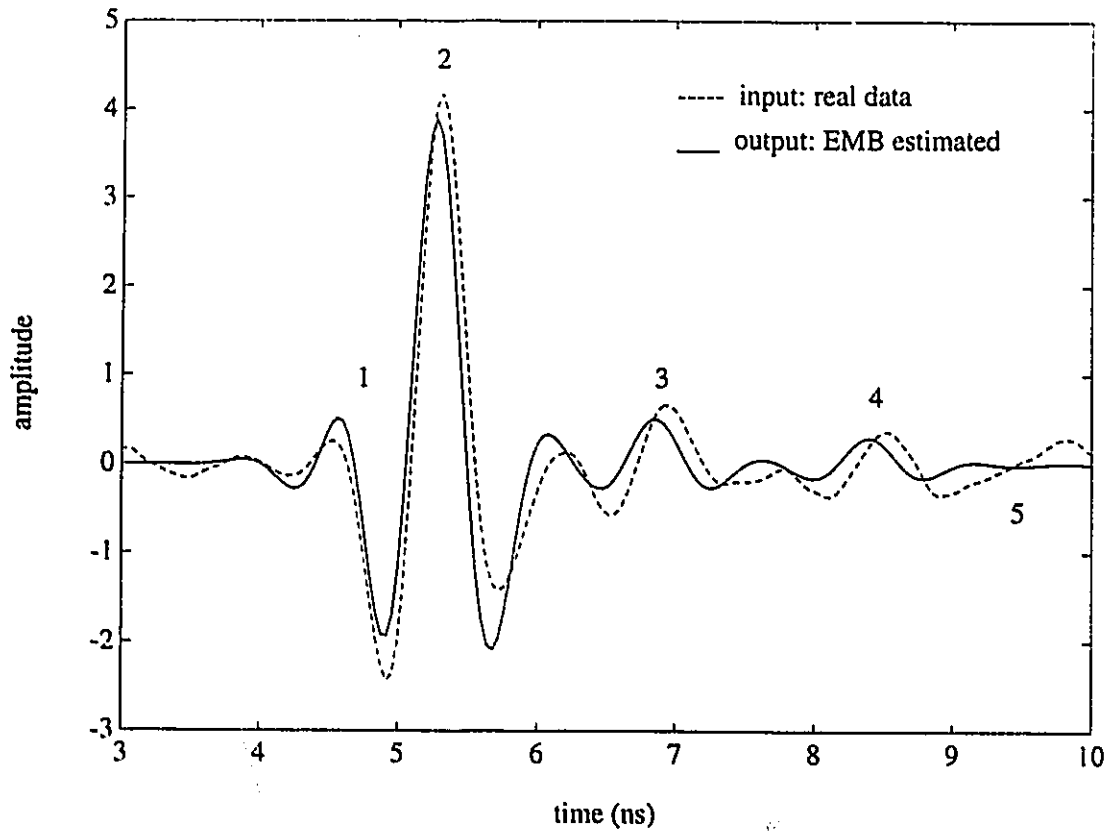

(The numbers mark the peak locations in the output.)

Figure 4.7: EB estimation of real radar waveform.

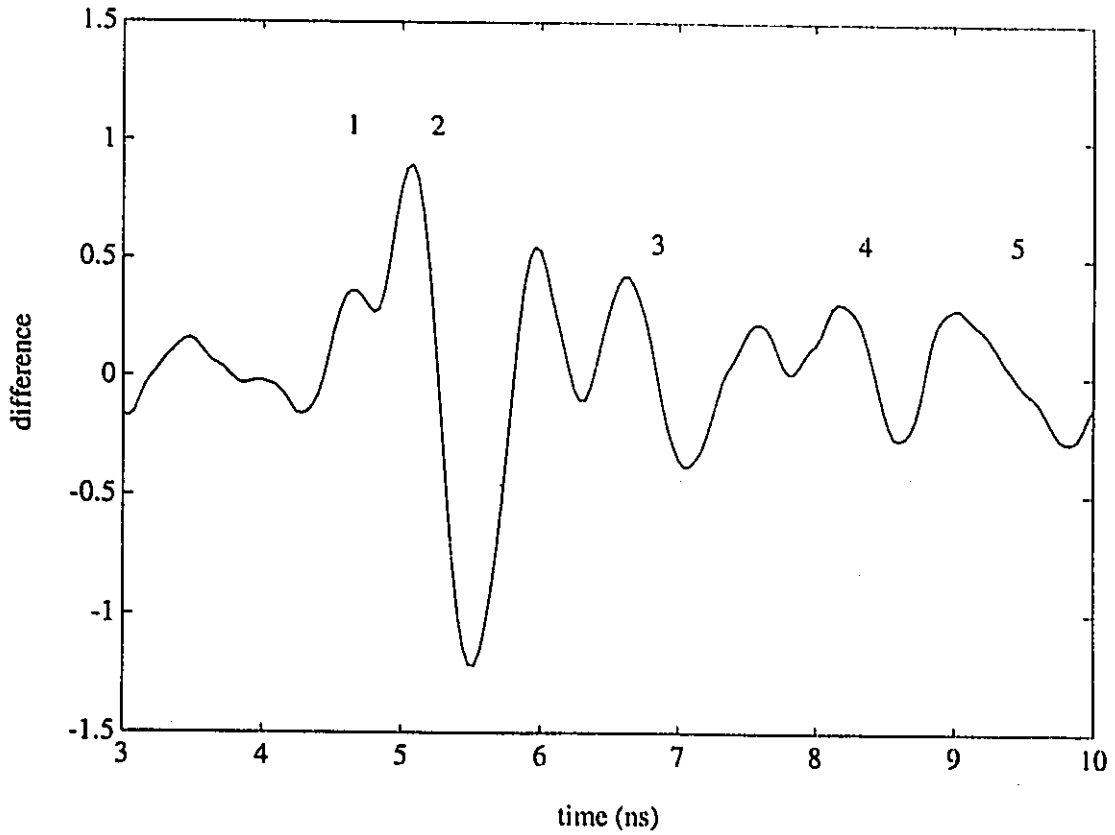

(The numbers mark the peak locations in the output.)

Figure 4.8: Difference between the real and estimated waveforms.

signal and noise subspaces. The mutual orthogonality of the signal and noise subspace provides a neat and straightforward solution to the DOA problem. In this chapter, the principle of this subspace approach based on eigen-decomposition of the covariance matrix is applied to the estimation of characteristic parameters of the reflected radar signals. It leads to the eigenstructure-based method (EBM), a new computationally efficient algorithm for the parameter estimation. In the derivation of EBM, the spectral smoothing technique is employed to overcome the rank deficiency problem in the estimation of the signal covariance matrix. The new method demands much less computation time and is not involved in the difficulty of initial value problem as encountered in the maximum mikelihood method. The method can also be used to resolve and estimate the overlapping echos in general. The error performance of the new method is comparable to that of ML estimator at high SNR level, but is inferior to that of MLE at lower SNR and deteriorates faster.

Chapter 5

Error Performance of Parameter Estimators

In any practical situation, the observations inevitably contain certain amount of noise, such as measurement error, modeling error, and ambient noise, to name a few. The presence of the random noise affects and, ultimately, limits the accuracy of the parameter estimation, which is is usually measured in terms of their mean squared errors (MSE). This chapter investigates the impact of the random noise upon the MSE of the various estimators, introduced in the previous chapters, through Monte Carlo simulations on computers. The estimators' mean squared errors are also compared with the Cramér-Rao Lower Bound (CRLB), which provides a theoretical lower limit on the minimum attainable estimation error for any unbiased estimators. A more complete analysis of the CRLB, including all the detailed mathematical derivations, can be found in Appendix A.

5.1 Cramér-Rao Lower Bounds on Estimation Errors

As addressed in Chapter 2, the reflected radar signal $y(t)$ can be modeled as a delayed sum of the probing pulse $s(t)$ such that

$$y(t) = g(t; \mathbf{a}, \mathbf{t}) + v(t)$$

$$= \sum_{k=1}^{K} a_k s(t - t_k) + v(t) \qquad t \in [0, T_r] \tag{5.1}$$

where a and t are the characteristic parameters of the media, $v(t)$ is the random noise, and $s(t)$ is given by

$$s(t) = Ae^{-\beta t^2} \cos(\omega_c t) \tag{5.2}$$

Let $\theta = (a_1, t-1, a_2, t_2, \ldots, a_K, t_K)$, or $\theta_{2k-1} = a_k$ and $\theta_{2k} = t_k$ for $k = 1, 2, \ldots, K$. Then, Eq.(5.1) may be rewritten as

$$y(t) = g(t; \theta) + v(t). \tag{5.3}$$

The following is a highlight of the results of CRLB analysis, that are obtained in Appendix A based on the delayed-sum signal model.

If the noise $v(t)$ is assumed to be a white Gaussian process with zero mean and power spectrum density (PSD) $N_0/2$, then the log-likelihood function of the parameters θ, given the observable $y(t)$, is shown to be

$$L(\theta) = \frac{2}{N_0} \int_{-\infty}^{\infty} y(t) g(t; \theta)\, dt - \frac{1}{N_0} \int_{-\infty}^{\infty} g^2(t; \theta)\, dt. \tag{5.4}$$

The associated Fisher's information matrix, $\mathbf{J}$, is defined as a $2K \times 2K$ matrix with its ijth element, J_{ij}, given by

$$J_{ij} = \mathrm{E}\left[\frac{\partial L(\theta)}{\partial \theta_i} \frac{\partial L(\theta)}{\partial \theta_j}\right], \tag{5.5}$$

or, equivalently,

$$J_{ij} = -\mathrm{E}\left[\frac{\partial^2 L(\theta)}{\partial \theta_i \partial \theta_j}\right] \qquad \text{for } i, j = 1, 2, \ldots, 2K. \tag{5.6}$$

Substitution of Eq.(5.4) into Eq.(5.6) yields

$$J_{ij} = \frac{2}{N_0} \int_{-\infty}^{\infty} \frac{\partial g(t; \theta)}{\partial \theta_i} \frac{\partial g(t; \theta)}{\partial \theta_j}\, dt \tag{5.7}$$

for $i, j = 1, 2, \ldots, 2K$. Since $J_{ij} = J_{ji}$, matrix $\mathbf{J}$ is symmetric.

Suppose that $\hat{\theta}_i$ is an unbiased estimator of θ_i. Then the variance of $\hat{\theta}_i$, denoted by $\mathrm{Var}[\hat{\theta}_i]$, is bounded below by the inequality

$$\mathrm{Var}[\hat{\theta}_i] \geq \Gamma_{ii}, \qquad \text{for } i = 1, 2 \ldots, 2K, \tag{5.8}$$

where Γ_{ii} is the ith diagonal element of matrx $\mathbf{\Gamma} = \mathbf{J}^{-1}$. The quantity given by the right-hand side of Eq.(5.8) is commonly referred to as the Cramér-Rao Lower Bound (CRLB) on the estimator $\hat{\theta}_i$,

which is the minimum attainable error for any unbiased estimator of θ_i. More specifically, Eq.(5.8) may be written in terms of a and t, namely,

$$\mathrm{Var}[\hat{a}_k] = \mathrm{Var}[\hat{\theta}_{2k-1}] \geq \Gamma_{2k-1,2k-1} \qquad \text{for } k = 1, 2, \ldots, K; \tag{5.9}$$

$$\mathrm{Var}[\hat{t}_k] = \mathrm{Var}[\hat{\theta}_{2k}] \geq \Gamma_{2k,2k} \qquad \text{for } k = 1, 2, \ldots, K. \tag{5.10}$$

5.2 Error Performance of ML Estimator

In Chapter 3, the principle of maximum likelihood estimation has been applied to determining the characteristic parameters of the reflected radar signals from multi-layered media. In this section, the error performance of the maximum likelihood estimator is to be evaluated by means of Monte Carlo computer simulations. A detailed analysis of Cramér-Rao Lower Bounds on the errors of the parameter estimation, as presented in Appendix A, indicates that the estimation errors depend largely upon the level of signal-to-noise ratio and the time distance between the radar returns in the reflected signal. Our primary goal is to assess the effects of these factors upon the performance of the ML parameter estimation. To achieve this, different reflected signals are simulated by varying the signal's parameters in Eq.(5.1), namely, the time delays t_k's and the reflection coefficients a_k's, as well as the SNR level. To be specific, the reflected signals for test consist of two returns, i.e., $K = 2$ in Eq.(5.1). The first return is always the stronger one and its arrival time t_1 and amplitude a_1 are both fixed; whereas t_2 and a_2 of the weaker, second return take various values. For the simulated signal of a particular set of parameters, the ML estimation is performed a number of times (realizations), each time with a different noise sequence being added to the signal. The mean squared errors (MSE) of the resulting estimates are then computed over all the realizations, and they are compared with each other and with the CRLB to evaluate their relative performance.

5.2.1 Performance of ML Estimation of Well Separated Arrivals

As demonstrated in Appendix A, when the reflected signal consists of only well separated returns, all the off-diagonal elements of the Fisher's information matrix J vanish, therefore J is diagonal. For K=2, its diagonal elements are given by

$$J_{2k-1,2k-1} = \frac{A^2}{N_0}\sqrt{\frac{\pi}{2\beta}}\,(1 + e^{-\omega_c^2/2\beta}), \tag{5.11}$$

and

$$J_{2k,2k} = \frac{a_k^2 A^2}{N_0}\sqrt{\frac{\pi}{2\beta}}\left\{\omega_c^2 + \beta(1 + e^{-\omega_c^2/2\beta})\right\}, \tag{5.12}$$

for $k = 1, 2$.

Since the second arrival is always the weaker return in the signal, the signal-to-noise ratio ρ is defined as

$$\rho = \rho_2 = \frac{a_2^2 A^2}{N_0}\sqrt{\frac{\pi}{2\beta}}(1 + e^{-\omega_c^2/2\beta}). \tag{5.13}$$

Then, the CRLB on the variances of estimated t_k's and a_k's can be written as

$$\mathrm{Var}[\hat{a}_k] \geq \rho^{-1} a_2^2, \tag{5.14}$$

$$\mathrm{Var}[\hat{t}_k] \geq \rho^{-1}\left(\frac{a_2}{a_k}\right)^2 \frac{1 + e^{-\omega_c^2/2\beta}}{\omega_c^2 + \beta(1 + e^{-\omega_c^2/2\beta})}, \tag{5.15}$$

for $k = 1, 2$.

In the simulation to assess the performance of ML estimator, the simulated signals consist of two returns, in which the parameters of the first return are fixed, with $t_1 = 5.0$ ns and $a_1 = 0.4$, and those of the second return varies, with $t_2 = 6.0$ or 6.5 ns and $a_2 = 0.05$ and 0.1 . For each set of parameters, the ML estimation is performed 50 times, each time with a different noise sequence, and then the mean squared errors of the estimates $\hat{t}_2$ and $\hat{a}_2$ are computed.

Figure 5.1 and 5.2 illustrate the change of MSE of the ML estimates of t_2 and a_2 with the signal-to-noise ratio, respectively, for different values of a_2. The true value of t_2 is 6.5 ns. Note that the MSE of $\hat{a}_2$ is normalized by a_2^2 in Fig. 5.2. The values of corresponding CRLB are also plotted for a comparison. As expected, the MSE's of $\hat{t}_2$ and $\hat{a}_2$ decrease as SNR increases. At high SNR, the MSE's are very close to the CRLB, which is the evidence of ML estimator being asymptotically efficient as stated in Chapter 3. Nevertheless, when the SNR is reduced to below a certain level, 6 dB in the case, the MSE's deviate significantly from the CRLB. This phenomenon is often referred to as the em threshold effect, which is due to the nonlinear nature of the ML estimator [Van Trees, 1968]. The simulation also shows that the variation of a_2 has very little effect on the estimated t_2 and a_2, just as predicted by the CRLB.

When t_2 is chosen to be 6.0 ns, the MSE's of the resulting $\hat{t}_2$ and $\hat{a}_2$ are depicted in Fig. 5.3 and Fig. 5.4, respectively. In general, they exhibit behaviour similar to that in Fig. 5.1 and 5.2, except that the threshold effect occurs slightly earlier, i.e., at higher SNR level (about 7 dB).

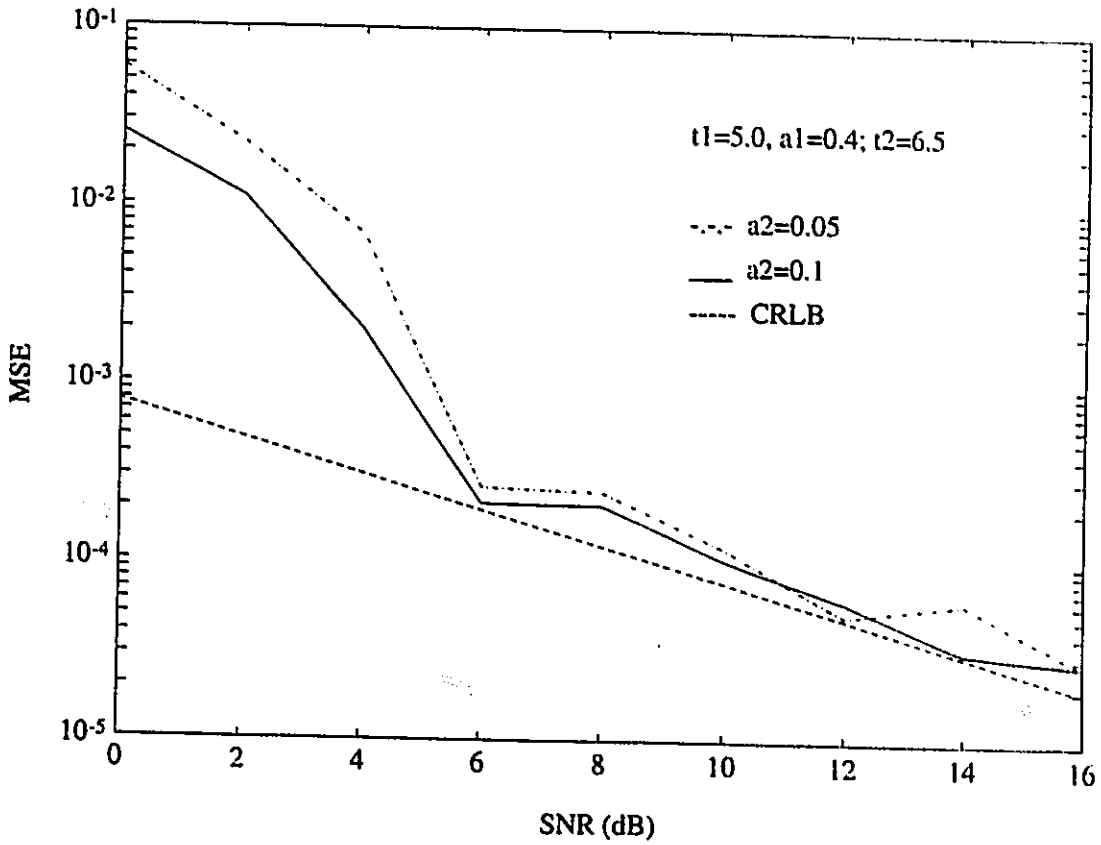

Figure 5.1: MSE of ML estimates, $\hat{t}_2$, when $t_2 = 6.5$ ns.

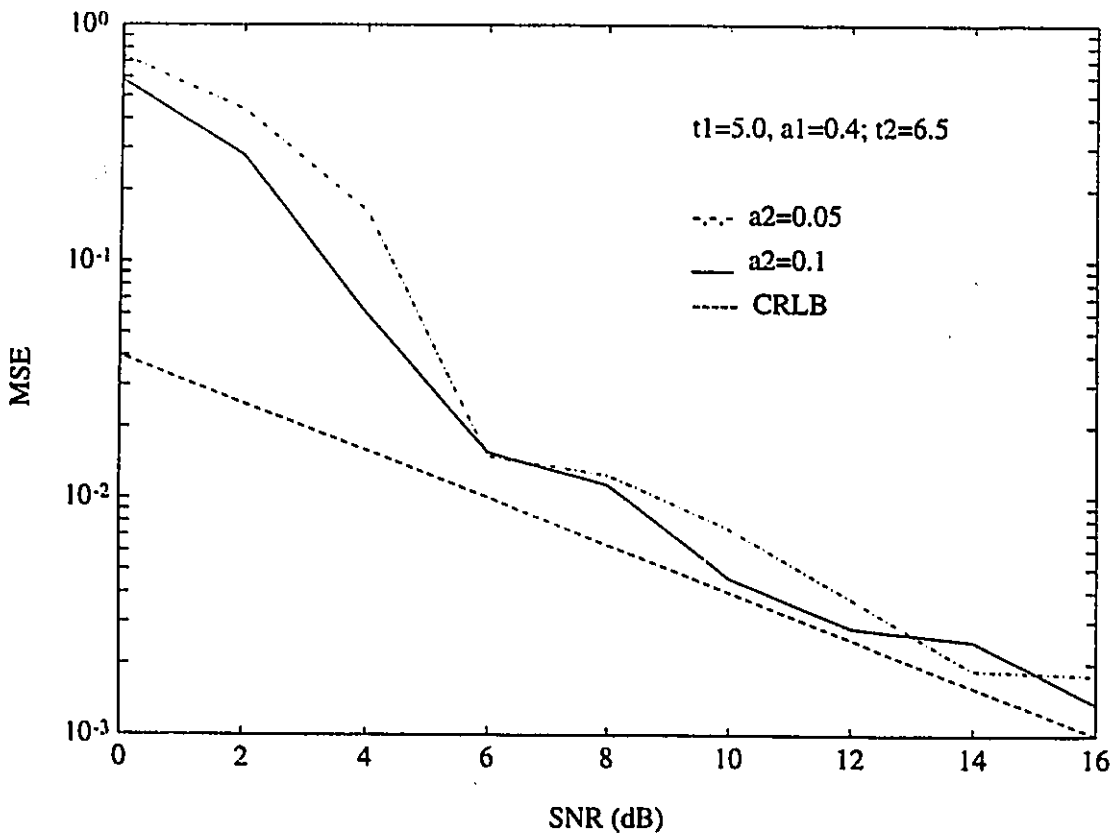

Figure 5.2: Normalized MSE of ML estimates, $\hat{a}_2$, when $t_2 = 6.5$ ns.

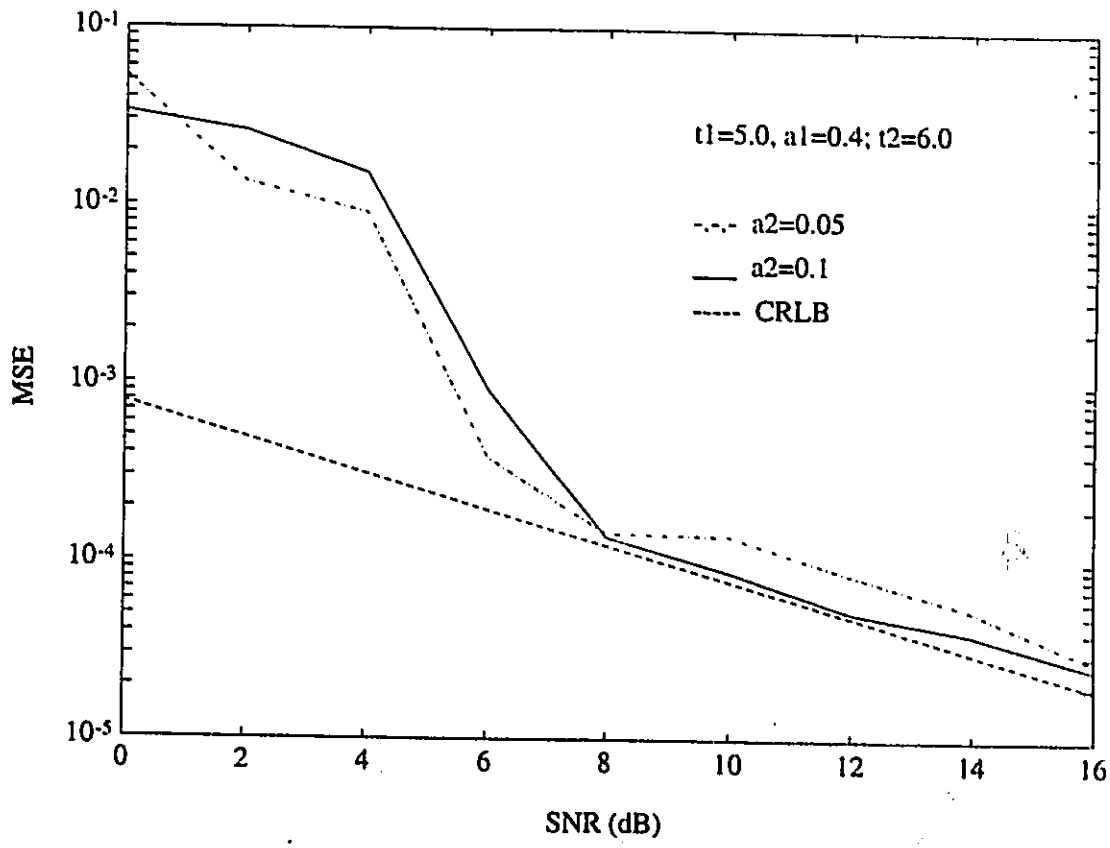

Figure 5.3: MSE of ML estimates, $\hat{t}_2$, when $t_2 = 6.0$ ns.

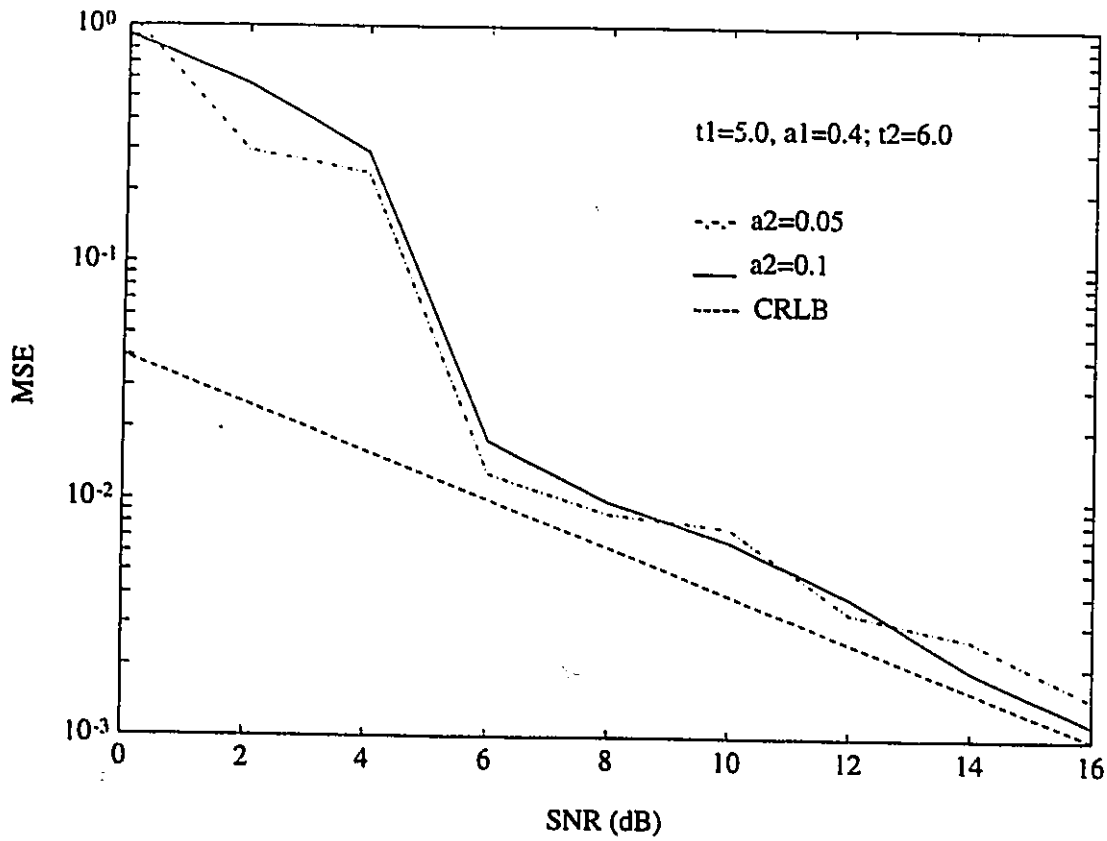

Figure 5.4: Normalized MSE of ML estimates, $\hat{a}_2$, when $t_2 = 6.0$ ns.

5.2.2 Effects of Arrival Times upon the Performance of ML Estimator

According to the analysis in Appendix A, when the difference between the arriving times of two radar returns becomes sufficiently small, the CRLB on the estimation error will increase drastically. The simulation results, as given in Fig. 5.5 and 5.6, clearly demonstrate the influence of the time distance between the two returns, $t_2 - t_1$, upon the MSE's of $\hat{t}_2$ and $\hat{a}_2$. The signal parameters for simulation are $t_1 = 5.0$ ns, $a_1 = 0.4$, $a_2 = 0.1$, and t_2 varying from 5.4 to 6.2 ns, and SNR is 10 dB. The figures show the rapid increase MSE's as the time distance $t_2 - t_1$ decreases. It is also observed that when $t_2 - t_1$ is greater than 0.8 ns, the change in MSE's with the time distance is negligible. The simulation results are in a good agreement with the prediction by CRLB analysis.

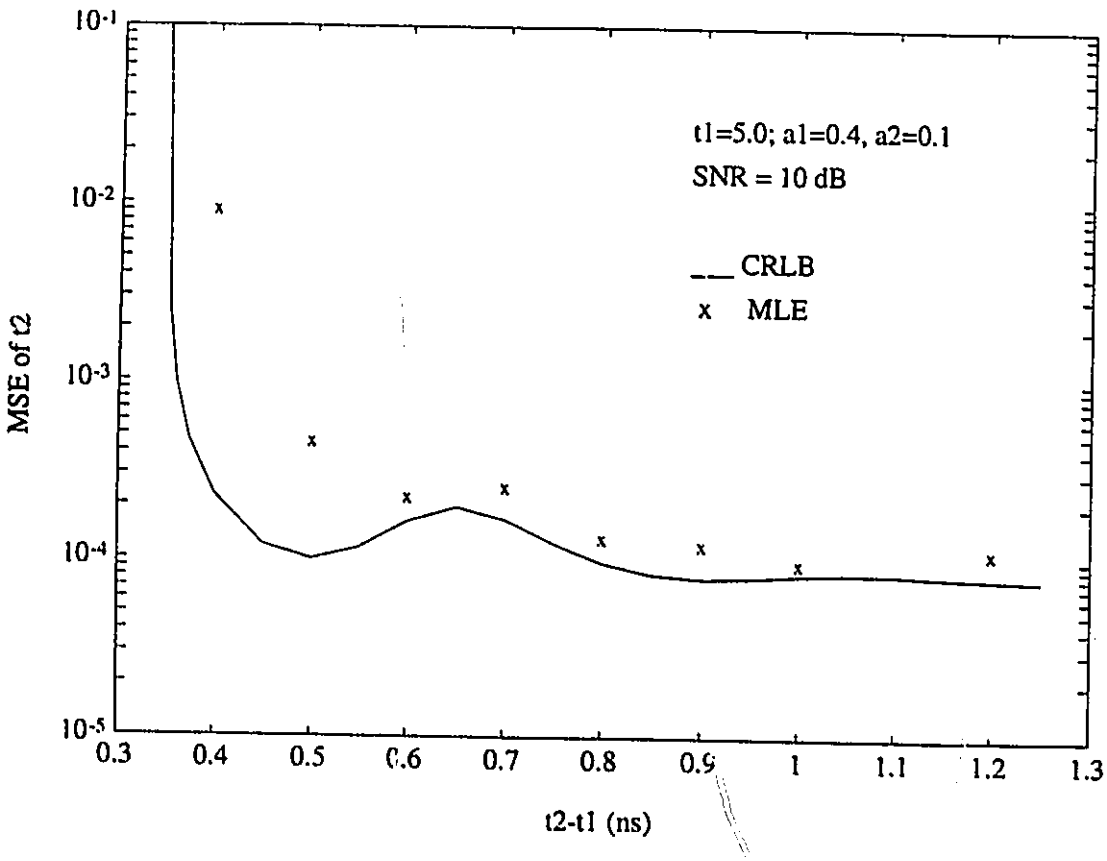

Figure 5.5: Effects of difference in time delays on MSE of $\hat{t}_2$.

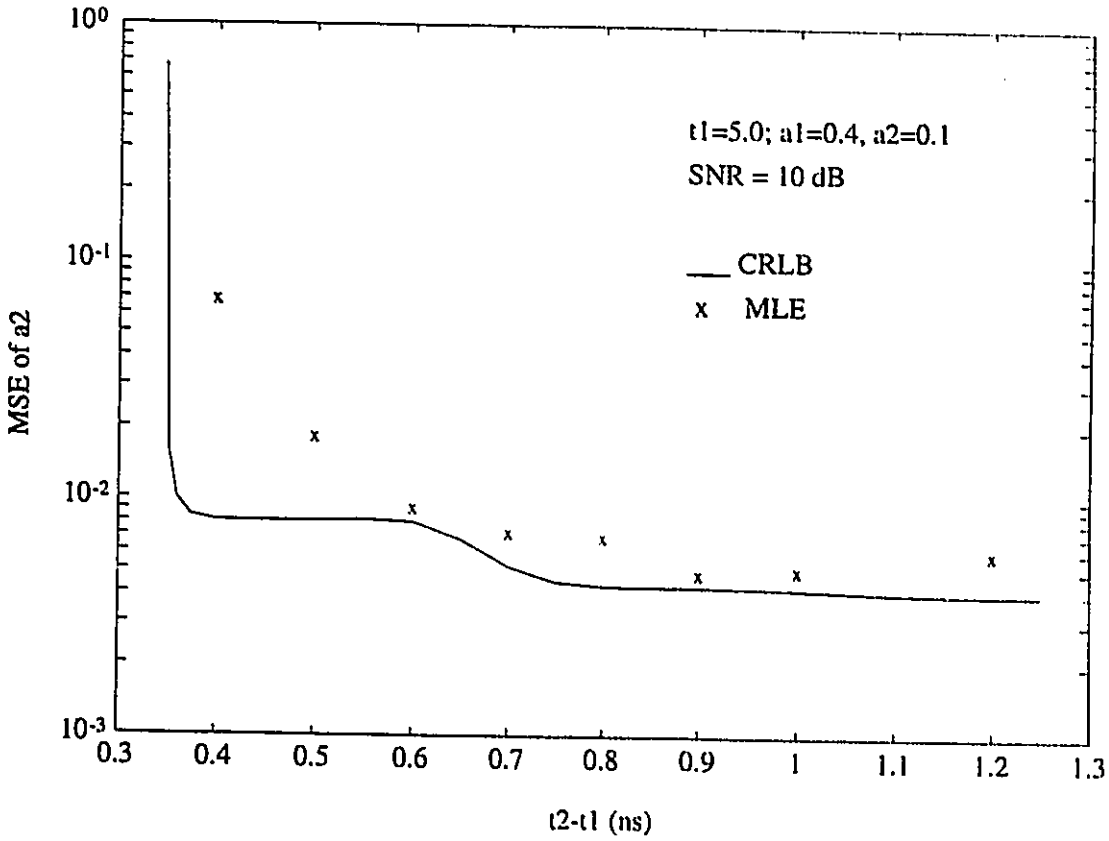

Figure 5.6: Effects of difference in time delays on MSE of $\hat{a}_2$.

5.3 Error Performance of Eigenstructure-Based Method

The Eigenstructure-Based (EB) method for parameter estimation, as derived in Chpater 4, makes use of the properties of the eigenstructure of the signal covariance matrix. It separates the space spanned by the eigenvectors of the covariance matrix into 'signal subspace' and 'noise subspace'. Since the signal component of the received data is orthogonal to the noise subspace, the estimation can be achieved by choosing the signal parameters such that they minimize the projection of the reflected signal on the noise subspace.

The evaluation of the performance of EB estimator is, again, made by estimating the parameters of simulated signals which contains two returns, or $K = 2$ in Eq.(5.1). The parameters of the first return are fixed, with $t_1 = 5.0$ ns and $a_1 = 0.4$, whereas those of the second return varies, with $t_2 = 6.0$ or 6.5 ns and $a_2 = 0.05$ and 0.1 . For the simulated signal of a particular set of parameters, the EB estimation is performed 50 times at one SNR level, each time with a different noise sequence, and then the mean squared errors of the estimates $\hat{t}_2$ and $\hat{a}_2$ are computed. The SNR level is measured with respect to the second (weaker) return. The procedure of EB estimation as illustrated in Chapter 4 is followed to determine the desired parameters, where the Fourier transformed sequence is partitioned into $M = 20$ segments for computing the covariance matrix.

For $t_2 = 6.5$, the resulting MSE's of $\hat{t}_2$ and $\hat{a}_2$ for various values of a_2 are plotted against SNR level in Fig. 5.7 and 5.8, respectively. The MSE of $\hat{a}_2$ is normalized by a_2^2. The corresponding CRLB's are also given as references. Undoubtedly, the MSE's of the estimates rise as the SNR decreases, and moreover, when the SNR becomes lower than about 4 dB, the MSE's increase rate takes a remarkable jump. Therefore, there is also a threshold effect in the EB estimation. However, at high level of SNR, the MSE's don't approach the CRLB's as in the case of ML estimation. In both figures, the influence of varying a_2 is negligible, as indicated by the CRLB analysis.

When $t_2 = 6.0$ ns, the MSE's of the resulting $\hat{t}_2$ and $\hat{a}_2$ from simulations are illustrated in Fig. 5.9 and Fig. 5.10, respectively. Similar observations can be made as for Fig. 5.7 and 5.8.

Comparisons between the ML and EB estimation errors are presented in Fig. 5.11 and Fig. 5.12. Compared with the ML estimation, the threshold effect of EB estimation occurs later, i.e., at lower SNR level, than ML method. However, the MSE of the EB estimation is generally much greater than that of ML estimation, and stays far above the CRLB even at high SNR levels.

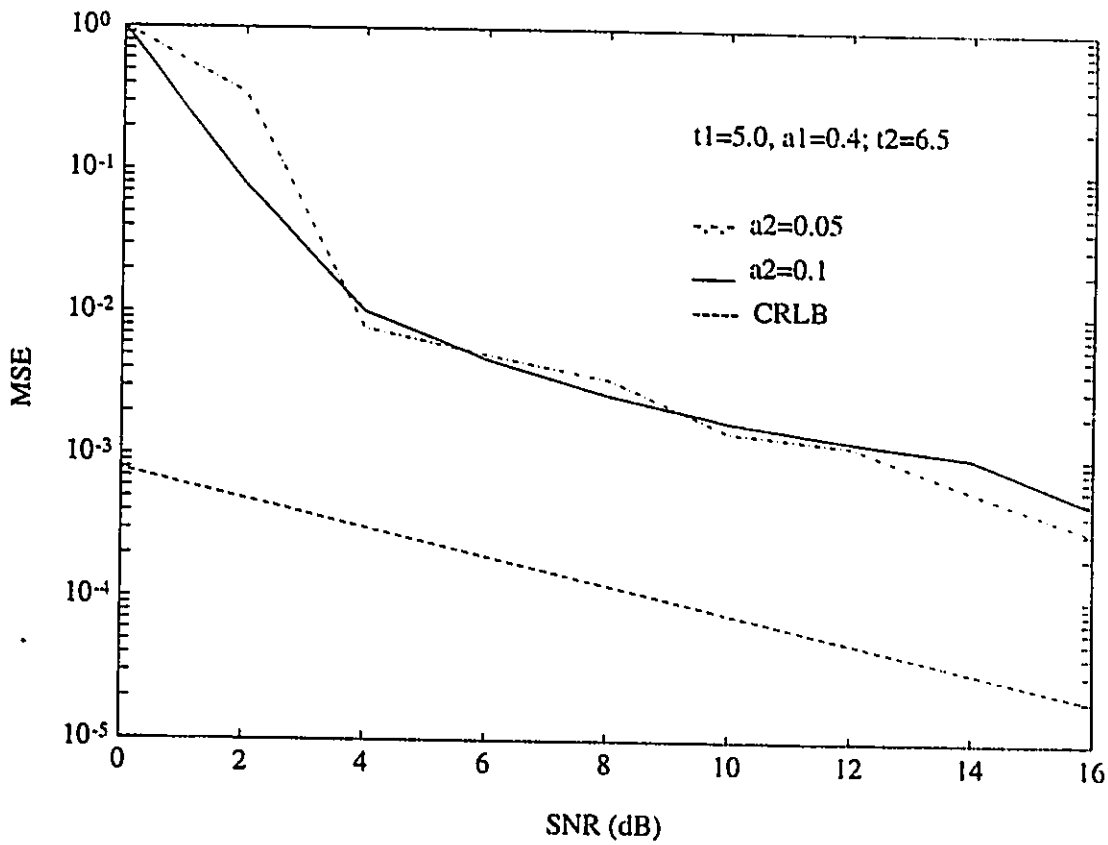

Figure 5.7: MSE of EB estimates, $\hat{t}_2$, when $t_2 = 6.5$ ns.

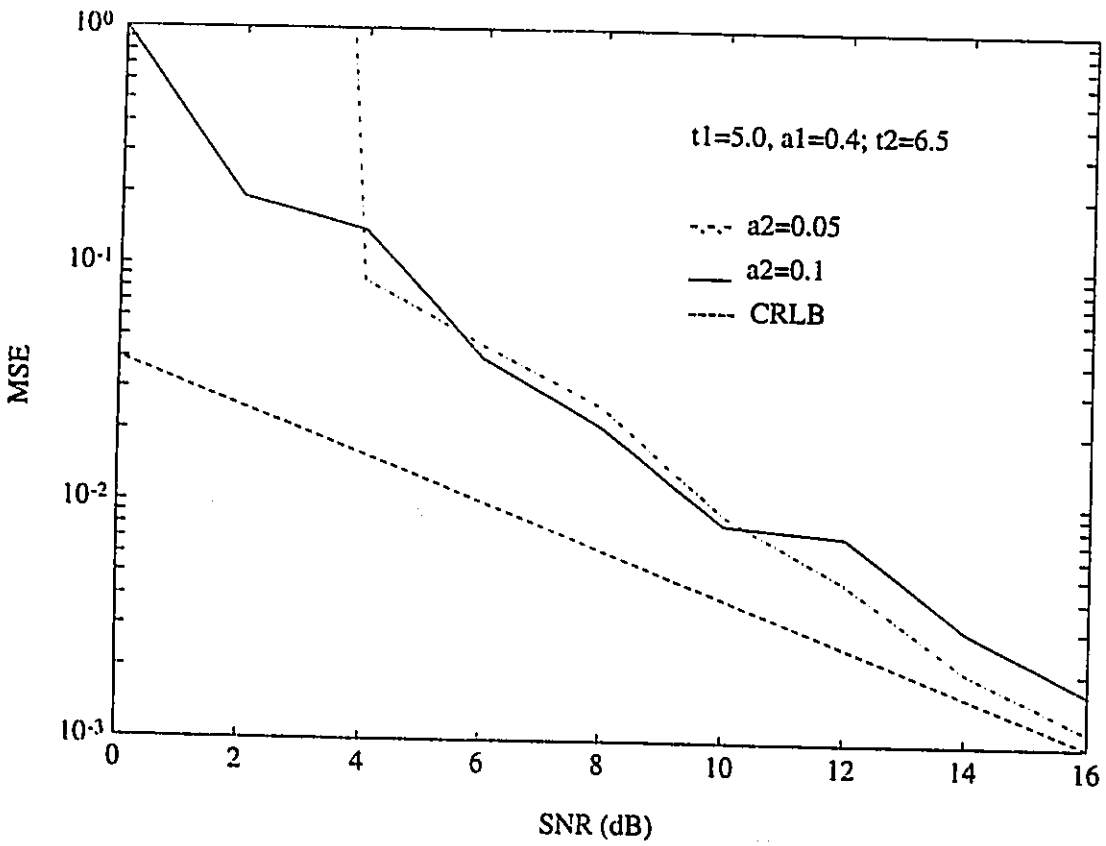

Figure 5.8: MSE of EB estimates, $\hat{a}_2$, when $t_2 = 6.5$ ns.

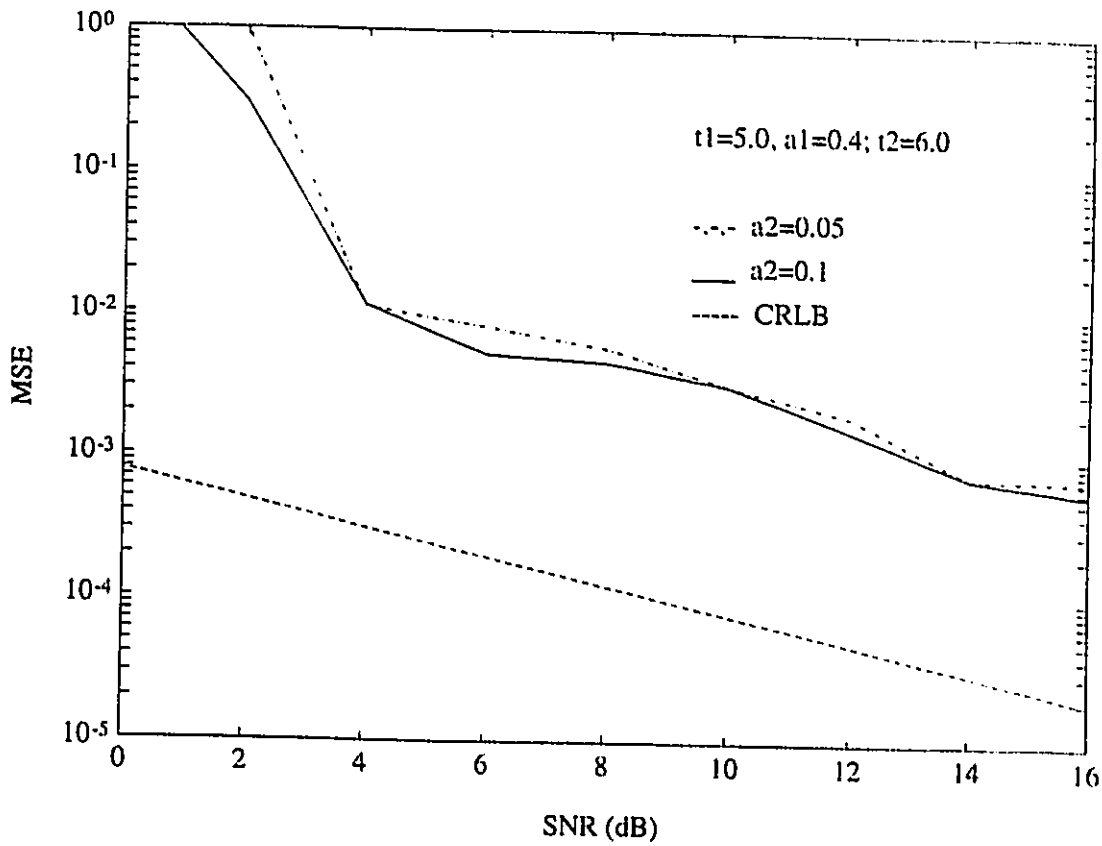

Figure 5.9: MSE of EB estimates, $\hat{t}_2$, when $t_2 = 6.0$ ns.

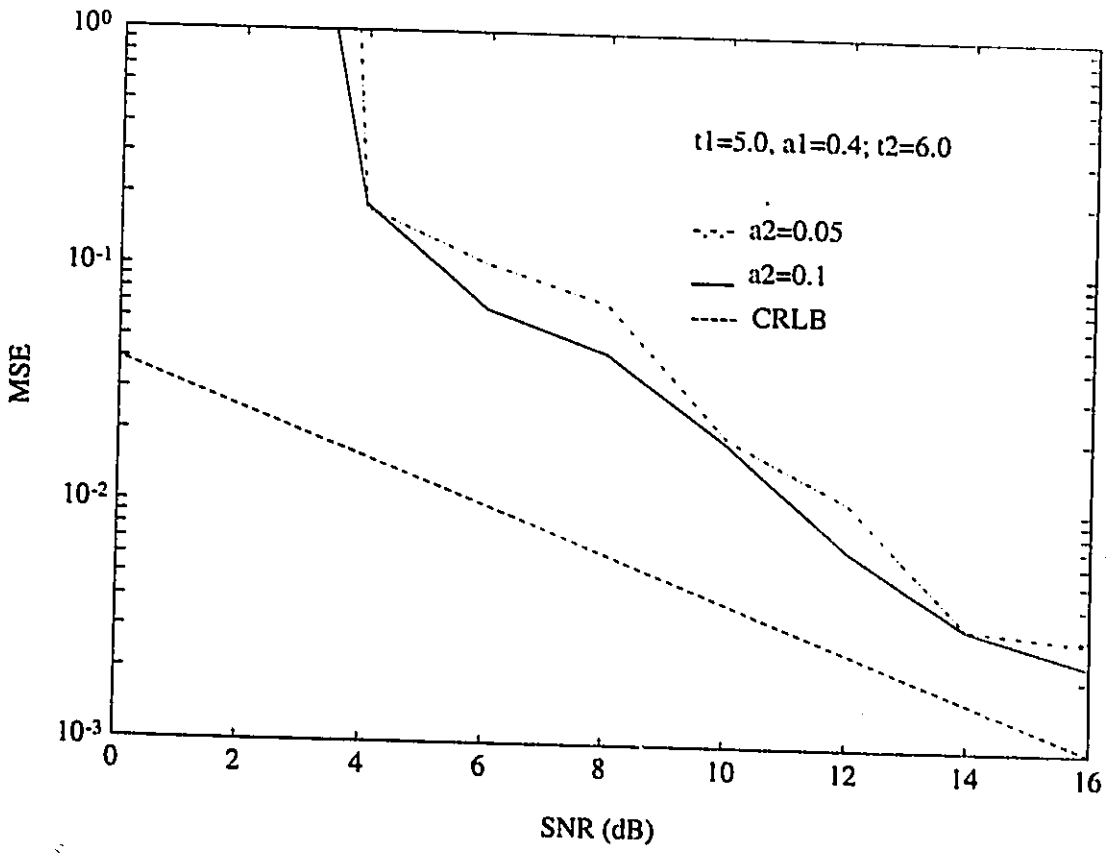

Figure 5.10: MSE of EB estimates, $\hat{a}_2$, when $t_2 = 6.0$ ns.

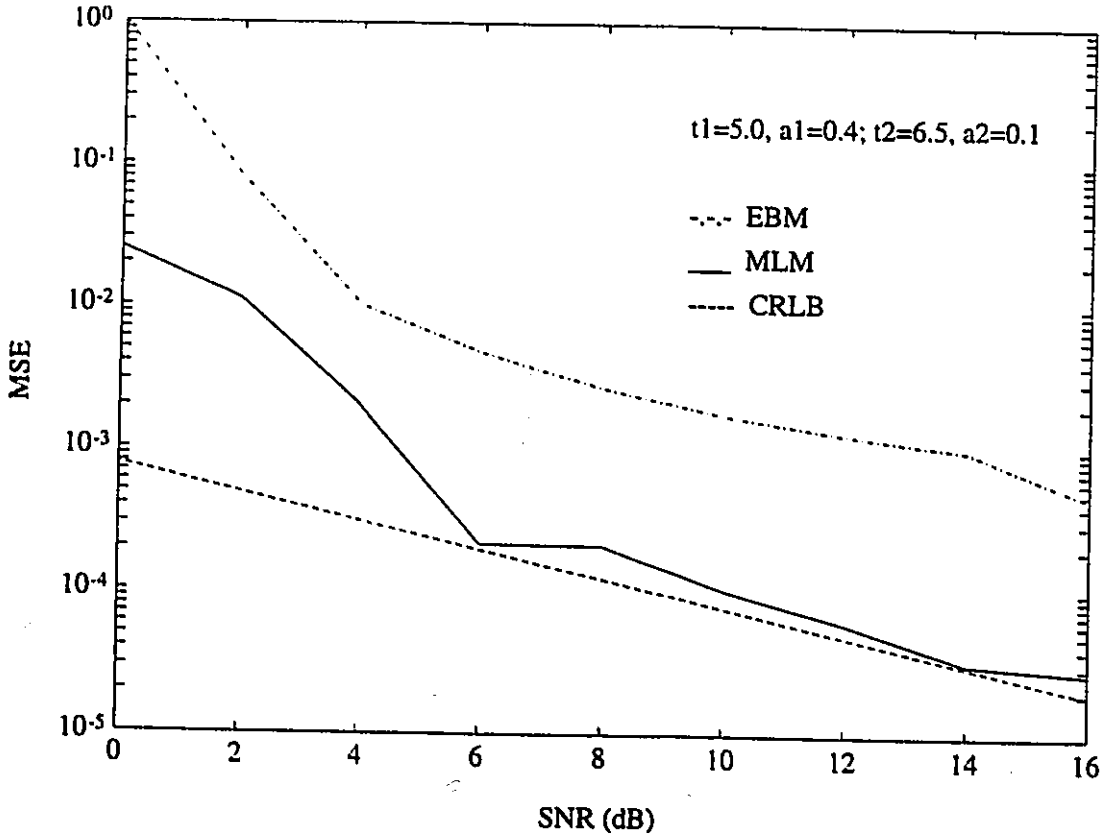

Figure 5.11: Performance comparison between ML and EB estimators of t_2.

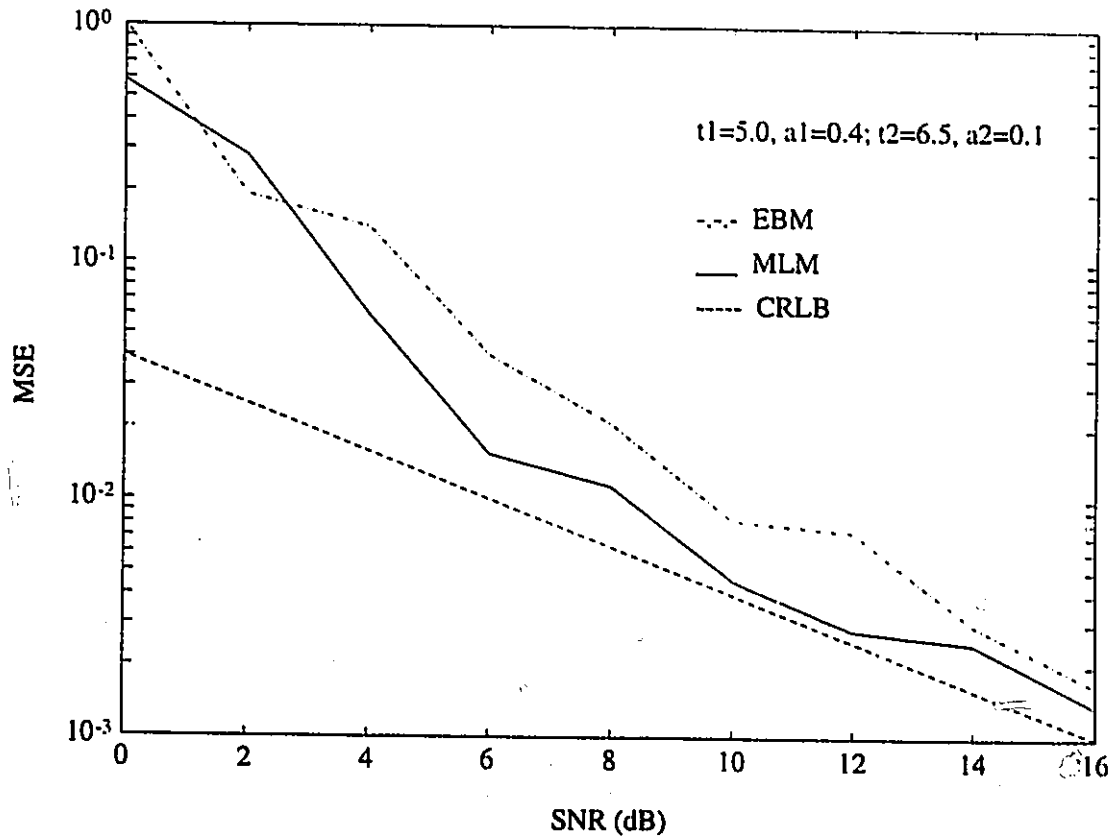

Figure 5.12: Performance comparison between ML and EB estimators of a_2.

5.4 Summary

In this chapter, the error performances of ML and EB estimators are evaluated by means of computer simulations and by the analysis of the limiting behaviour of the estimators, namely, the Cramér-Rao Lower Bound. It is observed in the simulations that at high SNR levels, the maximum likelihood method provides a very accurate estimation of the signal parameters and the mean squared errors of the estimates approach the Cramér-Rao Lower Bounds with the increase of SNR. At lower SNR levels, however, its performance deteriorates faster than what is predicted by CRLB, due to the nonlinear nature of the ML method. The Eigenstructure-Based method is very efficient in computation and yields satisfactory estimates of the parameters at high SNR levels. However, it does poorly at lower SNR levels, and its performance is in general inferior to that of the ML method. The CRLB analysis shows that the estimation will fail when the separation between two returns in a reflected signal is less than about 30 percent of the radar pulse width. This prediction is verified by the computer simulation.

Chapter 6

Predictive Deconvolution of Reflected Radar Signals

6.1 Introduction

For the purpose of radar probing, the bridge decks are modelled as a system of lossless, stratified media with each layer being homogeneous and isotropic (see Chapter 2). The reflected radar signals from this multi-layered media system can be then represented by a delay-sum model which is completely described by a set of characteristic parameters, namely, the reflection coefficients, r_k's, and the travel time for electromagnetic wave in the layers, τ_k's. Based upon such a parametric model, the maximum likelihood method and the eigenstructure-based method are developed, in Chapter 3 and Chapter 4, respectively, to estimate these parameters as to determine the subsurface conditions of the bridge decks under investigation. However, the use of parametric estimation techniques is by no means the only approach to extracting the subsurface features. One alternative is to utilize the deconvolution techniques, which are based on a nonparametric, convolutional representation of the reflected signals from the multi-layered media.

Problems of data processing similar to those associated with ground probing radar have been also encountered in geophysical exploration by means of *reflection seismology*. In the seismic exploration,

a pulse-like seismic energy waveform is emitted as a probing signal into the earth and reflected waves are transmitted back to the surface where they are recorded by pressure or velocity sensitive detectors. Various data processing operations are then performed on the observed data to extract the relevant information of the structure of the geological medium through which the seismic waves travel. An appropriate interpretation of the results will help to locate the potential oil and natural gas deposit that are trapped deep within the sedimentary layers of the earth's crust [Silvia, 1979]. In the reflection seismology, a layered earth model is often assumed, and both input signal to and output from the earth are measured, thus known. The goal is to deduce from them the structure of the geological strata. This procedure is generally referred to as *seismic inversion*, or *seismic deconvolution* in particular when a convolutional model is employed for the strata. Of various methods of seismic inversion, *Predictive deconvolution* provides a simple yet practical solution to the inversion problem based on a statistical approach, and has been a very popular and successful deconvolution technique in geophysical explorations for many years since Robinson's pioneering work in the 1950's [Robinson, 1954,1957; Wadsworth, 1953]. In principle, it is a direct application of Wiener filtering theory to the inverse problem in the reflection seismology [Robinson, 1984a; Arya, 1978; Mendel, 1980].

Due to the similarities between the problems in reflection seismology and those in impulse radar probing of the bridge decks, the methods of the seismic deconvolution are potentially applicable to the data processing of reflected radar signals [Daniels, 1988; McCann, 1988].

The primary objectives of this chapter are, firstly, to derive and apply the predictive deconvolution method to the reflected impulse radar signals so as to retrieve the desired information about the bridge decks such as the thickness of each layer and reflection coefficients; and secondly, to assess the performance of the predictive deconvolution under various conditions.

In this chapter the convolutional model for the reflected radar signals is introduced, and basic assumptions on the nature of layered media's reflectivity are addressed. The derivation of various implementations of the predictive deconvolution are presented. Examples of both simulated and real signals are also given to evaluate the feasibility of this method.

6.2 Convolutional Model for Reflected Radar Signals

As discussed in Chapter 2, a bridge deck has a structure of multi-layered media, consisting of asphalt, membrane, concrete, and reinforcing steel bars. For analytic simplicity, the bridge deck is treated as

lossless, non-dispersive, horizontally layered media with each layer being homogeneous and isotropic. Furthermore, the probing radar signal is assumed to be of normal incidence to the surface of the bridge deck and has a plane wavefront. The measured waveform of the probing radar signal $s(t)$ is illustrated in Fig. 1.2, and can be closely approximated by a modulated Gaussian function given by

$$s(t) = A\exp(-\beta t^2)\cos(2\pi f_c t), \tag{6.1}$$

where the constants A, β, f_c are all presented in Table 2.1.

Suppose that the impulse response of the multi-layered media system under radar probing is $u(t)$. Then, the reflected signal, $y(t)$, may be viewed as the output of the media system excited by input $s(t)$, and written as a convolution of $u(t)$ with $s(t)$ [Mendel, 1983] such that

$$y(t) = \int_0^t u(\tau)s(t-\tau)\,d\tau + v(t) \qquad t \in (0, T_r), \tag{6.2}$$

where $v(t)$ denotes the random noise, and the observation interval, T_r, is usually taken to be much longer than the duration of the probing radar signal $s(t)$. By system theory, Eq.(6.2) implies that the bridge deck under our assumptions is a linear, time-invariant, and causal system [Chen, 1970; Kailath, 1980]. By appropriate discretization methods, the convolution in Eq.(6.2) can be rewritten in a convolution sum,

$$y(nT) = \sum_{i=0}^{n} u(iT)s(nT - iT) + v(nT); \tag{6.3}$$

or, more conveniently,

$$y(n) = \sum_{i=0}^{n} u(i)s(n-i) + v(n), \qquad \text{for } n = 0, 1, 2, \ldots, N, \tag{6.4}$$

where T denotes the sampling period, which is 0.04 ns in our measurements. The sequence $\{u(n), n = 0, 1, \ldots, N\}$ is the unit response of the media system, a discrete equivalence of impulse response. This nonparametric model for the reflected signals is the starting point for all deconvolution procedures.

In Eq.(6.4), the reflected signal $\{y(n)\}$ is essentially the time-delayed, scaled replicas of the incident signal $\{s(n)\}$, with the unit response, $u(n)$'s, being the scaling factors, equally spaced at time instances $t = nT$. Since the impulse response bears inherently the reflection characteristics of the media, $u(n)$'s are related to the reflection coefficients r_k's, and often referred to as *reflectivity sequence* in the literature of seismic deconvolutions. It should be noted, however, that in general $u(k) \neq r_k$ and $u(k) \neq a_k$ in Eq.(2.23). A comparison of Eq.(6.4) with Eq.(2.23) reveals that not all of $u(n)$'s are associated with the physical reflecting interfaces in the layered media as shown in Fig. 2.1. In fact, the total number of samples in the sequence $\{u(n)\}$ in practice is much larger than

the number of layers in the real bridge deck. Consequently, each physical layer will contain a number of artificial interfaces separated by an equal two-way travel time interval T. The total number of these artificial interfaces in the kth layer is $n_k = 2\tau_k/T$, where τ_k is the one-way travel time in the kth layer. This is not really a loss in generality, since setting the corresponding $u(n)$'s to zero will effectively remove any artificial boundaries from the model [Robinson, 1984a]. For convenience, $u(n)$'s are sometimes also referred to as reflection coefficients, and the non-zero samples of $u(n)$'s are indeed very close to the reflection coefficients for a plane wave incidence and r_k's being sufficiently small ($|r_k| \ll 1$) [Robinson, 1984a; Justice, 1985].

6.3 Derivation of Predictive Deconvolution

6.3.1 Preliminaries and Assumptions of Deconvolution

If the reflected radar signals are represented by the convolutional model as described above in Eq.(6.4), then, the deconvolution can be considered, in general, as a procedure which undoes the operation of convolution. In other words, it removes the effects of the convolutional factor (*i.e.*, the probing signal $\{s(n)\}$) from the observed signal $\{y(n)\}$, thus retrieves the desired reflectivity sequence $\{u(n)\}$, or at least an estimate thereof. Consequently, the true reflection coefficients r_k's and the one-way travel time τ_k can be approximated by eliminating those zero-valued samples of $u(n)$'s that correspond to the artificial boundaries.

Signal and System

In the practice of deconvolution, a filtering operation is performed on the observed data samples $\{y(n)\}$ to produce an estimate of the reflectivity sequence $\{u(n)\}$. The filter for this purpose is referred to as an *inverse filter*, and is often chosen to be linear and time-invariant. Let $\{f(n)\}$ be the unit response of the inverse filter. Then, its output is

$$\hat{u}(n) = f(n) * y(n), \tag{6.5}$$

where $*$ denotes the operation of convolution. Since convolution is *commutative*,

$$\begin{aligned} y(n) &= u(n) * s(n) + v(n) \\ &= \sum_{i=0}^{n} u(i)s(n-i) + v(n) = \sum_{i=0}^{n} s(i)u(n-i) + v(n), \end{aligned} \tag{6.6}$$

then, a deconvolution scheme can be described by Fig. 6.1.

It is noted that, in Fig. 6.1, $\{s(n)\}$ is treated as a 'system response' and the reflectivity sequence $\{u(n)\}$ as the input to this 'system' or the desired output from the inverse filer, following a common practice in seismic deconvolution [Robinson, 1984b; Mendel, 1983]. Although this interpretation is rather counterintuitive from a physical point of view, there are two good reasons for doing so. Firstly, since the model in Eq.(6.4) is associated with a linear dynamical system, undoubtedly, it is mathematically more efficient and computationally more economical for such a system to be of lower dimensionality, as is the case when $s(n)$ is assumed to be its unit response, than a system of very high dimensionality, as would be the case if $u(n)$ is taken as its unit response. Additionally, owing to the hypothesis that the reflectivity sequence is random (which will be discussed in detail below), it is natural and more convenient to treat it as the system input [Mendel 1983].

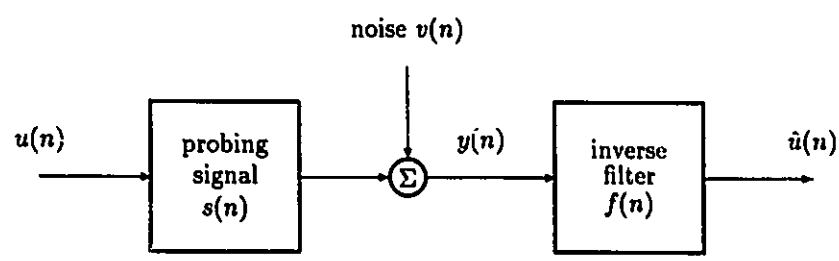

Figure 6.1: Schematic diagram of a convolution-deconvolution system.

Inverse Filter

The primary motivation for performing deconvolution is to improve the resolution of closely spaced returns of probing signal $\{s(n)\}$ in the reflected signal $\{y(n)\}$. From the convolution model Eq.(6.6)

and the filter definition Eq.(6.10), the output after inverse filtering is

$$\hat{u}(n) = \sum_{m=0}^{n} g(m)u(n-m) + \sum_{m=0}^{n} f(m)v(n-m), \tag{6.7}$$

where

$$g(n) = \sum_{m=0}^{n} f(m)s(n-m), \tag{6.8}$$

is the 'total response' of combined convolution-deconvolution system. To resolve closely spaced returns, $g(n)$ must be of relatively short duration. In the ideal situation, when $g(n) = \delta(k)$,

$$\hat{u}(n) = u(n) + \sum_{m=0}^{n} f(m)v(n-m). \tag{6.9}$$

Despite the fact that the probing signal $\{s(n)\}$, hence its z-transform, $S(z) = \mathcal{Z}\{s(n)\}$, is known in our problem, the transfer function of the inverse filter, $F(z) = \mathcal{Z}\{f(n)\}$, can not be taken simply as the reciprocal of $S(z)$, $F(z) = 1/S(z)$. That is because $\{s(n)\}$ is not necessarily of minimum phase, thus the zeros of $S(z)$, or the poles of $F(z)$, may lie outside of the unit circle in z-plane, which will result in an unstable system. Another deficiency of such an inverse filter is that it does not take into account the effects of random noise upon the deconvolution. Because the measured reflected signals inevitably contain some noise, the lack of noise suppression capability makes it highly inappropriate to be used in practical deconvolution. A solution to overcoming these difficulties is the utilization of predictive deconvolution techniques, which takes a more robust statistical approach to the problem, and is a widely accepted method in seismic deconvolution.

Random Reflectivity Hypothesis

As addressed earlier, the reflectivity sequence $\{u(n)\}$ is characterized by the fact that most of its samples are zero, with only a few non-zero elements distributed sparsely among them. The exact values of these non-zero samples are, however, unpredictable, and the positions where they appear are totally unrelated to each other. Therefore, if the observed time series of the reflected signal is assumed from a stationary stochastic process, then, the predictive part of the time series is attributed to the probing signal, $\{s(n)\}$, whereas the layered system's reflectivity, $\{u(n)\}$, is completely unpredictable. The spectrum of such a sequence is close to be flat, *i.e.*, white. This line of reasoning leads to a basic hypothesis in predictive deconvolution. It states that the reflectivity sequence $\{u(n)\}$ is a sample function from a white (but not necessarily Gaussian) random process with zero-mean and variance σ_u^2, and it is statistically independent of the noise sequence $\{v(n)\}$. This

random reflectivity hypothesis is commonly made in the derivation of most of seismic deconvolution algorithms [Mendel, 1983].

Although the geophysics community is divided on the issue of the use of random or deterministic earth models [Fokkema, 1987; Walden, 1987], there are strong arguments that the random models may be more robust than deterministic physical models when *a priori* knowledge of the layered media system is insufficient, and/or when the measurement noise is present in the data [Robinson, 1980; Mendel, 1986]. Geophysical experience over three decades has shown that the randomness hypothesis is indeed satisfied in many quantitative tests [Walden, 1985]. As a result, predictive deconvolution is robust under a wide variety of input conditions, and is routinely used in seismic data processing for geophysical exploration [Robinson, 1984b; Jurkevics, 1984].

6.3.2 Wiener Filtering as Predictive Deconvolution

In deconvolution, the inverse filter is usually chosen from the class of linear, time-invariant type filters. Suppose that the inverse filter is, in addition, a *finite-duration impulse response* (FIR) system of order M, whose coefficients are given by $f(n), n = 0, 1, \ldots, M-1$. Then, Eq.(6.5) may be rewritten as

$$\hat{u}(n) = f(n) * y(n) = \sum_{m=0}^{M-1} f(m)y(n-m), \qquad \text{for } M-1 \leq n \leq N. \tag{6.10}$$

Since the output $\{\hat{u}(n)\}$ should provide an estimate of the true reflectivity sequence $\{u(n)\}$ for the given input samples $\{y(n)\}$, the filter design must satisfy certain optimal criterion. In predictive deconvolution, the mean-square value of the estimation error, defined as the difference between the actual output $\{\hat{u}(n)\}$ and the desired output $\{u(n)\}$, is minimized. Such a linear, minimum mean-squared error (MSE) filter, in fact, belongs to a class of optimal filters, collectively known as Wiener filters [Haykin, 1991].

Mean-Squared Error of Estimation

From Eq.(6.6), the estimation error, denoted by $e(n)$, may be written as

$$\begin{aligned} e(n) &= \hat{u}(n) - u(n) \\ &= \sum_{m=0}^{M-1} f(m)y(n-m) - u(n), \end{aligned} \tag{6.11}$$

and the mean-squared error $\mathcal{E}$ is

$$\begin{aligned}
\mathcal{E} &= \mathrm{E}\{e^2(n)\} \\
&= \mathrm{E}\left\{\left[\sum_{m=0}^{M-1} f(m)y(n-m) - u(n)\right]^2\right\} \\
&= \mathrm{E}[u^2(n)] - 2\sum_{m=0}^{M-1} f(m)\mathrm{E}[y(n-m)u(n)] \\
&\quad + \sum_{m=0}^{M-1}\sum_{k=0}^{M-1} f(m)f(k)\mathrm{E}[y(n-m)y(n-k)]. \qquad (6.12)
\end{aligned}$$

The quantity $\mathcal{E}$ does not depend on the time index n due to the stationarity assumption on $u(n)$ and $v(n)$. Note that the auto-correlation function of real sequence $\{y(n)\}$ is defined as

$$r_{yy}(k) = r_{yy}(-k) = \mathrm{E}[y(n)y(n-k)], \qquad (6.13)$$

and the cross-correlation between $\{u(n)\}$ and $\{y(n)\}$ as

$$r_{uy}(k) = \mathrm{E}[u(n)y(n-k)]. \qquad (6.14)$$

Therefore, Eq.(6.12) can be rewritten as

$$\mathcal{E} = \sigma_u^2 - 2\sum_{m=0}^{M-1} f(m)r_{uy}(m) + \sum_{m=0}^{M-1}\sum_{k=0}^{M-1} f(m)f(k)r_{yy}(k-m), \qquad (6.15)$$

where $\sigma_u^2 = \mathrm{E}[u^2(n)]$.

Derivation of Normal Equations

To minimize MSE of the estimation, we take the partial derivatives of $\mathcal{E}$ with respect to all the unknown filter coefficients, $f(n)$'s, and then set them to be zero:

$$\frac{\partial \mathcal{E}}{\partial f(n)} = 0, \qquad \text{for } n = 0, 1, \ldots, M-1. \qquad (6.16)$$

This leads to a system of M simultaneous linear equations of the M unknowns $f(0), f(1), \ldots,$ $f(M-1)$, namely,

$$\sum_{m=0}^{M-1} f(m)r_{yy}(k-m) = r_{uy}(k), \qquad k = 0, 1, \ldots, M-1. \qquad (6.17)$$

These equations are called Wiener-Hoff normal equations, which define the optimal filter in terms of auto-correlation and cross-correlation functions. Alternatively, Eq.(6.17) may be expressed in a matrix notation,

$$\mathbf{R}_{yy}\mathbf{f} = \mathbf{r}_{uy}, \tag{6.18}$$

where $\mathbf{f}$ and $\mathbf{r}_{uy}$ are $M \times 1$ vectors, defined as

$$\begin{aligned} \mathbf{f} &= [f(0), \ldots, f(M-1)]^T, \\ \mathbf{r}_{uy} &= [r_{uy}(0), r_{uy}(1), \ldots, r_{uy}(M-1)]^T, \end{aligned}$$

and $\mathbf{R}_{yy}$ is a $M \times M$ auto-correlation matrix of $y(n)$, given by

$$\mathbf{R}_{yy} = \begin{pmatrix} r_{yy}(0) & r_{yy}(-1) & \ldots & r_{yy}(-M+1) \\ r_{yy}(1) & r_{yy}(0) & \ldots & r_{yy}(-M+2) \\ \vdots & \vdots & \ddots & \vdots \\ r_{yy}(M-1) & r_{yy}(M-2) & \ldots & r_{yy}(0) \end{pmatrix}. \tag{6.19}$$

Consequently, from Eq.(6.18), the optimal filter coefficients can be written as

$$\mathbf{f} = \mathbf{R}_{yy}^{-1}\mathbf{r}_{uy}, \tag{6.20}$$

which is the Wiener solution to the optimal inverse filter. Clearly, to solve Eq.(6.20), we have to estimate only the auto-correlation of $y(n)$ and cross-correlation between $u(n)$ and $y(n)$. Therefore, in principle, the procedure of predictive deconvolution may be performed without the knowledge of $s(n)$.

Variations of Normal Equations

The whiteness assumption of the reflectivity sequence implies that

$$\mathrm{E}[u(n)u(n-k)] = \sigma_u^2\delta(k), \tag{6.21}$$

where $\delta(k)$ is the *Kronecker delta*. If we also know the shape of the probing signal $s(n)$, then, from Eq.(6.6) and the fact that the noise $v(n)$ is statistically independent of $u(n)$, the right-hand side of Eq.(6.17) can be simplified as

$$r_{uy}(k) = \mathrm{E}\left\{u(n)\left[\sum_{i=0}^{n-k} s(i)u(n-k-i) + v(n)\right]\right\}$$

$$
\begin{aligned}
&= \sigma_u^2 \sum_{i=0}^{n-k} s(i)\delta(i+k) \\
&= \sigma_u^2 s(-k)\delta(k). \qquad (6.22)
\end{aligned}
$$

Since $\{s(n)\}$ is assumed here to be causal, *i.e.*, $s(n) = 0$ for $n < 0$, we have $r_{uy}(0) = \sigma_u^2 s(0)$ and $r_{uy}(k) = 0$ for $1 \le k \le M-1$. Accordingly, the normal equations become

$$
\sum_{m=0}^{M-1} f(m) r_{yy}(k-m) = \sigma^2 s(-k)\delta(k), \qquad k = 0, 1, \ldots, M-1. \qquad (6.23)
$$

There is only one non-zero element corresponding to $k = 0$ on the right-hand side of Eq.(6.23). Thus, Eq.(6.18) will be

$$
\begin{pmatrix}
r_{yy}(0) & r_{yy}(-1) & \ldots & r_{yy}(-M+1) \\
r_{yy}(1) & r_{yy}(0) & \ldots & r_{yy}(-M+2) \\
\vdots & \vdots & \ddots & \vdots \\
r_{yy}(M-1) & r_{yy}(M-2) & \ldots & r_{yy}(0)
\end{pmatrix}
\begin{pmatrix} f(0) \\ f(1) \\ \vdots \\ f(M-1) \end{pmatrix}
=
\begin{pmatrix} \sigma_u^2 s(0) \\ 0 \\ \vdots \\ 0 \end{pmatrix}, \qquad (6.24)
$$

Equation (6.24) imposes no assumptions upon the noise process. Therefore, When the noise statistics is unknown, it should be used to solve for $f(n)$'s, and $r_{yy}(k)$'s be estimated directly from measured data samples of the reflected signals.

Moreover, if the noise statistics is indeed known, we have

$$
\begin{aligned}
r_{yy}(k) &= \mathrm{E}\left\{ \left[\sum_{i=0}^{n} s(i)u(n-i) + v(n) \right] \left[\sum_{m=0}^{n-k} s(m)u(n-k-m) + v(n-k) \right] \right\} \\
&= \sigma_u^2 \sum_{i=0}^{n} \sum_{m=0}^{n-k} s(i)s(m)\delta(k+m-i) + \mathrm{E}[v(n)v(n-k)] \\
&= \sigma_u^2 \sum_{m=0}^{n-k} s(m)s(m+k) + r_{vv}(k) \\
&= \sigma_u^2 r_{ss}(k) + r_{vv}(k), \qquad (6.25)
\end{aligned}
$$

where $r_{ss}(k) = \sum_{m=0}^{n-k} s(m)s(m+k)$ and $r_{vv} = \mathrm{E}[v(n)v(n-k)]$ are the auto-correlation functions of $s(n)$ and $v(n)$, respectively. Because $s(n)$ is a deterministic signal of finite energy, the definition of its auto-correlation $r_{ss}(k)$ is slightly different from that of a random process which is of finite power.

Substitution of Eq.(6.25) and Eq.(6.22) into Eq.(6.17) yields

$$\sum_{m=0}^{M-1} f(m)\left[\sigma_u^2 r_{ss}(k-m) + r_{vv}(k-m)\right] = \sigma_u^2 s(-k)\delta(k), \qquad k = 0, 1, \ldots, M-1. \tag{6.26}$$

Generally, solving Eq.(6.26) requires the complete knowledge of the second order statistics of the noise process as well as the auto-correlation function of $\{s(n)\}$. When the noise level is low, or $r_{vv}(k)$'s are negligible, then the Wiener solution depends solely on $r_{ss}(k)$'s. However, the Wiener filter does not depend on the phase characteristics of the probing signal, because two different input sequences may produces identical auto-correlation functions. The resulting Wiener filters in such cases will differ only by a scaler, $s(0)$.

6.3.3 Wiener Smoothing as Predictive Deconvolution

In the evaluation of bridge decks, data processing doesn't need to take place strictly in real-time. Certain amount of delay is tolerable, and the processing may be even performed off-line if necessary. This fact allows us to use a non-causal type of inverse filter which makes use of not only the 'past' but also the 'future' observations for the deconvolution. Such a filter are commonly referred to as a *smoother*. In particular, a Wiener smoother is the one that its output provides a minimum mean-squared error estimation of a desired signal.

Suppose that a smoother of order M and lag l is used for deconvolution, its output may be expressed as

$$\hat{u}(n/n+l) = \sum_{i=0}^{M-1} f(i)y(n+l-i), \tag{6.27}$$

where $0 < l < M$. The quantity l controls the number of data samples after the time instance n that are used to estimate $u(n)$. When $l = 0$, there is no 'future' data used in the estimation, thus, the smoother degenerates into a filter. For a stationary input $y(n)$, its characteristics does not change with time, therefore, the most appropriate way is to weigh both the 'past' and 'future' data equally in the estimation. This suggests that l should be equal to $M/2$. For convenience, we choose $M = 2L-1$ and $l = L$. Then, Eq.(6.27) can be rewritten as

$$\hat{u}(n/n+L) = \sum_{i=-L+1}^{L-1} f(i)y(n-i). \tag{6.28}$$

To satisfy the Wiener optimality criterion, the estimate's MSE, $E\{[\hat{u}(n/n+L) - u(n)]^2\}$, is to be minimized with respect to the filter coefficients, $f(n)$, $n = -L+1, -L+2, \ldots, 0, 1, \ldots, L-1$.

Following the derivation similar to those outlined in the previous section, we obtain the normal equations for the *Wiener smoother* as

$$\sum_{m=1-L}^{L-1} f(m) r_{yy}(k-m) = r_{uy}(k), \qquad k = 0, \pm 1, \ldots, \pm(L-1). \tag{6.29}$$

Substitution of Eq.(6.22) into Eq.(6.29) gives

$$\sum_{m=1-L}^{L-1} f(m) r_{yy}(k-m) = \sigma_u^2 s(-k)\delta(k), \qquad k = 0, \pm 1, \ldots, \pm(L-1), \tag{6.30}$$

where the value of $s(n)$ for $n < 0$ is not necessariiy zero due to the noncausality assumption for the smoothing operation. The matrix form of Eq.(6.30) is

$$\begin{pmatrix} r_{yy}(0) & r_{yy}(-1) & \ldots & r_{yy}(-2L+2) \\ r_{yy}(1) & r_{yy}(0) & \ldots & r_{yy}(-2L+3) \\ \vdots & \vdots & \ddots & \vdots \\ r_{yy}(2L-2) & r_{yy}(2L-3) & \ldots & r_{yy}(0) \end{pmatrix} \begin{pmatrix} f(-L+1) \\ f(-L+2) \\ \vdots \\ f(L-1) \end{pmatrix} = \sigma_u^2 \begin{pmatrix} s(L-1) \\ s(L-2) \\ \vdots \\ s(-L+1) \end{pmatrix}, \tag{6.31}$$

where $r_{yy}(-k) = r_{yy}(k)$ for real $y(n)$. Solving the normal equation for $f(n)$'s gives the optimal smoother for deconvolution. On the left-hand side of Eq.(6.31), the matrix elements, $r_{yy}(k)$'s can be replaced by the results obtained in Eq.(6.25).

As clearly shown in Eq.(6.31), the Wiener smoother requires the complete knowledge of the probing signal $\{s(n)\}$, as opposed to the Wiener filter which, in general, does not require such knowledge. Nevertheless, this is not necessary a disadvantage of the Wiener smoother, since the shape of $s(n)$ is obtainable through measurement. The additional information on the probing signal enables the Wiener smoother to produce a more accurate estimate of $\{u(n)\}$, and its output tends to be more impulsive in nature, thus a higher resolution. Improved accuracy is achieved also by the added 'future' observations in Wiener smoothing which generally contain more information about the desired signal than the observations from distant past [Mendel, 1983].

6.3.4 Predictive Error Filtering as Predictive Deconvolution

Another variation of predictive deconvolution is the use of *linear prediction error filters*. By assumption, the reflectivity sequence $\{u(n)\}$ is a white random process, thus completely unpredictable. This

suggests that $u(n)$ may be considered as the difference between the observable $y(n)$ and its estimate $\hat{y}(n/n-p)$ [Robinson, 1984b; Mendel, 1983], namely,

$$\hat{u}(n) = y(n) - \hat{y}(n/n-p), \tag{6.32}$$

where $\hat{y}(n/n-p)$ denotes the p-step ($p > 0$) prediction of $y(n)$ and is obtained by a *linear prediction filter*, $f(n)$, $n = 0, 1, \ldots, M-1$, such that

$$\hat{y}(n/n-p) = \sum_{m=0}^{M-1} f(m)y(n-p-m). \tag{6.33}$$

In practice, a one-step prediction filter ($p = 1$) is often used. Minimizing the mean square error of the prediction, $\mathrm{E}\{[\hat{y}(n/n-1) - y(n)]^2\}$, with respect to the filter coefficients, $f(n)$'s, results in the following set of normal equations,

$$\begin{pmatrix} r_{yy}(0) & r_{yy}(-1) & \ldots & r_{yy}(-M+1) \\ r_{yy}(1) & r_{yy}(0) & \ldots & r_{yy}(-M+2) \\ \vdots & \vdots & \ddots & \vdots \\ r_{yy}(M-1) & r_{yy}(M-2) & \ldots & r_{yy}(0) \end{pmatrix} \begin{pmatrix} f(0) \\ f(1) \\ \vdots \\ f(M-1) \end{pmatrix} = \begin{pmatrix} r_{yy}(1) \\ r_{yy}(2) \\ \vdots \\ r_{yy}(M) \end{pmatrix}, \tag{6.34}$$

which are called the *Yule-Walker equations* [Haykin, 1991].

Because $r_{yy}(-k) = r_{yy}(k)$, Eq.(6.34) may be augmented as

$$\begin{pmatrix} r_{yy}(0) & r_{yy}(-1) & \ldots & r_{yy}(-M) \\ r_{yy}(1) & r_{yy}(0) & \ldots & r_{yy}(-M+1) \\ \vdots & \vdots & \ddots & \vdots \\ r_{yy}(M) & r_{yy}(M-1) & \ldots & r_{yy}(0) \end{pmatrix} \begin{pmatrix} h(0) \\ h(1) \\ \vdots \\ h(M) \end{pmatrix} = \begin{pmatrix} \alpha \\ 0 \\ \vdots \\ 0 \end{pmatrix}, \tag{6.35}$$

where $h(0) = 1$, $h(n) = -f(n-1)$ for $n = 1, 2, \ldots, M$, and $\alpha = \sum_{m=0}^{M} h(m)r_{yy}(m)$.

The coefficients, $h(n)$'s, specified by Eq.(6.35) defines a one-step linear prediction error filter. A comparison between Eq.(6.35) and Eq.(6.24) indicates that the two equations are essentially identical except for a scale factor on their right-hand sides. Therefore, the one-step prediction error filter is equivalent to the Wiener filter when the latter is normalized such that $f(0) = 1$. This fact confirms the validity of the assumption that leads to Eq.(6.32) *i.e.*, the estimation of $u(n)$'s can be achieved through the linear prediction error filtering of $y(n)$.

Since there is a inherent relationship among the Wiener filtering, Wiener smoothing, and linear prediction error filtering, they are collectively referred to as predictive deconvolution in literatures [Silvia, 1979; Mendel, 1983]. The selection of a particular inverse filter for deconvolution depends on the amount of information available about the signal and noise characteristics. The normal equations associated, Eq.(6.24), Eq.(6.31) and Eq.(6.35), can all be readily solved by using the highly efficient *Levinson-Durbin algorithm* or its variation [Haykin, 1991; Golub, 1990; Marple, 1987].

In the above derivation, the reflected signal $y(n)$ is assumed to be from a stationary process. If this assumption does not hold, a simple solution is to divide the reflected signal into a number of segments of given length, then an average $r_{yy}(k)$ is used within each subintervals [Wang, 1969].

6.4 Deconvolution of Reflected Signals

6.4.1 Simulation of Reflected Signals

As addressed in Section 6.2, the reflected signal $y(n)$ from multi-layered media can be modeled as a convolution of the probing radar signal $s(n)$ with the reflectivity sequence $u(n)$ of the media, such that

$$y(n) = \sum_{i=0}^{n} u(i)s(n-i), \qquad \text{n=0,1,...,N.} \tag{6.36}$$

Since the impulse radar generates very narrow pulses, the length of the probing signal is much shorter than that of a whole trace of reflected signal. Suppose that the length of $\{s(n)\}$ is N_s (*i.e.*, the number of samples). Then, Eq.(6.36) may be rewritten as

$$y(n) = \sum_{i=0}^{N_s-1} s(i)u(n-i), \qquad \text{n=0,1,...,N,} \tag{6.37}$$

where $u(n) = 0$ for $n < 0$. In this chapter the measured radar pulse (real data), illustrated in Fig. 6.2, is used as $s(n)$ in Eq.(6.37) for simulation of the reflected signal.

The reflectivity sequence, $\{u(n)\}$, has non-zero values only at those n's that correspond to the physical interfaces in the multi-layered media. Since the sample number N of the sequence $\{u(n)\}$ is much larger than the number of physical layers in the media, the values of $u(n)$'s are zero for most of n's which correspond to the large number of artificial interfaces in the convolution sum model. The amplitude of $u(n)$ is related to the reflection coefficient at nth interface. For adjacent non-zero elements, $u(n_1)$ and $u(n_2)$ ($n_1 < n_2$), the difference in their time indices, $n_2 - n_1$, is a measure of

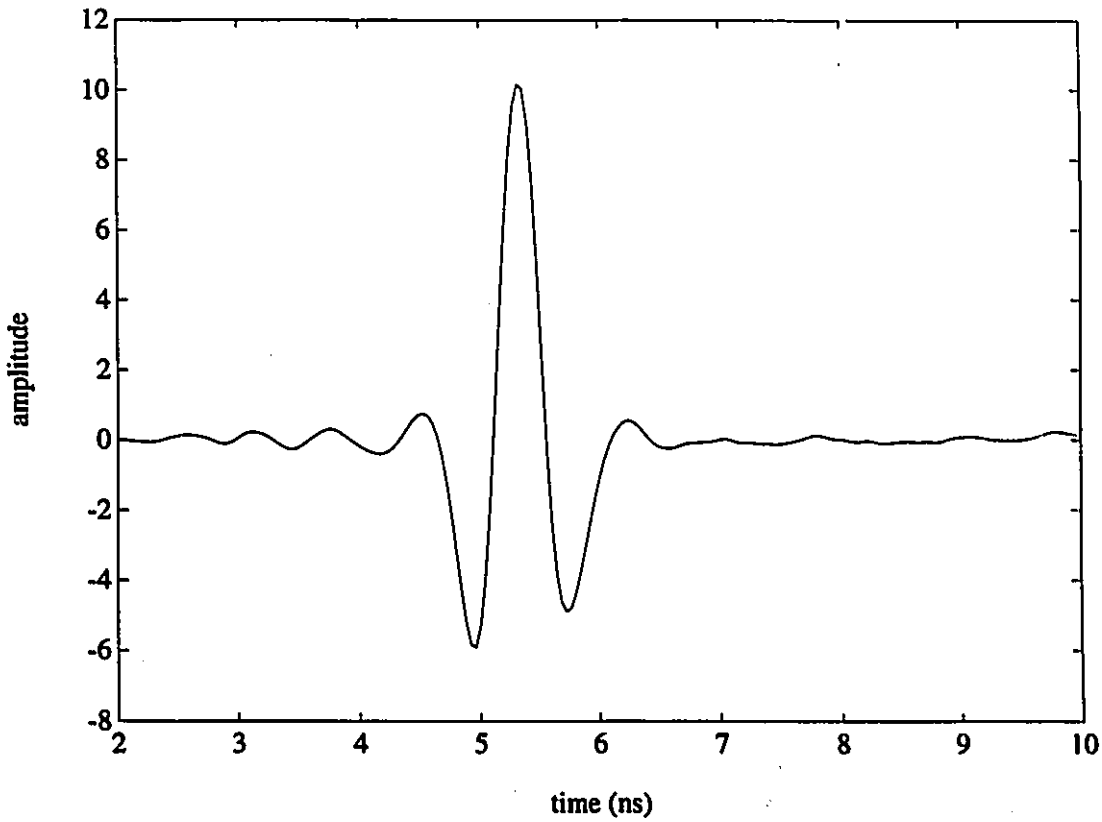

Figure 6.2: Measured waveform of probing radar signal $s(t)$. (Sampling period $T = 0.04$ ns.)

the thickness of a physical layer. Apparently, the reflected signal from a given layered media may be simulated by properly choosing the locations and amplitudes of non-zero elements in $\{u(n)\}$.

An example of such a reflectivity sequence is depicted in Fig. 6.3, where the non-zero elements of $\{u(n)\}$ are chosen to be $.45, .097, -.037, .044, .045$ at time instances $t_n = 5.32, 5.68, 6.52, 6.96, 8.52$ ns, respectively. The values of $t_n 0./$'s so chosen deviate slightly from those given in Chapter 3 and Chapter 4, because in the discrete convolution model, the time can be taken only at the integer multiples of sampling period T (*i.e.*, 0.04 ns). This fact limits the time resolution of the estimation of $u(n)$. The convolution of $u(n)$ with $s(n)$ results in a reflected signal as shown in Fig. 6.4. This waveform is in fact a simulation of the real reflected signal from a bridge deck which is also presented in Fig. 6.4 for a comparison. As we can see, the simulated data fit the real waveform reasonably well. This example demonstrates the simple convolutional model can be used as a approximation of the reflected signals from multi-layered media.

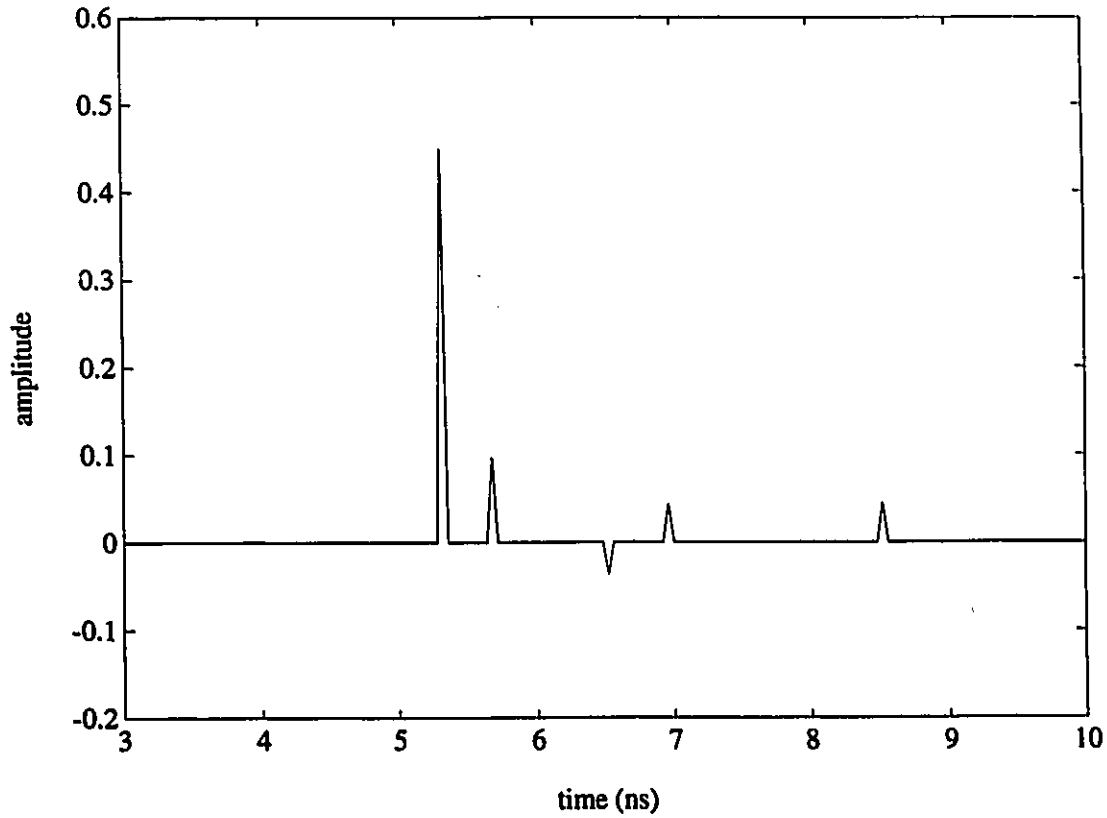

Figure

6.3: An example of reflectivity sequence $u(n)$, corresponding to $t_k = 5.32, 5.68, 6.52, 6.96, 8.52$ ns and $a_k = 0.45, 0.097, -.037, 0.044, 0.045$.

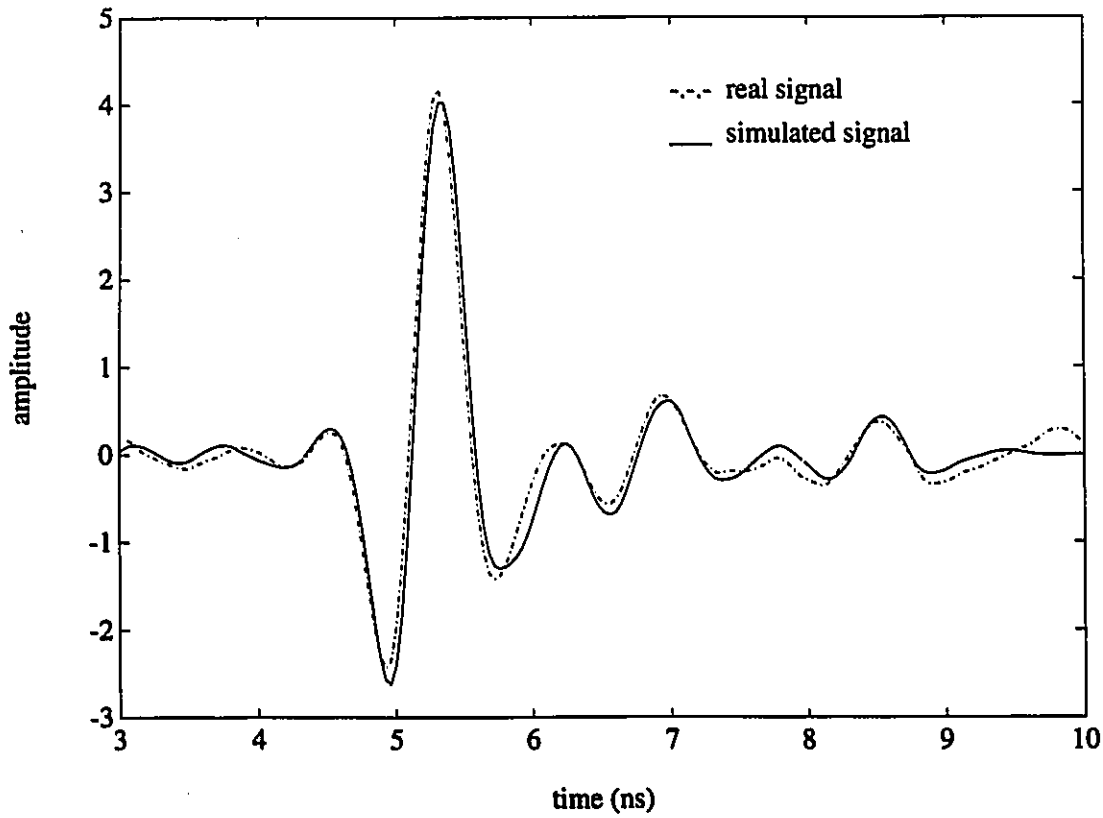

Figure 6.4: Simulation of reflected signal from a bridge deck. Simulated signal parameters: t_k = 5.32, 5.68, 6.52, 6.96, 8.52 ns, and a_k = 0.45, 0.097, −.037, 0.044, 0.045.

6.4.2 Implementation of Inverse Filters

Since the inverse filtering in the predictive deconvolution is carried out by Wiener filtering or smoothing, the key to its implementation is the proper design of the Wiener filter or smoother. As it has been discussed in Section 6.3, the coefficients (impulse responses) of Wiener filter and smoother can be determined by the normal equations, Eq.(6.24) and Eq.(6.31), respectively. Solving the normal equations requires the knowledge of the autocorrelation function of the reflected signal $r_{yy}(k)$, which can be evaluated from the received data samples by estimation, such that

$$\hat{r}_{yy}(k) = \frac{1}{N-k} \sum_{i=0}^{N-k} y(k+i)y(i), \tag{6.38}$$

where N is the total number of samples in the reflected signal $\{y(n)\}$. Figure 6.5 gives the normalized autocorrelation functions estimated from various types of data, which include the probing radar signal $s(n)$ as illustrated in Fig. 6.2, the reflected signal from a bridge deck and its simulated version as shown in Fig. 6.4. Since the probing radar signal $s(n)$ is known in our problem, Eq.(6.25) will be used to compute the autocorrelation function.

Once the autocorrelation function is determined, solving the normal equations can be carried out by highly efficient Levinson-Durbin algorithm. For the reasons that are provided in the previous discussion, the Wiener smoother usually offers better inverse filtering, hence a better candidate for the deconvolution. Therefore, in the following sections, the investigation will place emphasis on the performance of Wiener smoother in deconvolution, as the knowledge of $s(n)$ is readily available to us. Figure 6.6 depicts the impulse response of a Wiener smoother obtained by solving Eq.(6.31) for M=99, where M is the filter order, or the number of coefficients of the impulse response.

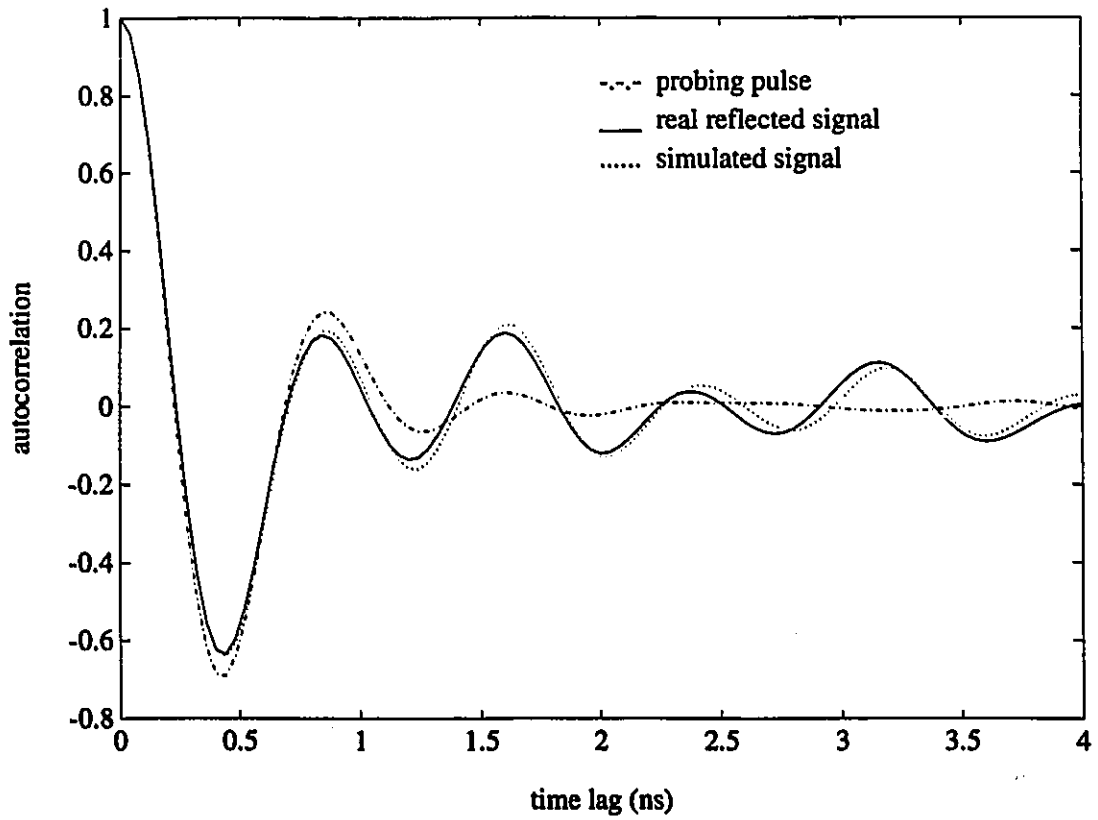

Figure 6.5: Normalized autocorrelation of various signals.

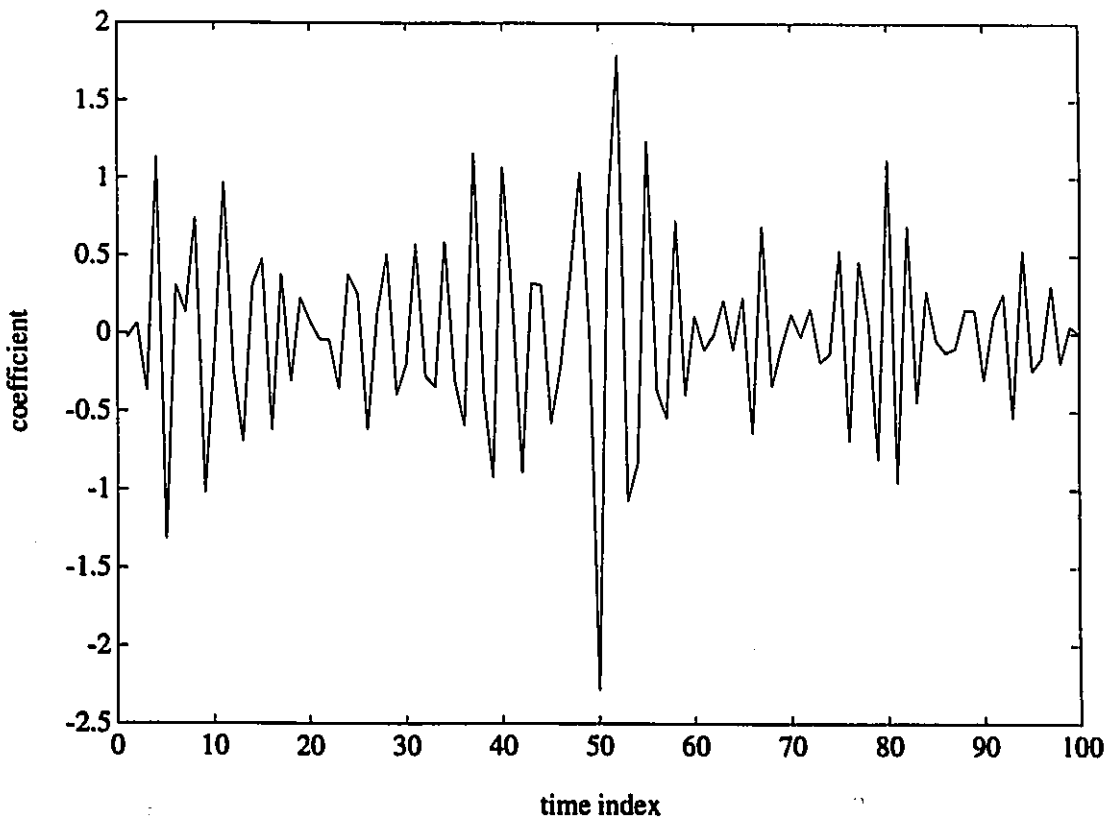

Figure 6.6: Impulse response of Wiener smoother of order M=99.

6.4.3 Deconvolution of Simulated Signals

Reflected Signals with Two Arrivals

To evaluate the feasibility and performance of the predictive deconvolution amounts to an assessment of how well it can retrieve the reflectivity sequence $u(n)$ from a reflected signal $y(n)$. This may be achieved by determining the ability of deconvolution to resolve two closely spaced arrivals in the reflected signal. Therefore, we begin with some examples of computer simulations where there are only two arrivals in the reflected signal, which corresponds to two non-zero elements in $\{u(n)\}$. Wiener smoothing operation is then performed to deconvolve the reflected signal, to provide an estimate of $\{u(n)\}$. The performance of the Wiener smoothing as deconvolution is investigated by varying the amplitudes and times of arrivals, as well as the signal-to-noise ratio of the reflected signal.

In the following examples, a Wiener smoother of order M=99 is used to perform the deconvolution. Our first example investigates the inverse filtering by Wiener smoother when the SNR is high and the separation between two arrivals in the reflected signal is large. As illustrated in Fig. 6.7, the two arrivals in the reflected signal occur at $t_1 = 5.0$ and $t_2 = 7.0$ ns, and the corresponding non-zero $u(n)$'s are are $a_1 = 0.4$ and $a_2 = 0.1$, respectively. The SNR is set to be 50 dB with respect to the weaker (second) arrival. The Wiener smoothing produces two very distinct peaks in the output, $\{\hat{u}(n)\}$. Note that the filter output in the figure is amplified by a factor of 10 for a clearer view, so that a peak of amplitude equal to 4, for instance, corresponds to a reflection coefficient $a_k = 0.4$. When the separation between the two arrivals is reduced to a few sampling periods ($Ts = 0.04$ ns), it is virtually impossible to distinguish them from each other in the reflected signal. Nevertheless, the Wiener smoother is still able to provide sufficient resolution in such cases, although the estimation of the weaker arrival may be less accurate.

In the second example as depicted in Fig. 6.8, the separation between the two arrivals is only 0.2 ns (5 sampling periods), and the SNR and reflection coefficients remain the same as in the first example. The two peaks related to the two arrivals are easily identifiable in the output. This example clearly demonstrates the capability of the Wiener smoother in resolving two arriving pulses very closely located in time. In fact, computer simulations reveal that the Wiener smoother is capable of resolving two arrivals as close as 0.12 ns (3 sampling periods) apart. However, the Wiener smoother fails, too, to produce two recognizable peaks when the separation is further reduced to 2 sampling periods (0.08 ns) or less.

While the Wiener smoother can separate very closely-located arrivals at a high SNR level, its performance is severely hampered by the presence of even a moderate level of noise. As exhibited in Fig. 6.9, at the Wiener smoother fails completely to produce an meaningful estimation of $\{u(n)\}$ sequence at SNR=30dB, even though the two arrivals in the input are well separated. The output is so noisy that the desired peaks at 5.0 and 7.0 ns are buried amidst many false peaks and not identifiable. An explanation will be outlined later in this section for the rapid deterioration of the deconvolution performance of the Wiener smoother in the presence of noise.

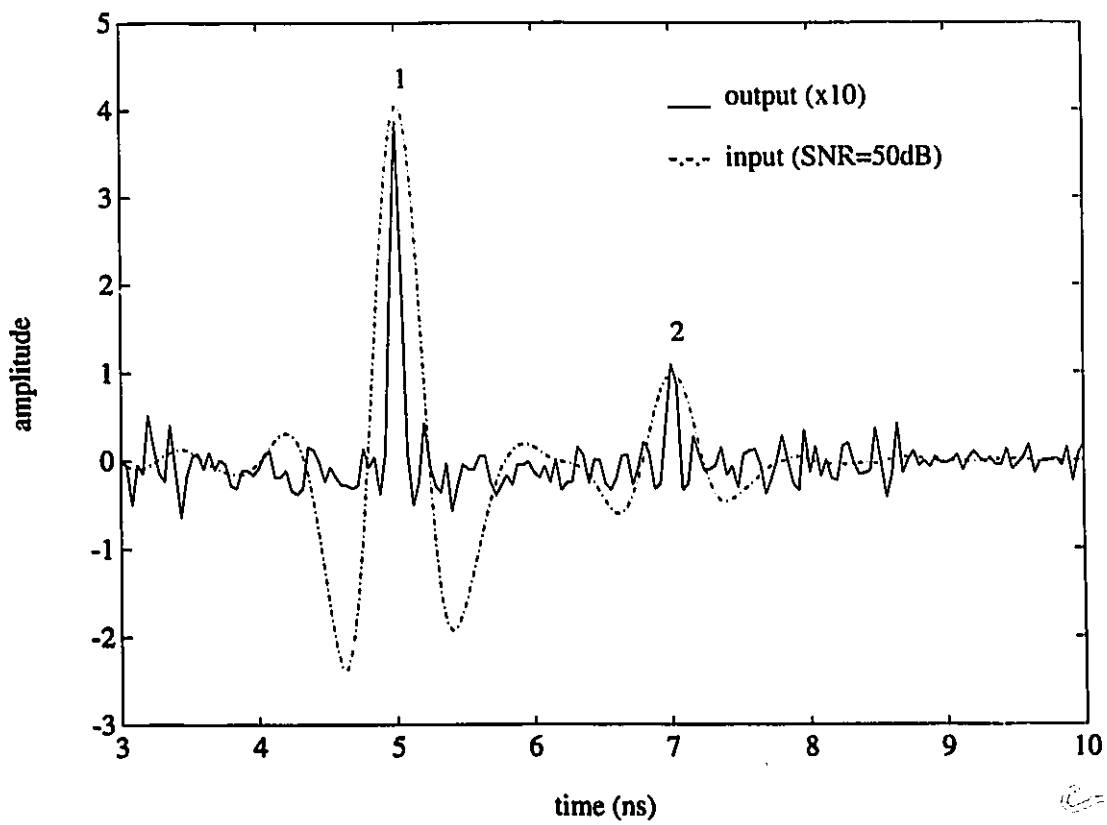

(The numbers marks the peak locations in the input.)

Figure 6.7: Deconvolution of reflected signal with two arrivals. Input signal parameters: $t_k = 5.0, 7.0$ ns, $a_k = 0.4, 0.1$, and SNR=50 dB.

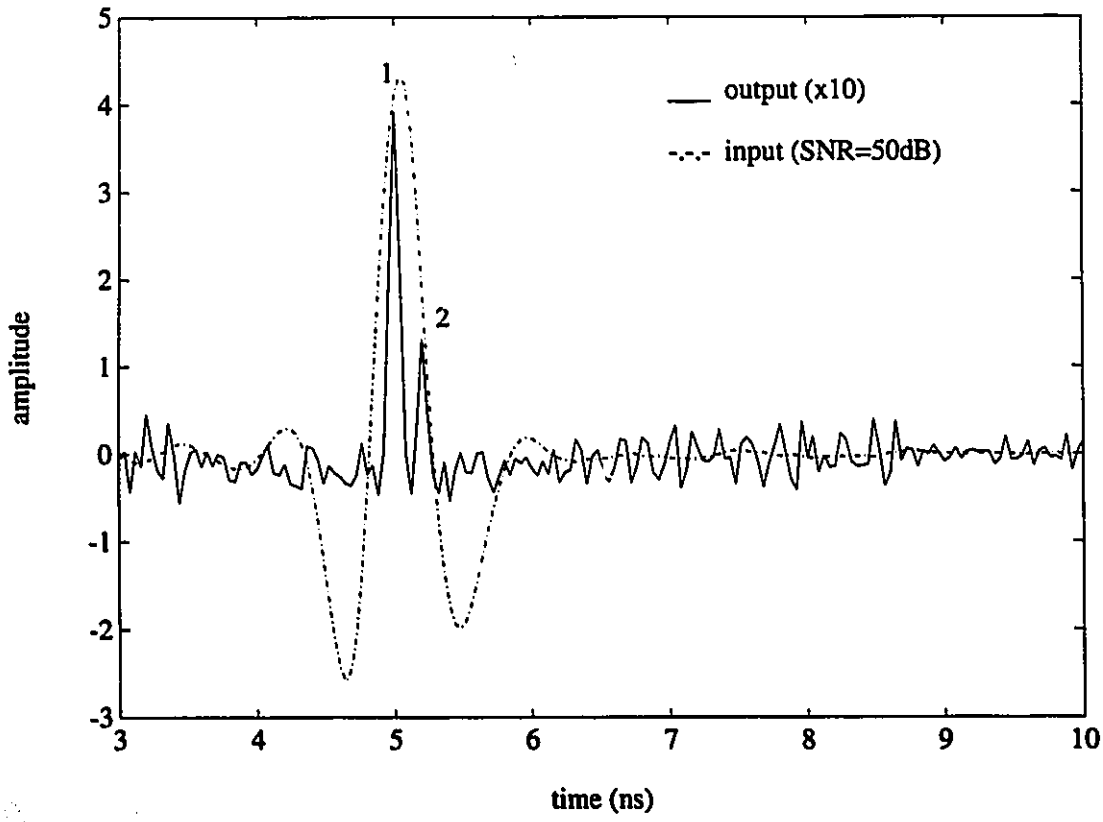

(The numbers marks the peak locations in the input.)

Figure 6.8: Deconvolution of reflected signal with closely-located arrivals. Input signal parameters: $t_k = 5.0, 5.2$ ns, $a_k = 0.4, 0.1$, and SNR=50 dB.

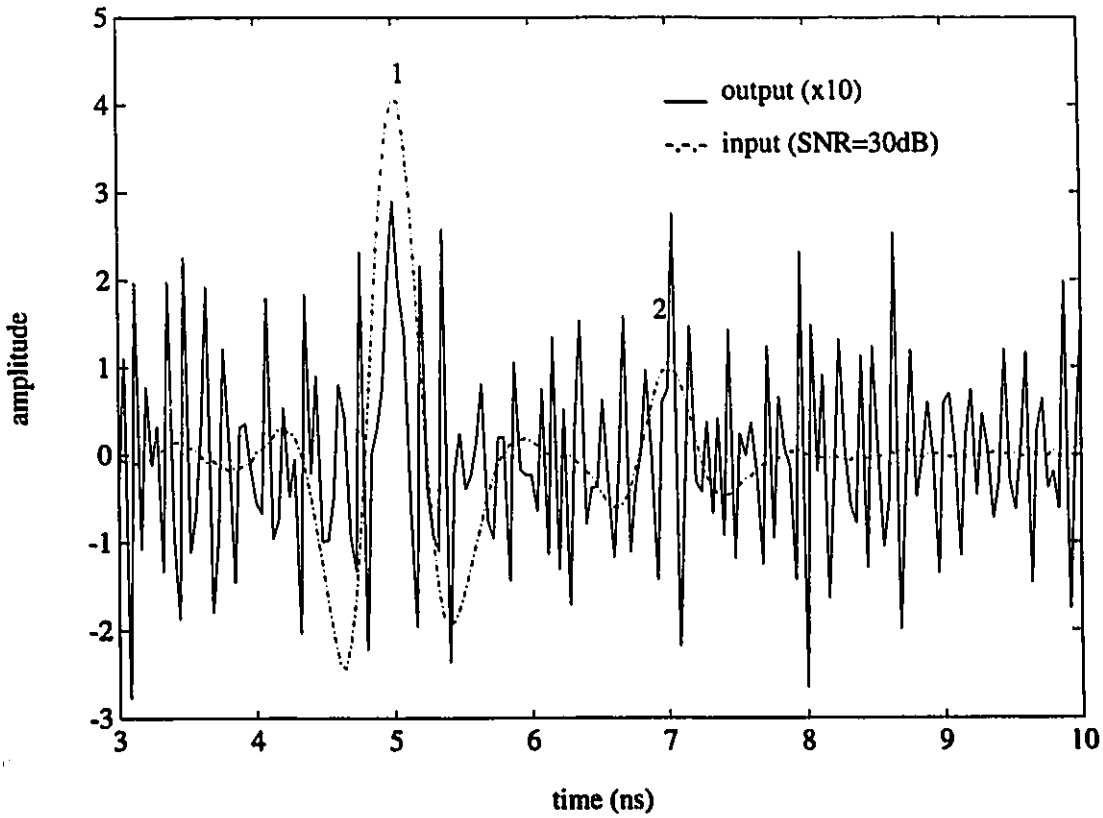

(The numbers marks the peak locations in the input.)

Figure 6.9: Deconvolution of reflected signal with two arrivals. Input signal parameters: $t_k = 5.0, 7.0$ ns, $a_k = 0.4, 0.1$, and SNR=30 dB

Estimation of Arrival Times and Reflection Coefficients

The estimates of the arriving times and reflection coefficients can be obtained from the output of inverse filter. In simulation, the reflected signals contains only two arrivals. The first non-zero element in $\{u(n)\}$ is chosen to be $a_1 = 0.4$ at time instance $t_1 = 5.0$ ns, and the second non-zero element is $a_2 = 0.1$ at times instances $t_2 = 5.2$, 6.0 and 7.0 ns. Again, the inverse filter used for deconvolution is a Wiener smoother of order M=99. The resulting estimates of t_1, t_2, a_1 and a_2 are summaried in Table 6.1 for various levels of SNR measured with respect to the second arrival.

Table 6.1: Deconvolution of reflected signals with two arrivals.

ture t_2		5.2 ns		6.0 ns		7.0 ns	
peak no. k		1	2	1	2	1	2
estimated	$\hat{t}_k$	5.000	5.200	5.000	6.000	5.000	7.000
SNR=∞	$\hat{a}_k$	.4029	.1117	.3989	.08869	.3985	.1130
estimated	$\hat{t}_k$	5.000	5.200	5.000	6.000	5.000	7.000
SNR=50 dB	$\hat{a}_k$	.3921	.1311	.3881	.08763	.3876	.0109
SNR=30 dB		failed		failed		failed	

Input signal parameters: $t_1 = 5.0$ ns, t_2 varies, $a_1 = 0.4$, $a_2 = 0.1$.

It is observed from Table 6.1 that at high SNR levels, the deconvolution produces virtually no error in the estimation of arrival times. This is partially due to the discrete nature of time in the signal so that any error less than a sampling period will not reflect in the estimate. However, the estimates of the reflection coefficients, a_1 and a_2 contain some errors even when SNR is high. This is in contrast to the ML estimates that are almost error-free when there is no noise. The most serious problem with predictive deconvolution is its sensitivity to the noise, as it fails completely at

SNR=30 dB.

6.4.4 Impact of Noise upon Predictive Deconvolution

As clearly demonstrated in Fig. 6.9 the performance of inverse filtering as deconvolution is greatly influenced by the presence of noise. In this section, we try to offer a brief explanation to this phenomenon.

Recall that the output of an inverse filter for deconvolution is an estimation of media's reflectivity sequence $\{u(n)\}$ as given in Eq.(6.7), namely,

$$\hat{u}(n) = g(n) * u(n) + f(n) * v(n), \tag{6.39}$$

where $f(n)$ is the impulse response of the inverse filter and $g(n) = f(n) * s(n)$ is the total response of the convolution-deconvolution system. If $f(n)$ is so chosen that $g(n) = \delta(n)$, then

$$\hat{u}(n) = u(n) + f(n) * v(n). \tag{6.40}$$

This is an ideal situation for producing the most impulsive $\hat{u}(n)$, hence a high resolution. However, it does not necessarily provide sufficient suppression of the noise component $v(n)$ which appears in the second term of Eq.(6.40). Obviously, an inherent conflict between the capability of noise suppression and the capability of 'pulse compression' always lies in the implementation of the predictive deconvolution.

In computing the impulse response of the Wiener smoother used in the above examples, the autocorrelation matrix $\mathbf{R}_{yy}$ is estimated from the probing signal $s(n)$ which contain little noise. The solution of the normal equation corresponds roughly to an inverse filter that maximizes the resolution but offers little noise reduction. To verify this analysis, the Wiener smoother is taken as an example for studying its characteristics in deconvolution.

For the Wiener smoother of order M=99, whose impulse response $f(n)$ is given in Fig. 6.6, its corresponding frequency spectrum (magnitude) is illustrated in Fig. 6.10 (marked as Wiener smoother 1), alone with the spectrum of the probing signal $s(n)$. It is observed that the Wiener smoother in our problem is essentially a highpass filter, and its frequency response is literally the inverse of the probing signal spectrum An importance feature to be noted is that the Wiener smoother provides a net gain for any frequency components that lie above 4 GHz, and the gain can be as high as 15 dB at some frequencies. Since the noise in the simulation is assumed to be a white random process, it contains rich high frequency components in its spectrum. After passing through the inverse filter,

these noise components are actually amplified and present at the filter output. Consequently, they overhelm the desired signal and lead to the failure of deconvolution.

To enhance the noise reduction capability, white noise that corresponds to a SNR level of 30 dB is added to the probing signal $s(n)$ for evaluating $\mathbf{R}_{yy}$, and the filter order is still chosen to be M=99. The resulting Wiener smoother has a frequency response which is also depicted in Fig. 6.10 (Wiener smoother 2) for a comparison. At low frequency, both smoothers have very similar response, but the the Wiener smoother 2, unlike the Wiener smoother 1, provides virtually no net gain for the high frequency components. Therefore, when being used for deconvolution, it produces much less noise in its output as illustrated in Fig. 6.12 where the input is identical to that in Fig. 6.9. The improvement in the noise suppression is achieved, however, at the expense of lower accuracy and reduced resolution of $\{\hat{u}(n)\}$. As demonstrated in Fig. 6.12, the resulting $\{\hat{u}(n)\}$ is no longer impulsive enough to distinguish arrivals closely located in time, since not only the high frequency noise is suppressed but also the fine structure of $\{u(n)\}$ is lost in the deconvolution.

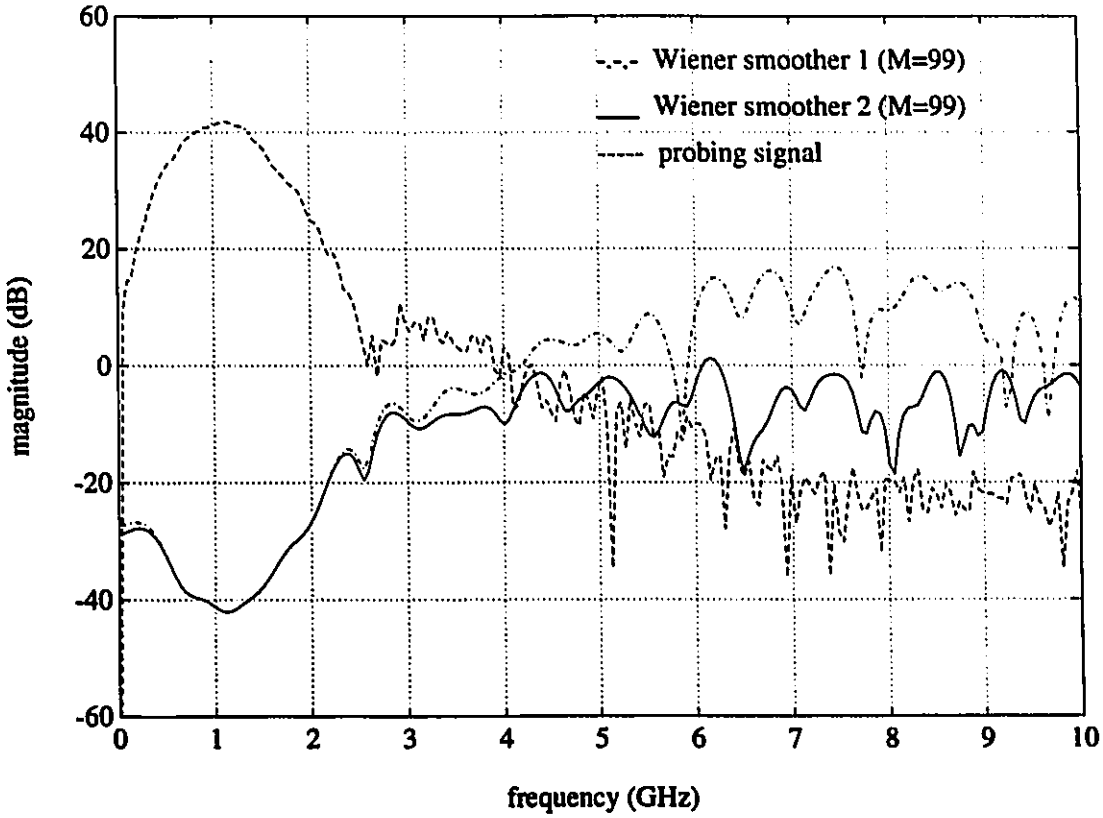

Figure 6.10: Frequency response of Wiener smoothers of order M=99.

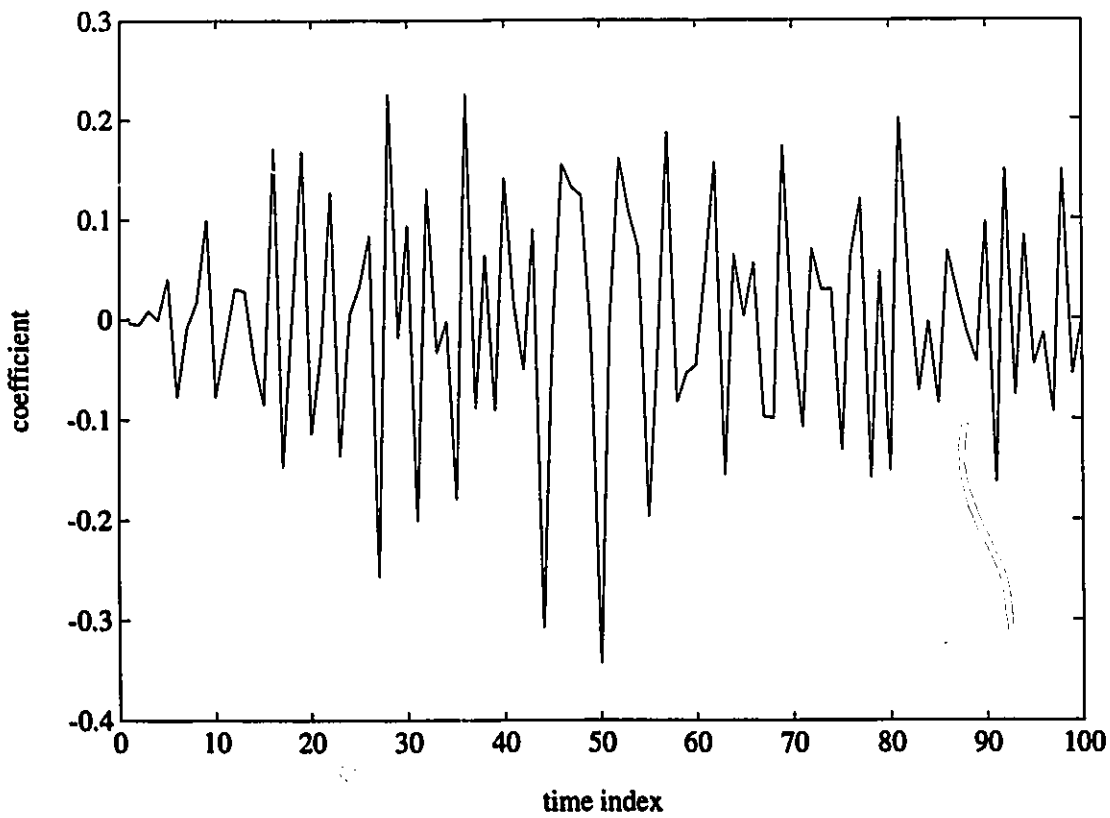

Figure 6.11: Impulse response of an alternative Wiener smoother of order M=99. Noise is added to $s(t)$ for computing $\mathbf{R}_{yy}$.

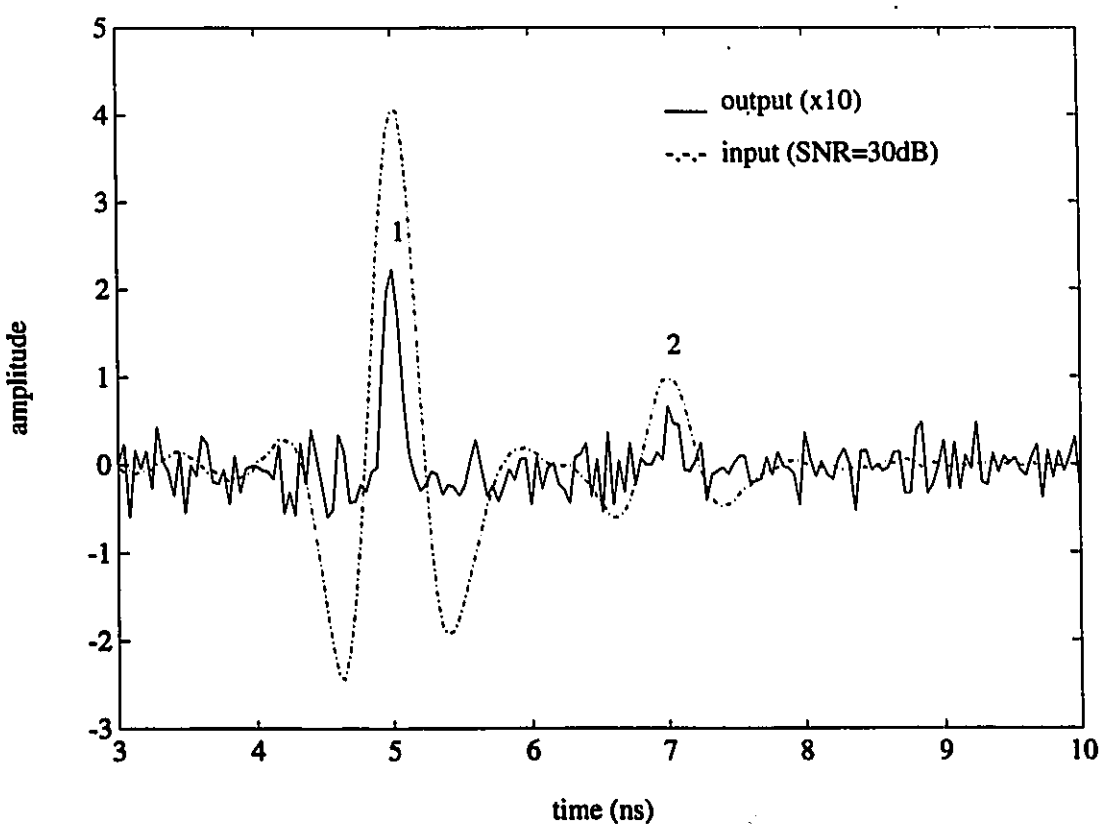

(The numbers marks the peak locations in the input.)

Figure 6.12: Deconvolution by the alternative Wiener smoother. Input signal parameters: t_k = 5.0, 7.0 ns, a_k = 0.4, 0.1, and SNR=30 dB.

6.4.5 Deconvolution of Reflected Signals from Bridge Decks

Deconvolution of Simulated Signal

As shown in Fig. 6.4, the reflected signal from a bridge deck can be simulated by convolving a reflectivity sequence $u(n)$ with the probing radar signal $s(n)$. Inverse filtering of the simulated signal by a Wiener smoother of order M=99 results in the output as illustrated in Fig. 6.13. There are two steps involved in the estimation of original $\{u(n)\}$: (1) to detect the presence and determine the locations of non-zero elements in $\{u(n)\}$ *i.e*, arrival times t_k's; and then (2) to estimate the amplitudes of these peaks, a_k's. To detect the non-zero elements in $\{u(n)\}$, two thresholds, one positive $\mu_1 > 0$, and one negative $\mu_2 < 0$, are applied upon the filter output. Anything that is greater the μ_2 but less than μ_1 is set to zero, and that greater than μ_1 or less than μ_2 is preserved in the output. Let $z(n)$ denote the output of an inverse filter. Then, the introduction of such thresholds yields an output $\hat{u}(n)$ which can be expressed as

$$\hat{u}(n) = \begin{cases} 0 & \text{if } \mu_2 < z(n) < \mu_1; \\ z(n) & \text{otherwise.} \end{cases} \tag{6.41}$$

By properly choosing μ_1 and μ_2, the unwanted false peaks in the filter output can be eliminated, while the desired peaks are saved. Once the non-zero elements are detected and located, the the values of the filter output at these time instances can be thus taken as the estimated a_k's.

Table 6.2 lists the estimates of t_k's and a_k's for the simulated signal as shown in Fig. 6.4 at two different levels of SNR measured with respect to the 3rd arrival (the weakest peak). Compared with results obtained by ML method (Table 3.1) or with those by eigenstructure-based method (Table 4.1), the estimates produced by predictive deconvolution are obviously much less accurate and more sensitive to the noise.

Deconvolution of Real Reflected Signal

When the deconvolution is applied to the real reflected signal, the result is, however, rather disappointing. Figure 6.14 shows the output of the deconvolution, by a Wiener smoother of order M=99, of the real reflected signal as illustrated in Fig. 6.4. In the output, almost all of the weak arrivals are not identifiable. It even fails to estimate accurately the reflection coefficient corresponding to the strongest arrival in the reflected signal (*i.e.*, the reflection from the air-asphalt surface) The poor

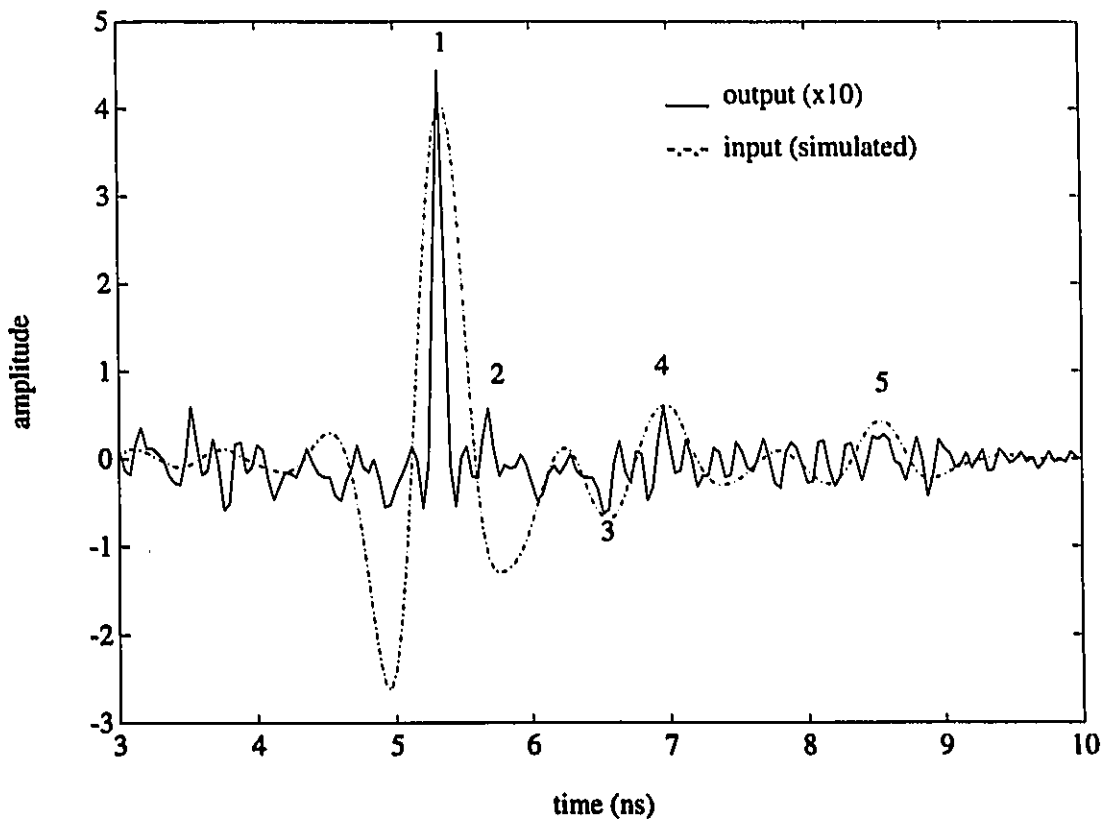

(The numbers marks the peak locations in the input.)

Figure 6.13: Deconvolution of simulated signal. Input signal parameters: t_k = 5.32, 5.68, 6.52, 6.96, 8.52 ns, and a_k = 0.45, 0.097, −.037, 0.044, 0.045.

Table 6.2: Deconvolution of simulated signals.

Peak no. k		1	2	3	4	5
true	t_k	5.320	5.680	6.520	6.960	8.520
parameters	a_k	0.450	0.097	-.037	0.044	0.045
estimated	$\hat{t}_k$	5.320	5.680	6.520	6.960	8.560
SNR=∞	$\hat{a}_k$	.4501	.05724	-.06294	.05936	.02722
estimated	$\hat{t}_k$	5.320	5.680	6.520	6.960	8.540
SNR=50 dB	$\hat{a}_k$	.4416	.05554	-.05771	.06001	.02856
SNR=30 dB		failed				

Input signal parameters:

$t_k = 5.32, 5.68, 6.52, 6.96, 8.52$ ns, and $a_k = 0.45, 0.097, -.037, 0.044, 0.045$.

performance of the Wiener smoother in the case of real signal could be contributed to the measurement noise and the discrepancy between the real signal and the convolutional signal model used to approximate it. Since the inverse filter is extremely sensitive to the noise as discussed earlier, the failure of deconvolution should be no surprise to us.

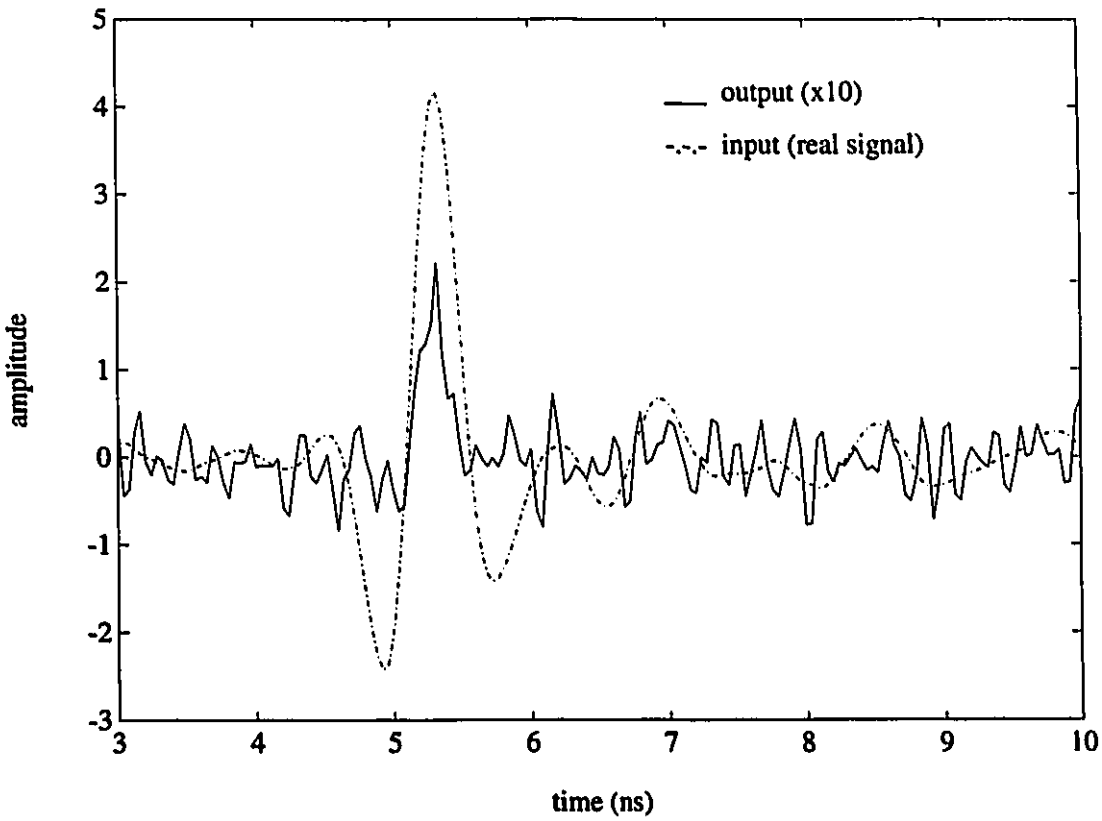

Figure 6.14: Deconvolution of real reflected signal.

6.5 Summary

In this chapter the reflected signals from multi-layered media is represented by the convolution of reflectivity sequence of the media with probing radar signal. Then, the concept of predictive

deconvolution is introduced, and normal equations are derived for Wiener filter, prediction-error filter and Wiener smoother. Wiener smoothing as the deconvolution is performed on both simulated and real reflected signals with various degrees of success. It has been found that Wiener smoother as the inverse filter is capable of resolving two arrivals closely located in time. Its implementation is carried out by simply solving the normal equations, and its operation involves only straightforward linear filtering which demands little computation and, thus, can be be easily performed in real time. However, the performance of predictive deconvolution deteriorates quickly in the presence of even a moderate level of noise in the input signal. This weakness severely restricts its usefulness in the applications to the problems such as the bridge deck evaluation.

Chapter 7

Conclusions

7.1 Summary and Conclusions

This thesis is concerned with the modeling of the impulse radar signals reflected from asphalt-covered bridge decks and extracting relevant information about the subsurface features of the bridge decks from the reflected signal. Essentially, it follows a statistical parameter estimation approach to the solution of the problem.

The bridge deck under our consideration may be regarded as media of multiple layers, consisting of asphalt, membrane, concrete, and reinforcing bars. For simplicity, the media are assumed to be stratified, lossless, and horizontally layered with each layer being homogeneous and isotropic. In the context of electromagnetic wave propagation, such a multi-layered media system is completely described by a set of characteristic parameters of the media, namely, the reflection coefficients associated with the interfaces, r_k's, and the one-way travel times for electromagnetic wave in the layers, τ_k's. It is further demonstrated in the thesis that the waveform of radar-generated pulses can be closely approximated by a modulated Gaussian function, $s(t)$. For normal incidence and non-dispersive media, the received signal at surface is regarded as a superposition of scaled and delayed replicas of the probing pulse, $s(t)$. This leads to the delayed sum model for the reflected signal. In addition, the scaling factors in the model are very close to the reflection coefficients and the number of reflected pulses are equal to the number of layers when the reflection coefficients are sufficient small, or equivalently, when the multiple reflections can be ignored. The effectiveness of the suggested signal model is supported by the simulation examples.

Based on the the parametric model of the reflected radar signals as developed in the thesis, the maximum likelihood method is then formulated and applied to estimating the characteristic parameters of the media, namely, a_k's and t_k's. The computer simulation results demonstrate that the ML method is capable of resolving very closely spaced arrivals in the reflected signals. At high SNR levels, it yields very accurate parameters estimates, since the mean squared errors of the estimates approach the Cramér-Rao Lower Bounds with the increase of SNR. At lower SNR levels, however, its performance deteriorates faster than what is predicted by CRLB, due to the nonlinear nature of the ML method. The ML method is also shown to be applied successfully to the estimation of real radar signal reflected from a bridge deck. Despite the superior error performance of the ML method, there are two major obstacles to its effective use in practice: firstly, it requires the explicit knowledge of the probability density function of the received signals which may not be always available; and secondly, the ML estimation usually involves a nonlinear optimization procedure where the iterative search for a globally optimal solution can be extremely time-consuming.

To overcome the difficulties in implementation of ML estimation, a new eigenstructure-based method is developed in this thesis, by making some major modifications to the existing eigenstructure-based DOA estimation techniques. The eigenstructure-based estimation method requires only the autocovariance of the reflected signal, which is a second order statistics and can be easily estimated from received data. Moreover, the EB method is more efficient in computation than the ML method, since it mainly involves the eigen-decomposition of the covariance matrix, which usually demands less computation than the nonlinear optimization. In principle, the EB method exploits the properties of the eigenstructure of the data covariance matrix to decompose the received data into signal subspace and noise subspace which are mutually orthogonal. The signal parameters can be then determined by minimizing (maximizing) the projection of the data into noise (signal) subspace. In the derivation of the EB method, the spectral smoothing technique is employed to resolve the rank deficiency problem in forming the data covariance matrix. As illustrated by simulations, the EB method produces good estimates of the parameters at high SNR levels, but the estimates become inaccurate when SNR level is low and the radar returns in the reflected signal are very closely spaced. Because new EB method imposes very few restrictions on the reflected signals, it can be applied to the more general problems of resolution and estimation of overlapping echos.

A thorough analysis of the limiting performance of the parameter estimators for the given signal model is carried out in the thesis by deriving the Cramér-Rao Lower Bound on the estimation error. It predicts the best achievable error performance and provides a basis with which the estimators'

accuracy can be compared under various situations, such as reflected signals with different sets of signal parameters and different levels of SNR's. More importantly, it gives us an insight into how the signal parameters and other factors affect the estimation performance. The analysis demonstrates that when the time separation between two arrivals is below certain finite value, the error of any parameter estimator will become extremely large. In other words, any parameter estimation will fail completely in such a case. The simulation results confirm this prediction by the analysis.

As an alternative to the parametric model, the reflected signals from multi-layered media may also be represented by the convolution of reflectivity sequence of the media with the probing radar signal. Based upon this model, the techniques of predictive deconvolution are developed, which is essentially an application of Wiener optimal filtering theory to the deconvolution problem. Wiener smoothing as the deconvolution is performed on both simulated and real reflected signals with various degrees of success. It is observed that the Wiener smoother as the inverse filter is capable of resolving arrivals very closely located in time. Its implementation is carried out by simply solving a set of linear, normal equations, and its operation involves only straightforward linear filtering which demands little computation, thus can be be easily performed in real time. However, the performance of predictive deconvolution deteriorates quickly in the presence of even a moderate level of noise in the input signal. This weakness severely restricts its usefulness in the applications to the problems such as the bridge deck evaluation.

7.2 Suggestions for Further Research

To carry on the study initiated in this thesis so that the proposed estimation techniques can be used more effectively in practice, there are two major areas for further investigation and improvement.

First of all, as one may be aware of, in the derivation of the delayed sum model for the reflected signals, we assumed lossless media, plane wave, and white noise. Although this simple model works quite well in most of the cases, it is obviously not adequate for further reducing the estimation error and/or extracting more information from the reflected signals about the subsurface conditions of a bridge deck. One possible improvement to the signal model is to make some modification to accommodate the effects of media absorption, non-white noise, and spheric divergence in the propagation of electromagnetic waves. The parameter estimation in the presence of unknown colored

noise may be achieved by the *maximum a posterior* method proposed by Wong et al [Wong, 1992].

In addition, more work has to be done on the determination of the number of the returns, K, in the reflected signal, when the number of layers in the bridge deck under inspection is unknown. The difficulty is that in order to overcome the rank deficiency problem, the signal covariance matrix can be only obtained only by performing spectral smoothing. Doing so, however, makes the data samples no longer uncorrelated, even though the noise is white. Consequently, the existing effective detection techniques [Wax, 1985; 1989] can not be applied directly, since those methods all assume uncorrelated data samples in derivation.

Appendix A

Analysis of Cramér-Rao Lower Bounds on Estimation Errors

In any practical system, the observations inevitably contain certain amount of noise, such as measurement error, modeling error, and ambient noise, to name a few. The presence of the random noise affects and, ultimately, limits the accuracy of the parameter estimation. In fact, the estimation error is bounded from below by a lower limit and, for a unbiased estimator, it is usually described by the Cramér-Rao Lower Bound (CRLB). In this appendix, we will first derive the likelihood function for the reflected signals of continuous waveforms and the associated Fisher's information matrix. Then, the CRLB on the estimator is calculated for both single-layer and multi-layer reflections. It not only predicts the lowest error possibly attainable by various estimators but also provides a reference with which the performances of different estimation techniques can be compared.

A.1 Likelihood Function and Fisher's Information Matrix

In Chapter 2, we have demonstrated that the reflected radar waveform $y(t)$ can be approximated by the sum of delayed pulses, which we rewrite here as

$$y(t) = g(t; \mathbf{a}, \mathbf{t}) + v(t)$$

$$= \sum_{k=1}^{K} a_k s(t - t_k) + v(t), \qquad t \in (0, T_r), \tag{A.1}$$

where $\mathbf{a}$ and $\mathbf{t}$ are the characteristic parameters, $v(t)$ a white Gaussian process with zero mean and power spectrum density (PSD) $N_0/2$, and $s(t)$ is given by

$$s(t) = Ae^{-\beta t^2} \cos(\omega_c t), \tag{A.2}$$

Note that $s(t)$ is an even function of t which decays very fast with t, i.e., $s(t) \approx 0$ for $| t | \gg 0$, since the radar impulse is of very short duration.

Let $\{\phi_i(t), i = 1, 2, \ldots\}$ be an *arbitary* complete set of orthonormal functions. Then $y(t)$, $g(t; \mathbf{a}, \mathbf{t})$ and $v(t)$ can be approximated by $y_N(t)$, $g_N(t)$ and $v_N(t)$, respectively, which are weighted sums of $\phi_i(t)$'s:

$$\begin{aligned} y_N(t) &= \sum_{i=1}^{N} y_i \phi_i(t), \\ g_N(t) &= \sum_{i=1}^{N} g_i \phi_i(t), \\ v_N(t) &= \sum_{i=1}^{N} v_i \phi_i(t), \end{aligned} \tag{A.3}$$

where y_i, g_i and v_i $(i = 1, 2, \ldots N)$ are coefficients given by

$$\begin{aligned} y_i &= \int_0^{T_r} y(t)\phi_i(t)\, dt, \\ g_i &= \int_0^{T_r} g(t; \mathbf{a}, \mathbf{t})\phi_i(t)\, dt, \\ v_i &= \int_0^{T_r} v(t)\phi_i(t)\, dt. \end{aligned} \tag{A.4}$$

As N increases, $y_N(t)$ approaches $y(t)$ (in the probabilistic sense), i.e.,

$$\lim_{N \to \infty} y_N(t) = y(t).$$

Similarly,

$$\begin{aligned} \lim_{N \to \infty} g_N(t) &= g(t; \mathbf{a}, \mathbf{t}), \\ \lim_{N \to \infty} v_N(t) &= v(t). \end{aligned} \tag{A.5}$$

It is easy to show that v_i's are also white Gaussian random variables with zero mean and variance $N_0/2$. Therefore the joint probability density function (PDF) of $\{v_i,\ i = 1, 2, \ldots, N\}$ can be written as

$$p_{\mathbf{v}}(\mathbf{v}) = \prod_{i=1}^{N} \frac{1}{\sqrt{\pi N_0}} \exp\left\{-\frac{1}{2}\frac{v_i^2}{N_0/2}\right\}, \tag{A.6}$$

where $\mathbf{v} \stackrel{\text{def}}{=} (v_1, v_2, \ldots, v_N)$. By substituting $y_i = g_i + v_i$ into Eq.(A.6), we obtain the PDF of N observables $(y_1, y_2, \ldots, y_N) \stackrel{\text{def}}{=} \mathbf{y}$, namely,

$$p_{\mathbf{y}}(\mathbf{y}) = \prod_{i=1}^{N} \frac{1}{\sqrt{\pi N_0}} \exp\left\{-\frac{(y_i - g_i)^2}{N_0}\right\}. \tag{A.7}$$

By intuition, the likelihood function of $(\mathbf{a}, \mathbf{t})$ based on N observations, denoted by $\ell_N(\mathbf{a}, \mathbf{t})$, can be defined equal to Eq.(A.7). However, this will lead to divergence when we let $N \to \infty$. To overcome this problem, we make use of the property that a likelihood function of $(\mathbf{a}, \mathbf{t})$ can be scaled by any factor which does not depend upon $(\mathbf{a}, \mathbf{t})$ [Van Trees, 1968]. Therefore, we may define the likelihood function $\ell_N(\mathbf{a}, \mathbf{t})$ as Eq.(A.7) divided by Eq.(A.6) such that

$$\begin{aligned} \ell_N(\mathbf{a}, \mathbf{t}) &\stackrel{\text{def}}{=} p_{\mathbf{y}}(\mathbf{y})/p_{\mathbf{v}}(\mathbf{v}) \\ &= \prod_{i=1}^{N} \exp\left\{-\frac{(y_i - g_i)^2 - v_i^2}{N_0}\right\}. \end{aligned} \tag{A.8}$$

Taking the logarithm of Eq.(A.8) and ignoring terms that do not depend upon parameters $\mathbf{a}$ and $\mathbf{t}$ gives the log-likelihood function $L_N(\mathbf{a}, \mathbf{t})$:

$$\begin{aligned} L_N(\mathbf{a}, \mathbf{t}) &\stackrel{\text{def}}{=} \ln \ell_N(\mathbf{a}, \mathbf{t}) \\ &= \frac{2}{N_0}\sum_{i=1}^{N} y_i g_i - \frac{1}{N_0}\sum_{i=1}^{N} g_i^2. \end{aligned} \tag{A.9}$$

By Parseval's theorem, the two sums in Eq.(A.9) are readily expressed as integrals. From Eq.(A.3) and Eq.(A.4), we have

$$\sum_{i=1}^{N} y_i g_i = \int_0^{T_r} y_N(t) g_N(t)\, dt,$$

and

$$\sum_{i=1}^{N} g_i^2 = \int_0^{T_r} g_N^2(t)\, dt. \tag{A.10}$$

Now, letting $N \to \infty$ and recalling the results in Eq.(A.5), we obtain the log-likelihood function

$$L(\mathbf{a}, \mathbf{t}) \stackrel{\text{def}}{=} \lim_{N\to\infty} L_N(\mathbf{a}, \mathbf{t})$$

$$= \frac{2}{N_0}\int_0^{T_r} y(t)g(t;\mathbf{a},\mathbf{t})\,dt - \frac{1}{N_0}\int_0^{T_r} g^2(t;\mathbf{a},\mathbf{t})\,dt. \tag{A.11}$$

Since the radar impulse $s(t)$ decays very fast with time t, so does $g(t;\mathbf{a},\mathbf{t})$, i.e., $g(t;\mathbf{a},\mathbf{t}) \approx 0$ for $t \gg 0$. Then the likelihood function for any given $y(t)$ can be very closely approximated by

$$L(\mathbf{a},\mathbf{t}) \approx \frac{2}{N_0}\int_{-\infty}^{\infty} y(t)g(t;\mathbf{a},\mathbf{t})\,dt - \frac{1}{N_0}\int_{-\infty}^{\infty} g^2(t;\mathbf{a},\mathbf{t})\,dt. \tag{A.12}$$

Denote $\boldsymbol{\theta} = (a_1, t_1, a_2, t_2, \ldots, a_K, t_K)^T$, i.e., $\theta_{2k-1} = a_k$ and $\theta_{2k} = t_k$ for $k = 1, \ldots, K$, and $L(\boldsymbol{\theta}) \equiv L(\mathbf{a},\mathbf{t})$. Then the Fisher's information matrix associated with the parameters $\mathbf{a}$ and $\mathbf{t}$ for given $y(t)$, $\mathbf{J}$, is defined as a $2K \times 2K$ matrix with its ijth element, J_{ij}, given by

$$J_{ij} = \mathrm{E}\left[\frac{\partial L(\boldsymbol{\theta})}{\partial \theta_i}\frac{\partial L(\boldsymbol{\theta})}{\partial \theta_j}\right], \tag{A.13}$$

or, equivalently,

$$J_{ij} = -\mathrm{E}\left[\frac{\partial^2 L(\boldsymbol{\theta})}{\partial \theta_i \partial \theta_j}\right]. \qquad \text{for } i,j = 1,2,\ldots,2K. \tag{A.14}$$

Suppose that $\hat{\theta}_i$ is an unbiased estimator of θ_i. Then the variance of $\hat{\theta}_i$, denoted by $\mathrm{Var}[\hat{\theta}_i]$, is bounded from below by the inequality

$$\mathrm{Var}[\hat{\theta}_i] \geq \Gamma_{ii}, \qquad \text{for } i = 1,2\ldots,2K, \tag{A.15}$$

where Γ_{ii} is the ith diagonal element of matrix $\boldsymbol{\Gamma} = \mathbf{J}^{-1}$. The quantity given by the right-hand side of Eq.(A.15) is commonly referred to as the Cramér-Rao Lower Bound (CRLB) on the estimator $\hat{\theta}_i$, which is the minimum attainable error for any unbiased estimator of θ_i. More specifically, Eq.(A.15) may be written in terms of $\mathbf{a}$ and $\mathbf{t}$, such that

$$\mathrm{Var}[\hat{a}_k] = \mathrm{Var}[\hat{\theta}_{2k-1}] \geq \Gamma_{2k-1,2k-1} \qquad \text{for } k = 1,2,\ldots,K; \tag{A.16}$$

$$\mathrm{Var}[\hat{t}_k] = \mathrm{Var}[\hat{\theta}_{2k}] \geq \Gamma_{2k,2k} \qquad \text{for } k = 1,2,\ldots,K. \tag{A.17}$$

Substitution of Eq.(A.12) into Eq.(A.14) yields

$$J_{ij} = -\frac{2}{N_0}\mathrm{E}\left\{\int_{-\infty}^{\infty}[y(t) - g(t;\boldsymbol{\theta})]\frac{\partial^2 g(t;\boldsymbol{\theta})}{\partial \theta_i \partial \theta_j}\,dt - \int_{-\infty}^{\infty}\frac{\partial g(t;\boldsymbol{\theta})}{\partial \theta_i}\frac{\partial g(t;\boldsymbol{\theta})}{\partial \theta_j}\,dt\right\}. \tag{A.18}$$

Since

$$\mathrm{E}[y(t) - g(t;\boldsymbol{\theta})] = \mathrm{E}[v(t)] = 0,$$

then

$$J_{ij} = \frac{2}{N_0}\int_{-\infty}^{\infty}\frac{\partial g(t;\boldsymbol{\theta})}{\partial \theta_i}\frac{\partial g(t;\boldsymbol{\theta})}{\partial \theta_j}\,dt, \tag{A.19}$$

for $i, j = 1, 2, \ldots, 2K$. Obviously, $J_{ij} = J_{ji}$, therefore matrix $\mathbf{J}$ is symmetric.

Once the elements of Fisher's information matrix $\mathbf{J}$ are all determined, the values of the Cramér-Rao Lower Bounds can be readily computed by taking inverse of $\mathbf{J}$, i.e., $\mathbf{\Gamma}$.

A.2 Cramér-Rao Lower Bounds for Single-Layer Reflection

For the case of a single-layer reflection, the reflected signal consists of only one arrival, i.e., $K = 1$ in Eq.(A.1). Then, the signal model,

$$g(t, \theta) = a_1 s(t - t_1) = a_1 A e^{-\beta(t-t_1)^2} \cos \omega_c (t - t_1), \tag{A.20}$$

contains two parameters. $\theta = (a_1, t_1)$. Correspondingly, there are three distinct elements in matrix $\mathbf{J}$, namely, J_{11}, J_{22}, and $J_{12} = J_{21}$.

A.2.1 Derivation of Fisher's Information Matrix

Some Useful Formulas of Integration

To determine the elements of $\mathbf{J}$, a number of definite integrals have to be evaluated. Listed below are some useful results for the calculation. They can be found in the reference [Gradshteyn, 1965], and will be referred to frequently in this appendix.

$$\int_{-\infty}^{\infty} e^{-px^2}\, dx = \sqrt{\frac{\pi}{p}}, \tag{A.21}$$

$$\int_{-\infty}^{\infty} x^2 e^{-px^2}\, dx = \frac{1}{2p}\sqrt{\frac{\pi}{p}}, \tag{A.22}$$

$$\int_{-\infty}^{\infty} e^{-px^2} \cos bx\, dx = \sqrt{\frac{\pi}{p}}\, e^{-b^2/4p}, \tag{A.23}$$

$$\int_{-\infty}^{\infty} x e^{-px^2} \sin bx\, dx = \frac{b}{2p}\sqrt{\frac{\pi}{p}}\, e^{-b^2/4p}, \tag{A.24}$$

$$\int_{-\infty}^{\infty} x^2 e^{-px^2} \cos bx\, dx = \frac{2p - b^2}{4p^2}\sqrt{\frac{\pi}{p}}\, e^{-b^2/4p}, \tag{A.25}$$

where the constant $p > 0$.

Calculation of J_{12} and J_{21}

Substituting Eq.(A.20) into Eq.(A.19) gives

$$J_{12} = J_{21} = \frac{2a_1}{N_0} \int_{-\infty}^{\infty} s(t-t_1) \frac{\partial s(t-t_1)}{\partial t_1} \, dt. \tag{A.26}$$

Furthermore, we have

$$\begin{aligned} \frac{\partial s(t-t_1)}{\partial t_1} &= a_1 A e^{-\beta(t-t_1)^2} \left[2\beta(t-t_1)\cos\omega_c(t-t_1) + \omega_c \sin\omega_c(t-t_1)\right] \\ &\stackrel{\text{def}}{=} s'(t-t_1). \end{aligned} \tag{A.27}$$

Let $u = t - t_1$, and note that $s(u) = s(t-t_1)$ is an even function of u and $s'(u) = -s'(t-t_1)$ is an odd function of u. It follows that

$$\begin{aligned} J_{12} &= J_{21} \\ &= \frac{2a_1}{N_0} \int_{-\infty}^{\infty} s(t-t_1) s'(t-t_1) \, dt \\ &= -\frac{2a_1}{N_0} \int_{-\infty}^{\infty} s(u) s'(u) \, du \\ &= 0. \end{aligned} \tag{A.28}$$

Therefore, **J** is a diagonal matrix.

Calculation of J_{11}

Also from Eq.(A.19), we have the diagonal element J_{11} as

$$\begin{aligned} J_{11} &= \frac{2}{N_0} \int_{-\infty}^{\infty} [s(t-t_1)]^2 \, dt \\ &= \frac{2A^2}{N_0} \int_{-\infty}^{\infty} e^{-2\beta(t-t_1)^2} \cos^2[\omega_c(t-t_1)] \, dt \\ &= \frac{A^2}{N_0} \left\{ \int_{-\infty}^{\infty} e^{-2\beta u^2} du + \int_{-\infty}^{\infty} e^{-2\beta u^2} \cos(2\omega_c u) \, du \right\} \\ &= \frac{A^2}{N_0} \sqrt{\frac{\pi}{2\beta}} \left(1 + e^{-\omega_c^2/2\beta}\right). \end{aligned} \tag{A.29}$$

In the last step in Eq.(A.29), we utilized the results of Eq.(A.21) and Eq.(A.23).

Calculation of J_{22}

Similarly, J_{22} is given by Eq.(A.19) as

$$J_{22} = \frac{2a_1^2}{N_0}\int_{-\infty}^{\infty}\left[\frac{\partial s(t-t_1)}{\partial t_1}\right]^2 dt.$$

Again, let $u = t - t_1$. It follows from Eq.(A.27) that

$$\begin{aligned}
&\left[\frac{\partial s(t-t_1)}{\partial t_1}\right]^2 \\
&= A^2 e^{-2\beta(t-t_1)^2}\{2\beta(t-t_1)\cos[\omega_c(t-t_1)] + \omega_c \sin[\omega_c(t-t_1)]\}^2 \\
&= A^2 e^{-2\beta u^2}\{\frac{\omega_c^2}{2} + 2\beta^2 u^2 - \frac{\omega_c^2}{2}\cos(2\omega_c u) \\
&\quad + 2\beta\omega_c u \sin(2\omega_c u) + 2\beta^2 u^2 \cos(2\omega_c u)\}. \qquad \text{(A.30)}
\end{aligned}$$

Then, J_{22} can be expressed as

$$J_{22} = \frac{2a_1^2 A^2}{N_0}(I_1 + I_2 + I_3 + I_4 + I_5), \qquad \text{(A.31)}$$

where the terms I_i's can by calculated by using Eq.(A.21) to Eq.(A.25), i.e.,

$$\begin{aligned}
I_1 &= \int_{-\infty}^{\infty}\frac{\omega_c^2}{2}e^{-2\beta u^2}du = \frac{\omega_c^2}{2}\sqrt{\frac{\pi}{2\beta}}; \\
I_2 &= \int_{-\infty}^{\infty}2\beta^2 u^2 e^{-2\beta u^2}du = \frac{\beta}{2}\sqrt{\frac{\pi}{2\beta}}; \\
I_3 &= -\int_{-\infty}^{\infty}\frac{\omega_c^2}{2}\cos(2\omega_c u)e^{-2\beta u^2}du = -\frac{\omega_c^2}{2}\sqrt{\frac{\pi}{2\beta}}\,e^{-\omega_c^2/2\beta}; \\
I_4 &= \int_{-\infty}^{\infty}2\beta\omega_c u\sin(2\omega_c u)e^{-2\beta u^2}du = \omega_c^2\sqrt{\frac{\pi}{2\beta}}\,e^{-\omega_c^2/2\beta}; \\
I_5 &= \int_{-\infty}^{\infty}2\beta^2 u^2\cos(2\omega_c u)e^{-2\beta u^2}du \\
&= \frac{1}{2}\sqrt{\frac{\pi}{2\beta}}(\beta - \omega_c^2)\,e^{-\omega_c^2/2\beta}. \qquad \text{(A.32)}
\end{aligned}$$

Finally, by combining the results from Eq.(A.32) with Eq.(A.31), we get

$$J_{22} = \frac{a_1^2 A^2}{N_0}\sqrt{\frac{\pi}{2\beta}}\left\{\omega_c^2 + \beta\left(1 + e^{-\omega_c^2/2\beta}\right)\right\}. \qquad \text{(A.33)}$$

A.2.2 CRLB on $\hat{a}_1$ and $\hat{t}_1$

Since the matrix $\mathbf{J}$ is diagonal ($J_{12} = J_{21} = 0$), the diagonal elements of $\mathbf{\Gamma} = \mathbf{J}^{-1}$, i.e., Γ_{11} and Γ_{22}, are readily obtained by

$$\begin{aligned} \Gamma_{11} &= J_{11}^{-1}, \\ \Gamma_{22} &= J_{22}^{-1}. \end{aligned}$$

From Eq.(A.29), Eq.(A.33) and Eq.(A.15), the Cramér-Rao Lower Bounds on the variances of $\hat{a}_1$ and $\hat{t}_1$ can be expressed as

$$\mathrm{Var}[\hat{a}_1] \geq \frac{N_0}{A^2}\sqrt{\frac{2\beta}{\pi}}\,(1+e^{-\omega_c^2/2\beta})^{-1}, \tag{A.34}$$

$$\mathrm{Var}[\hat{t}_1] \geq \frac{N_0}{a_1^2 A^2}\sqrt{\frac{2\beta}{\pi}}\left[\omega_c^2+\beta\,(1+e^{-\omega_c^2/2\beta})\right]^{-1}. \tag{A.35}$$

A few observations may be made on the Eq.(A.34) and Eq.(A.35). Firstly, the lower bounds of the estimators' errors depend on parameters of the probing radar pulse, namely, A, β, ω_c, as well as the reflection coefficient a_1, but independent of the arrival time t_1. It should be noted, however, that the independence of the estimation errors from t_1 holds only for the single-layer reflection. When the media consist of multiple layers, the CRLB do depend upon the time intervals between the radar returns. Secondly, for a given noise level (fixed N_0), the CRLB on the errors can be reduced by raising A and/or β. This agrees with our intuition, since increase of A is to raise the signal energy level and increase of β means to reduce the pulse-width of the probing radar signal, hence a higher resolution.

Recall that in Section 2.4 we have derived the signal-to-noise ratio for the k arrival as

$$\rho_k = \frac{a_k^2 A^2}{N_0}\sqrt{\frac{\pi}{2\beta}}\,(1+e^{-\omega_c^2/2\beta}).$$

Therefore, the inequalities for the estimation errors in Eq.(A.34) and Eq.(A.35) may be rewritten as

$$\mathrm{Var}[\hat{a}_1] \geq \rho_1^{-1} a_1^2, \tag{A.36}$$

$$\mathrm{Var}[\hat{t}_1] \geq \rho_1^{-1}\frac{1+e^{-\omega_c^2/2\beta}}{\omega_c^2+\beta(1+e^{-\omega_c^2/2\beta})}. \tag{A.37}$$

Figure A.1 illustrates the Cramér-Rao Lower Bounds so obtained for $A = 10.375$, $\beta = 3.574$, and $f_c = \omega_c/2\pi = 1.100$. The curves are plotted as $\mathrm{Var}[\hat{a}_1]/a_1^2$ and $\mathrm{Var}[\hat{t}_1]$ (in ns^2) against the signal-to-noise ratio.

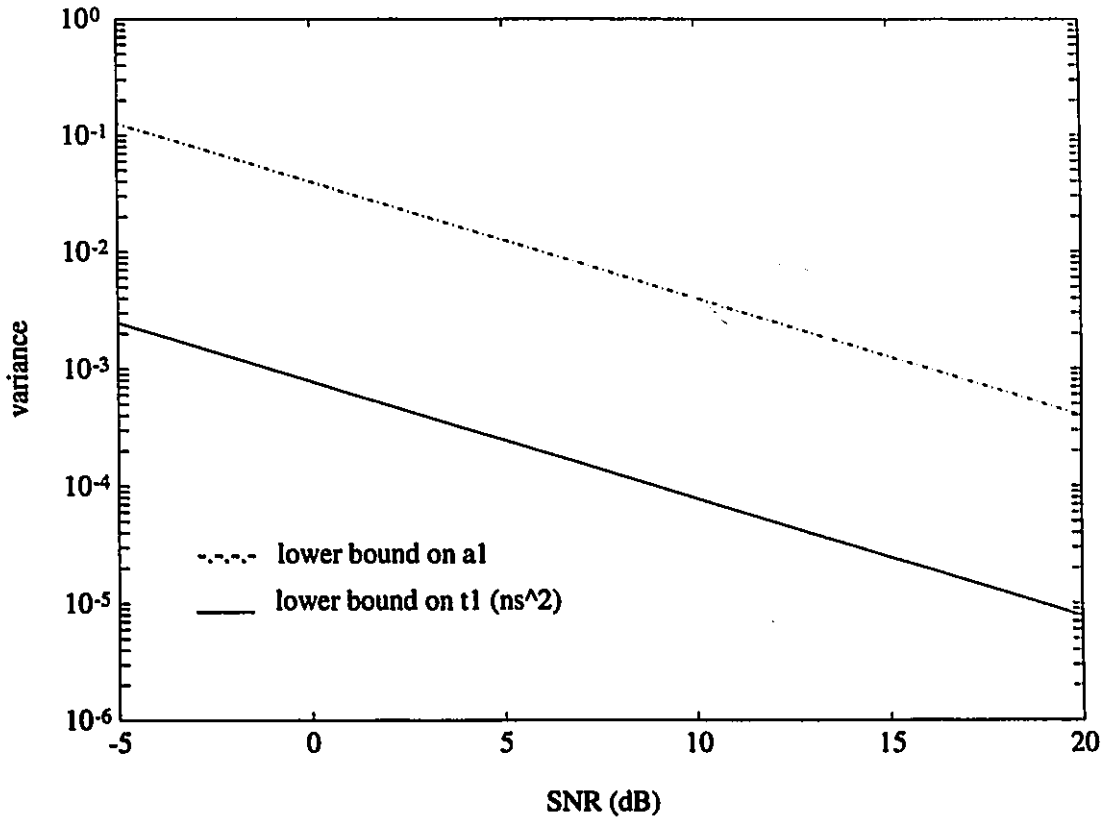

Figure A.1: CRLB's on $\mathrm{Var}[\hat{a}]/a^2$ and $\mathrm{Var}[\hat{t}]$ in single-layer reflection.

A.3 Cramér-Rao Lower Bounds for Multi-Layer Reflection

For multi-layer reflection, we have $K > 1$ in Eq.(A.1), and

$$g(t;\theta) = g(t;\mathbf{a},\mathbf{t}) = \sum_{k=1}^{K} a_k s(t-t_k), \tag{A.38}$$

where $\theta = (a_1, t_1, a_2, t_2, \ldots, a_K, t_K)^T$, i.e., $\theta_{2k-1} = a_k$ and $\theta_{2k} = t_k$ for $k = 1, 2, \ldots, K$.

A.3.1 Derivation of Fisher's Information Matrix

Since the elements of $\mathbf{J}$, J_{ij}'s, are related to the parameters θ_i's by Eq.(A.14), they fall into three categories, corresponding to

Case 1: $\theta_i = a_k$ and $\theta_j = a_m$, or $J_{ij} = J_{2k-1,2m-1}$, for $k, m = 1, 2, \ldots, K$;
Case 2: $\theta_i = t_k$ and $\theta_j = t_m$, or $J_{ij} = J_{2k,2m}$, for $k, m = 1, 2, \ldots, K$;
Case 3: $\theta_i = a_k$ and $\theta_j = t_m$, or $J_{ij} = J_{2k-1,2m}$, for $k, m = 1, 2, \ldots, K$;
Case 4: $\theta_i = t_k$ and $\theta_j = a_m$, or $J_{ij} = J_{2k,2m-1}$, for $k, m = 1, 2, \ldots, K$.

We deal with these cases one by one to determine all the elements, J_{ij}'s, for $i, j = 1, 2, \ldots, 2K$, in the following sub-sections.

Case 1: $J_{ij} = J_{2k-1,2m-1}$ when $\theta_i = a_k$ and $\theta_j = a_m$

For $\theta_i = a_k$ and $\theta_j = a_m$, we obtain from Eq.(A.19) that

$$\begin{aligned} J_{ij} &= \frac{2}{N_0}\int_{-\infty}^{\infty} \frac{\partial g(t;\mathbf{a},\mathbf{t})}{\partial a_k}\frac{\partial g(t;\mathbf{a},\mathbf{t})}{\partial a_m}\,dt \\ &= \frac{2}{N_0}\int_{-\infty}^{\infty} s(t-t_k)s(t-t_m)\,dt \\ &= \frac{2A^2}{N_0}\int_{-\infty}^{\infty} e^{-\beta[(t-t_k)^2+(t-t_m)^2]}\cos\omega_c(t-t_k)\cos\omega_c(t-t_m)\,dt. \end{aligned} \tag{A.39}$$

Define

$$d \stackrel{\text{def}}{=} \frac{1}{2}(t_k - t_m), \tag{A.40}$$

and

$$u \stackrel{\text{def}}{=} t - \frac{1}{2}(t_k + t_m), \tag{A.41}$$

It is obvious that

$$t - t_k = u - d \quad \text{and} \quad t - t_m = u + d. \tag{A.42}$$

Then, Eq.(A.54) can be rewritten as

$$J_{ij} = \frac{2A^2}{N_0} e^{-2\beta d^2} \int_{-\infty}^{\infty} e^{-2\beta d^2} \cos\omega_c(u-d) \cos\omega_c(u+d)\, du. \tag{A.43}$$

From the trigonometric identity

$$\cos x \cos y = \frac{1}{2}[\cos(x+y) + \cos(x+y)],$$

it follows that

$$J_{ij} = \frac{A^2}{N_0} e^{-2\beta d^2} \left\{ \cos(2\omega_c d) \int_{-\infty}^{\infty} e^{-2\beta u^2}\, du + \int_{-\infty}^{\infty} e^{-2\beta u^2} \cos(2\omega_c u)\, du \right\}$$

By recalling Eq.(A.21) and Eq.(A.23), We obtain

$$J_{ij} = J_{2k-1,2m-1} = \frac{A^2}{N_0} \sqrt{\frac{\pi}{2\beta}}\, e^{-2\beta d^2} \{\cos(2\omega_c d) + e^{-\omega_c^2/2\beta}\}, \tag{A.44}$$

for $k, m = 1, 2, \ldots, K$.

When $k = m$, we have $\theta_i = \theta_j = a_k$ and $d = (t_k - t_m)/2 = 0$. Obviously, this corresponds to the $(2k-1)$th diagonal element of $\mathbf{J}$, and Eq.(A.44) becomes

$$J_{2k-1,2k-1} = \frac{A^2}{N_0} \sqrt{\frac{\pi}{2\beta}} (1 + e^{-\omega_c^2/2\beta}), \qquad \text{for } k = 1, 2, \ldots, K. \tag{A.45}$$

Note that Eq.(A.45) is identical to Eq.(A.29), obtained by assuming a single-layer medium.

Case 2: $J_{ij} = J_{2k,2m}$ when $\theta_i = t_k$ and $\theta_j = t_m$

Let $\theta_i = t_k$ and $\theta_j = t_m$ in Eq.(A.19). It follows that

$$\begin{aligned} J_{ij} &= \frac{2}{N_0} \int_{-\infty}^{\infty} \frac{\partial g(t;\mathbf{a},\mathbf{t})}{\partial t_k} \frac{\partial g(t;\mathbf{a},\mathbf{t})}{\partial t_m}\, dt \\ &= \frac{2a_k a_m}{N_0} \int_{-\infty}^{\infty} \frac{\partial s(t-t_k)}{\partial t_k} \frac{\partial s(t-t_m)}{\partial t_m}\, dt, \end{aligned} \tag{A.46}$$

where the integrand is given by

$$\begin{aligned} F &\stackrel{\text{def}}{=} \frac{\partial s(t-t_k)}{\partial t_k} \frac{\partial s(t-t_m)}{\partial t_m} \\ &= \left\{ 2\beta A(t-t_k) e^{-\beta(t-t_k)^2} \cos\omega_c(t-t_k) + \omega_c A e^{-\beta(t-t_k)^2} \sin\omega_c(t-t_k) \right\} \times \\ &\quad \left\{ 2\beta A(t-t_m) e^{-\beta(t-t_m)^2} \cos\omega_c(t-t_m) + \omega_c A e^{-\beta(t-t_m)^2} \sin\omega_c(t-t_m) \right\}. \end{aligned}$$

Again, let $d = \frac{1}{2}(t_k - t_m)$ and $u = t - \frac{1}{2}(t_k + t_m)$. We have

$$\begin{aligned} F &= 4\beta^2 A^2 e^{-2\beta d^2}(u-d)(u+d)e^{-2\beta u^2}\cos\omega_c(u-d)\cos\omega_c(u+d) \\ &\quad + 2\beta\omega_c A^2 e^{-2\beta d^2}(u-d)e^{-2\beta u^2}\cos\omega_c(u-d)\sin\omega_c(u+d) \\ &\quad + 2\beta\omega_c A^2 e^{-2\beta d^2}(u+d)e^{-2\beta u^2}\sin\omega_c(u-d)\cos\omega_c(u+d) \\ &\quad + \omega_c^2 A^2 e^{-2\beta d^2} e^{-2\beta u^2}\sin\omega_c(u-d)\sin\omega_c(u+d) \\ &\stackrel{\text{def}}{=} A^2(F_1 + F_2 + F_3 + F_4). \end{aligned} \tag{A.47}$$

Then, the first term in Eq.(A.47) is

$$\begin{aligned} F_1 &= 2\beta^2 e^{-2\beta d^2}(u^2 - d^2)e^{-2\beta u^2}\{\cos 2\omega_c u + \cos 2\omega_c d\} \\ &= 2\beta^2 e^{-2\beta d^2} e^{-2\beta u^2}\{u^2\cos 2\omega_c u \\ &\quad - d^2\cos 2\omega_c u - u^2\cos 2\omega_c d + d^2\cos 2\omega_c d\}. \end{aligned}$$

From Eqs.(A.21), (A.22), (A.23), and (A.25),

$$\begin{aligned} &\int_{-\infty}^{\infty} F_1\,du \\ &= 2\beta^2 e^{-2\beta d^2}\sqrt{\frac{\pi}{2\beta}}\left\{\frac{\beta - \omega_c^2}{4\beta^2}e^{-\omega_c^2/2\beta} - d^2 e^{-\omega_c^2/2\beta} + \frac{1}{4\beta}\cos 2\omega_c d\right\}. \end{aligned} \tag{A.48}$$

Since

$$\sin x\cos y = \frac{1}{2}[\sin(x+y) + \sin(x-y)],$$

we have

$$F_2 = \beta\omega_c e^{-2\beta d^2}(u-d)e^{-2\beta u^2}(\sin 2\omega_c u + \sin 2\omega_c d).$$

From Eqs.(A.21) and (A.24), and the fact that $\int_{-\infty}^{\infty} x(t) = 0$ for $x(t)$ being an odd function of t, we obtain

$$\int_{-\infty}^{\infty} F_2\,du = \beta\omega_c e^{-2\beta d^2}\sqrt{\frac{\pi}{2\beta}}\left\{\frac{\omega_c}{2\beta}e^{-\omega_c^2/2\beta} - d\sin 2\omega_c d\right\}. \tag{A.49}$$

Similarly,

$$F_3 = \beta\omega_c e^{-2\beta d^2}(u+d)e^{-2\beta u^2}(\sin 2\omega_c u - \sin 2\omega_c d).$$

It follows that

$$\int_{-\infty}^{\infty} F_3\,du = \beta\omega_c e^{-2\beta d^2}\sqrt{\frac{\pi}{2\beta}}\left\{\frac{\omega_c}{2\beta}e^{-\omega_c^2/2\beta} - d\sin 2\omega_c d\right\}, \tag{A.50}$$

which is identical to the rsult given by Eq.(A.49).

The last term F_4 can be obtained by using the identity

$$\sin x \sin y = -\frac{1}{2}[\cos(x+y) - \cos(x-y)],$$

such that

$$F_4 = \omega_c^3 e^{-2\beta d^2} e^{-2\beta u^2} (\cos 2\omega_c d - \cos 2\omega_c u).$$

Therefore,

$$\int_{-\infty}^{\infty} F_4 \, du = \omega_c^2 e^{-2\beta d^2} \sqrt{\frac{\pi}{2\beta}} \left\{ \cos 2\omega_c d - e^{-\omega_c^2/2\beta} \right\}. \tag{A.51}$$

Finally, substitute Eqs.(A.48), (A.49), (A.50), and (A.51) into Eq.(A.47). Then, from Eq.(A.46), we obtain

$$\begin{aligned} J_{ij} &= J_{2k,2m} \\ &= \frac{a_k a_m A^2}{N_0} \sqrt{\frac{\pi}{2\beta}} e^{-2\beta d^2} \left\{ \beta(1 - 4\beta d^2)(\cos 2\omega_c d + e^{-\omega_c^2/2\beta}) \right. \\ &\quad \left. + 4\beta\omega_c d \sin 2\omega_c d + \omega_c^2 \cos 2\omega_c d \right\}, \end{aligned} \tag{A.52}$$

where $k, m = 1, 2, \ldots, K$.

In the special case that $m = k$, we have $\theta_i = \theta_j = t_k$ and $d = (t_k - t_m)/2 = 0$. Then, J_{ij} corresponds to the $(2k)$th diagonal element of $\mathbf{J}$ such that

$$J_{2k,2k} = \frac{a_k^2 A^2}{N_0} \sqrt{\frac{\pi}{2\beta}} \left\{ \omega_c^2 + \beta(1 + e^{-\omega_c^2/2\beta}) \right\}, \tag{A.53}$$

where $k = 1, 2, \ldots, K$. This result is identical to that acquired for the case of single-layer reflection as given in Eq.(A.33).

Case 3: $J_{ij} = J_{2k-1,2m}$ when $\theta_i = a_k$ and $\theta_j = t_m$

Substitution of $\theta_i = a_k$ and $\theta_j = t_m$ into Eq.(A.19) gives

$$\begin{aligned} J_{ij} &= \frac{2}{N_0} \int_{-\infty}^{\infty} \frac{\partial g(t; \mathbf{a}, \mathbf{t})}{\partial a_k} \frac{\partial g(t; \mathbf{a}, \mathbf{t})}{\partial t_m} \, dt \\ &= \frac{2a_m}{N_0} \int_{-\infty}^{\infty} s(t - t_k) \frac{\partial s(t - t_m)}{\partial t_m} \, dt \\ &= \frac{2a_m A^2}{N_0} \int_{-\infty}^{\infty} e^{-\beta(t-t_k)^2} \cos \omega_c (t - t_k) \times \end{aligned}$$

$$\left[2\beta(t-t_m)e^{-\beta(t-t_m)^2}\cos\omega_c(t-t_m)+\omega_c e^{-\beta(t-t_m)^2}\sin\omega_c(t-t_m)\right]dt$$

$$= \frac{4a_m\beta A^2}{N_0}\int_{-\infty}^{\infty} e^{-\beta[(t-t_k)^2+(t-t_m)^2]}(t-t_m)\cos\omega_c(t-t_k)\cos\omega_c(t-t_m)\,dt +$$

$$\frac{2a_m\omega_c A^2}{N_0}\int_{-\infty}^{\infty} e^{-\beta[(t-t_k)^2+(t-t_m)^2]}\cos\omega_c(t-t_k)\sin\omega_c(t-t_m)\,dt. \tag{A.54}$$

Let $d=\frac{1}{2}(t_k-t_m)$ and $u=t-d$. Then

$$J_{ij} = \frac{4a_m\beta A^2}{N_0}e^{-2\beta d^2}\int_{-\infty}^{\infty} e^{-2\beta u^2}(u+d)\cos\omega_c(u-d)\cos\omega_c(u+d)\,du +$$

$$\frac{2a_m\omega_c A^2}{N_0}e^{-2\beta d^2}\int_{-\infty}^{\infty} e^{-2\beta u^2}\cos\omega_c(u-d)\sin\omega_c(u+d)\,du.$$

By using trigonometeric identities, we can obtain

$$J_{ij} = \frac{4a_m\beta A^2}{N_0}e^{-2\beta d^2}\int_{-\infty}^{\infty} e^{-2\beta u^2}u\cos\omega_c(u-d)\cos\omega_c(u+d)\,du -$$

$$\frac{4a_m\beta d A^2}{N_0}e^{-2\beta d^2}\int_{-\infty}^{\infty} e^{-2\beta u^2}\cos\omega_c(u-d)\cos\omega_c(u+d)\,du +$$

$$\frac{a_m\omega_c A^2}{N_0}e^{-2\beta d^2}\int_{-\infty}^{\infty} e^{-2\beta u^2}\sin 2\omega_c u\,du +$$

$$\frac{a_m\omega_c A^2}{N_0}e^{-2\beta d^2}\sin 2\omega_c d\int_{-\infty}^{\infty} e^{-2\beta u^2}\,du$$

$$\stackrel{\text{def}}{=} I_1+I_2+I_3+I_4. \tag{A.55}$$

Note that the integrands of first and third terms, I_1 and I_3, in Eq.(A.55) are odd functions of u, therefore I_1 and I_3 are both equal to zero. By using the result in Eq.(A.44), we find that

$$I_2=\frac{2a_m\beta d A^2}{N_0}\sqrt{\frac{\pi}{2\beta}}\,e^{-2\beta d^2}(\cos 2\omega_c d+e^{-\omega_c^2/2\beta}).$$

The fourth term in Eq.(A.55), I_4, can be determined by using the result in Eq.(A.21), i.e.,

$$I_4=\frac{a_m\omega_c A^2}{N_0}\sqrt{\frac{\pi}{2\beta}}\,e^{-2\beta d^2}\sin 2\omega_c d.$$

Combining these results with Eq.(A.55) yields

$$J_{ij} = J_{2k-1,2m}$$

$$= \frac{a_m A^2}{N_0}\sqrt{\frac{\pi}{2\beta}}\,e^{-2\beta d^2}\left\{2\beta d(\cos 2\omega_c d+e^{-\omega_c^2/2\beta})+\omega_c\sin 2\omega_c d\right\}, \tag{A.56}$$

where $k, m = 1, 2, \ldots, K$.

For the case that $m = k$, it is obvious that $\theta_i = a_k$, $\theta_j = t_k$, and $d = (t_k - t_m)/2 = 0$. Accordingly, Eq.(A.56) becomes

$$J_{2k-1,2k} = 0, \qquad \text{for } k = 1, 2, \ldots, K. \tag{A.57}$$

Case 4: $J_{ij} = J_{2k,2m-1}$ when $\theta_i = t_k$ and $\theta_j = a_m$

For the case that $\theta_i = a_k$ and $\theta_j = t_m$, we have

$$\begin{aligned} J_{ij} &= \frac{2}{N_0}\int_{-\infty}^{\infty} \frac{\partial g(t;\mathbf{a},\mathbf{t})}{\partial t_k}\frac{\partial g(t;\mathbf{a},\mathbf{t})}{\partial a_m}\,dt \\ &= \frac{2a_k}{N_0}\int_{-\infty}^{\infty} \frac{\partial s(t-t_k)}{\partial t_k} s(t-t_m)\,dt. \end{aligned} \tag{A.58}$$

The analogy of Eq.(A.58) to Eq.(A.54) suggests that J_{ij} in Eq.(A.58) can be obtained simply by switching a_k with a_m and t_k with t_m, respectively, in Eq.(A.56). Accordingly, the quantity d in Eq.(A.56) should be replaced by $-d$, because d is related to t_k and t_m by equation $d = (t_k - t_m)/2$. This amounts to multiplying Eq.(A.56) by $-a_k/a_m$ such that

$$\begin{aligned} J_{ij} &= J_{2k,2m-1} \\ &= -\frac{a_k A^2}{N_0}\sqrt{\frac{\pi}{2\beta}}\, e^{-2\beta d^2}\left\{2\beta d(\cos 2\omega_c d + e^{-\omega_c^2/2\beta}) + \omega_c \sin 2\omega_c d\right\}, \end{aligned} \tag{A.59}$$

for $k, m = 1, 2, \ldots, K$.

Specially, when $m = k$, we have $\theta_i = t_k$, $\theta_j = a_k$, and $d = 0$. Then, Eq.(A.59) becomes

$$J_{2k,2k-1} = 0, \qquad \text{for } k = 1, 2, \ldots, K. \tag{A.60}$$

Therefore, all four different types of elements of matrix $\mathbf{J}$ can be now computed by Eq.(A.44), Eq.(A.52), Eq.(A.56) and Eq.(A.59), respectively.

A.3.2 Cramér-Rao Lower Bounds on $\hat{a}_k$'s and $\hat{t}_k$'s

Now that all the elements of the Fisher's information matrix, $\mathbf{J}$, have been determined, the CRLB on the estimators' errors are the diagonal elements of the matrix $\mathbf{\Gamma}$, the inverse of $\mathbf{J}$, which is also a $2K \times 2K$ matrix. Let Γ_{ij} be the ijth element of matrix $\mathbf{\Gamma}$. Since it is so defined that $\boldsymbol{\theta} = (a_1, t_1, a_2, t_2, \ldots, a_K, t_K)^T$, or $a_k = \theta_{2k-1}$ and $t_k = \theta_{2k}$ for $k = 1, 2, \ldots, K$, then, the CRLB on

the estimators, $\hat{a}_k$'s and $\hat{t}_k$'s, are given by the following inequalities,

$$\mathrm{Var}[\hat{a}_k] = \mathrm{Var}[\hat{\theta}_{2k-1}] \geq \Gamma_{2k-1,2k-1}, \qquad \text{for } k = 1, 2, \ldots, K; \tag{A.61}$$

and

$$\mathrm{Var}[\hat{t}_k] = \mathrm{Var}[\hat{\theta}_{2k}] \geq \Gamma_{2k,2k}, \qquad \text{for } k = 1, 2, \ldots, K. \tag{A.62}$$

Since the off-diagonal elements of $\mathbf{J}$ for multi-layer reflection are non-zero in general, the elements of $\mathbf{\Gamma}$ are related to J_{ij} in a complicated ways, thus, it is not feasible to express the CRLB in terms of the signal parameters explicitly as in the case for single-layer reflection (Eq.(A.36) and Eq.(A.37)). Instead, we investigate the behaviour of the CRLB in some special cases and give only the numerical solutions for the CRLB of general situation.

CRLB for Reflected Signals of Well Separated Arrivals

When the depth of each layer in the media is sufficiently large, the reflections from the different interfaces will all appear far apart in time, or, $d \gg 1$, where $d = (t_k - t_m)/2$ is the time difference between the kth and mth arrivals, as defined in Eq.(A.40). In such cases, the elements of matrix $\mathbf{J}$, J_{ij}'s, may be well approximated by taking $d \to \infty$.

The diagonal elements of $\mathbf{J}$, shown in Eq.(A.45) and Eq.(A.53), are given by

$$J_{2k-1,2k-1} = \frac{A^2}{N_0}\sqrt{\frac{\pi}{2\beta}}\,(1 + e^{-\omega_c^2/2\beta}), \tag{A.63}$$

and

$$J_{2k,2k} = \frac{a_k^2 A^2}{N_0}\sqrt{\frac{\pi}{2\beta}}\,\left\{\omega_c^2 + \beta(1 + e^{-\omega_c^2/2\beta})\right\}, \tag{A.64}$$

where $k = 1, 2, \ldots, K$.

The off-diagonal elements, $J_{2k-1,2k}$ and $J_{2k,2k-1}$, are given by Eq.(A.57) and Eq.(A.60) as

$$J_{2k-1,2k} = 0, \tag{A.65}$$

and

$$J_{2k,2k-1} = 0, \tag{A.66}$$

for $k = 1, 2, \ldots, K$.

Clearly, those elements of $\mathbf{J}$ that are given by Eq.(A.63), Eq.(A.64), Eq.(A.65), and Eq.(A.66) do not depend upon the time difference d, so that they are not affected when $d \to \infty$. On the other hand, the rest of the elements do depend upon d in general. Particularly, all four types elements of

J as given by Eq.(A.44), Eq.(A.52), Eq.(A.56) and Eq.(A.59) (except above special cases) contain a common factor $e^{2\beta d^2}$, and they will all vanish when d approaches infinity. In other word, all the off-diagonal elements of **J** become zero as $d \to \infty$. Therefore, the Fisher's information matrix in such a case is a diagonal matrix, with its diagonal elements given by Eq.(A.63) and Eq.(A.64).

As a result, the Cramér-Rao Lower Bounds on the estimation errors, $\mathrm{Var}[\hat{\theta}_i]$'s, for the multi-layer reflection with well separated arrivals, can be written simply as the inverse of J_{ii}'s such that

$$\mathrm{Var}[\hat{\theta}_i] \geq 1/J_{ii}, \qquad \text{for } i = 1, 2, \ldots, 2K.$$

Or, more specifically,

$$\mathrm{Var}[\hat{a}_k] \geq \frac{N_0}{A^2}\sqrt{\frac{2\beta}{\pi}}\,(1 + e^{-\omega_c^2/2\beta})^{-1}, \tag{A.67}$$

$$\mathrm{Var}[\hat{t}_k] \geq \frac{N_0}{a_k^2 A^2}\sqrt{\frac{2\beta}{\pi}}\left[\omega_c^2 + \beta\,(1 + e^{-\omega_c^2/2\beta})\right]^{-1}, \tag{A.68}$$

for $k = 1, 2, \ldots, K$. The results here are identical to those given in Eq.(A.34) and Eq.(A.35) for the single-layer reflection. The lower bounds on $\mathrm{Var}[\hat{a}_k]$ and $\mathrm{Var}[\hat{t}_k]$ depend upon only the parameters of the probing radar pulse and the parameters associated with the kth layer. There is no interdependence between the parameters of different layers. This result is in accordance with our intuition, since the estimation of the parameters of different layers should not interfere with each other if the layers in the media are well separated.

Suppose that the ℓth arrival is the weakest one in the reflected radar signal consisting of multiple returns. The signal-to-noise ratio ρ, measured with respect to the weakest arrival, is defined as

$$\rho = \rho_\ell = \frac{a_\ell^2 A^2}{N_0}\sqrt{\frac{\pi}{2\beta}}\,(1 + e^{-\omega_c^2/2\beta}).$$

Then, the inequalities in Eq.(A.67) and Eq.(A.68) may be rewritten, respectively, as

$$\mathrm{Var}[\hat{a}_k] \geq \rho^{-1} a_\ell^2, \tag{A.69}$$

$$\mathrm{Var}[\hat{t}_k] \geq \rho^{-1}\left(\frac{a_\ell}{a_k}\right)^2 \frac{1 + e^{-\omega_c^2/2\beta}}{\omega_c^2 + \beta\,(1 + e^{-\omega_c^2/2\beta})}, \tag{A.70}$$

for $k = 1, 2, \ldots, K$. If the CRLB's are plotted as $\mathrm{Var}[\hat{a}_k]/a_\ell^2$ and $\mathrm{Var}[\hat{t}_k]/(a_k/a_\ell)^2$, they

CRLB for Reflected Signals of Closely Spaced Arrivals

When the layers in the media are very shallow, the reflections from the adjacent interfaces will be very closely spaced in time, or $d = (t_k - t_m)/2 \ll 1$. In this section, we study the limiting case of

the Fisher's information matrix $\mathbf{J}$ as d approaches zero.

As addressed above, the diagonal elements of $\mathbf{J}$, $J_{2k-1,2k-1}$ and $J_{2k,2k}$, as given by Eq.(A.63) and Eq.(A.64) respectively, are independent of d, so that they are not affected when d varies. The off-diagonal elements of $\mathbf{J}$, however, all depend upon d in general, thus they will undoubtedly be affected as d decreases. From Eq.(A.44), Eq.(A.52), Eq.(A.56), and Eq.(A.59), it is straightforward to calculate their limits, which are found to be as following.

$$\lim_{d\to 0} J_{2k-1,2m-1} = \frac{A^2}{N_0}\sqrt{\frac{\pi}{2\beta}}(1+e^{-\omega_c^2/2\beta}) = \frac{2E_s}{N_0}, \tag{A.71}$$

$$\lim_{d\to 0} J_{2k,2m} = \frac{a_k a_m A^2}{N_0}\sqrt{\frac{\pi}{2\beta}}\left\{\omega_c^2+\beta(1+e^{-\omega_c^2/2\beta})\right\} = \frac{2a_k a_m}{N_0}E_t, \tag{A.72}$$

$$\lim_{d\to 0} J_{2k-1,2m} = 0, \tag{A.73}$$

$$\lim_{d\to 0} J_{2k,2m-1} = 0, \tag{A.74}$$

where $k, m = 1, 2, \ldots, K$, and E_s and E_t are defined as

$$\begin{aligned} E_s &= \frac{A^2}{2}\sqrt{\frac{\pi}{2\beta}}(1+e^{-\omega_c^2/2\beta}), \\ E_t &= \frac{A^2}{2}\sqrt{\frac{\pi}{2\beta}}\left\{\omega_c^2+\beta(1+e^{-\omega_c^2/2\beta})\right\}. \end{aligned} \tag{A.75}$$

Note that the diagonal elements may also be calculated by Eq.(A.71) and Eq.(A.72) as they give the exactly same results as Eq.(A.63) and Eq.(A.64), respectively.

Nevertheless, the inverse of the Fisher's information matrix $\boldsymbol{\Gamma}$ does not exist because $\mathbf{J}$ becomes singular as $d \to 0$. To demonstrate this singularity, we take the reflection from a two-layer media ($K = 2$) as an example. From Eq.(A.71), Eq.(A.72), Eq.(A.73), and Eq.(A.74), the associated 4×4 matrix $\mathbf{J}$ can be expressed as

$$\mathbf{J} = \frac{2}{N_0}\begin{pmatrix} E_s & 0 & E_s & 0 \\ 0 & a_1^2 E_t & 0 & a_1 a_2 E_t \\ E_s & 0 & E_s & 0 \\ 0 & a_1 a_2 E_t & 0 & a_2^2 E_t \end{pmatrix}. \tag{A.76}$$

Obviously, the first and third columns, the second and fourth columns are linearly dependent, respectively. Consequently, matrix $\mathbf{J}$ is deficient in rank, i.e., singular.

The singularity of the Fisher's information matrix implies that the estimation of the parameters, a_k's and t_k's, will be highly inaccurate or unreliable if the difference between the arriving times of the radar returns, d, becomes sufficiently small. This dependence of the estimation accuracy on d is illustrated in Fig. A.3 and Fig. A.2, where the case $K = 2$ is taken as an example, and the CRLB's on $\mathrm{Var}[\hat{a}_2]/a_2^2$ and $\mathrm{Var}[\hat{t}_2]$ (the weaker return) versus the time difference $\Delta t = t_2 - t_1$ are plotted for different levels of SNR.

They clearly show that, for Δt greater than about 0.8 ns, the minimum attainable variances of $\hat{a}_2$ and $\hat{t}_2$ displays very little change, but they increase, though not monotonically, when Δt is smaller than 0.8 ns and decreases. A very revealing feature, common to both Fig. A.2 and Fig. A.3, is that there is a drastic increase of the CRLB's, regardless of the SNR level, as Δt approaches certain point Δt_c, far before it actually reduces to zero. The value of this critical point is $\Delta t_c \approx 0.35$ ns, approximately 30 percent of the pulse-width (main lobe) of the probing radar signal $s(t)$. The surge of the lower bounds suggests that it is practically impossible to resolve any two arrivals if their time difference Δt is below Δt_c.

Figure A.4 depicts the reflected signals consisting of two returns, except the waveform (a), which contains only one return and is plotted as a reference. For the rest, the signal parameters are $t_1 = 5.0$ ns, $a_1 = 0.5$, $a_2 = 0.1$, and t_2 is so chosen that Δt varies from 0.34 to 0.40 ns. Despite the resemblance among these waveforms, their behaviour will differ substantially in terms of the accuracy of resulting parameter estimates, according to the analysis of CRLB. The estimation of the two arrivals in the waveform (b), on the one hand, is bound to fail even at high SNR level; and on the other hand, the returns in (c) and (d) can be expected to lead to a reasonably accurate estimation, provided that an appropriate estimation technique is employed.

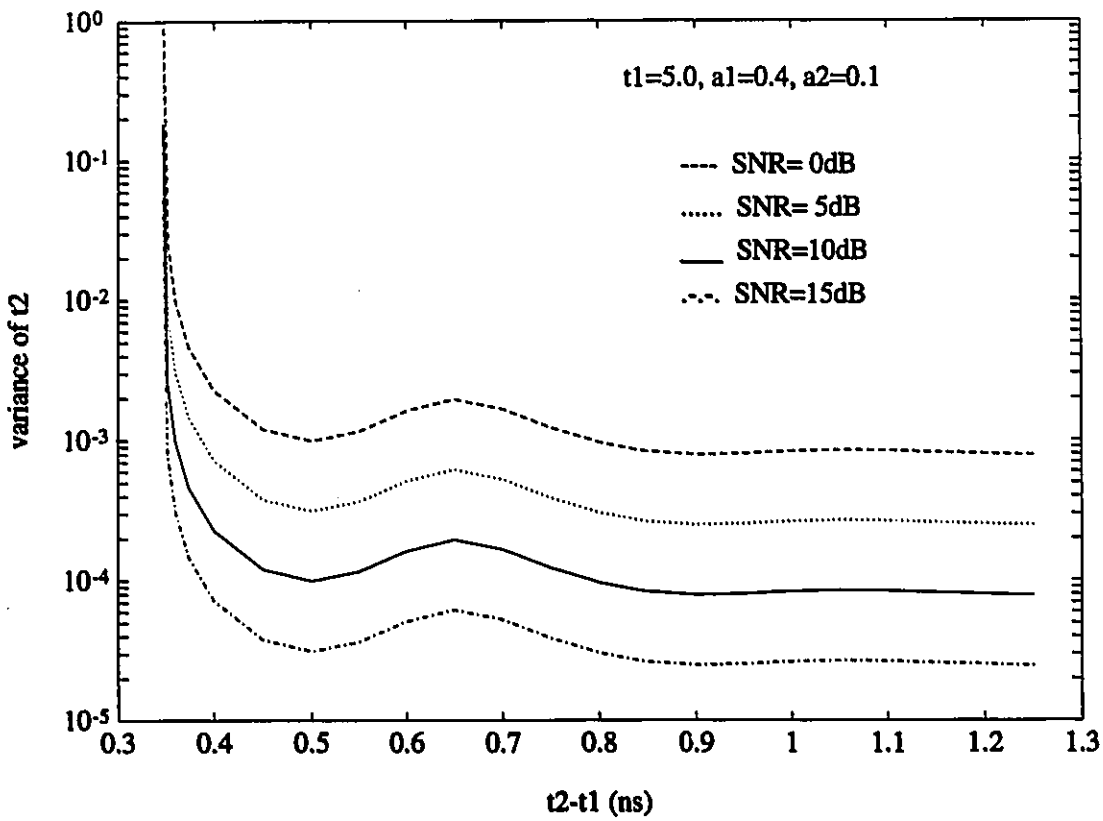

Figure A.2: Dependency of CRLB's upon $\Delta t = t_2 - t_1$: (a) CRLB on $\mathrm{Var}[\hat{t}_2]$.

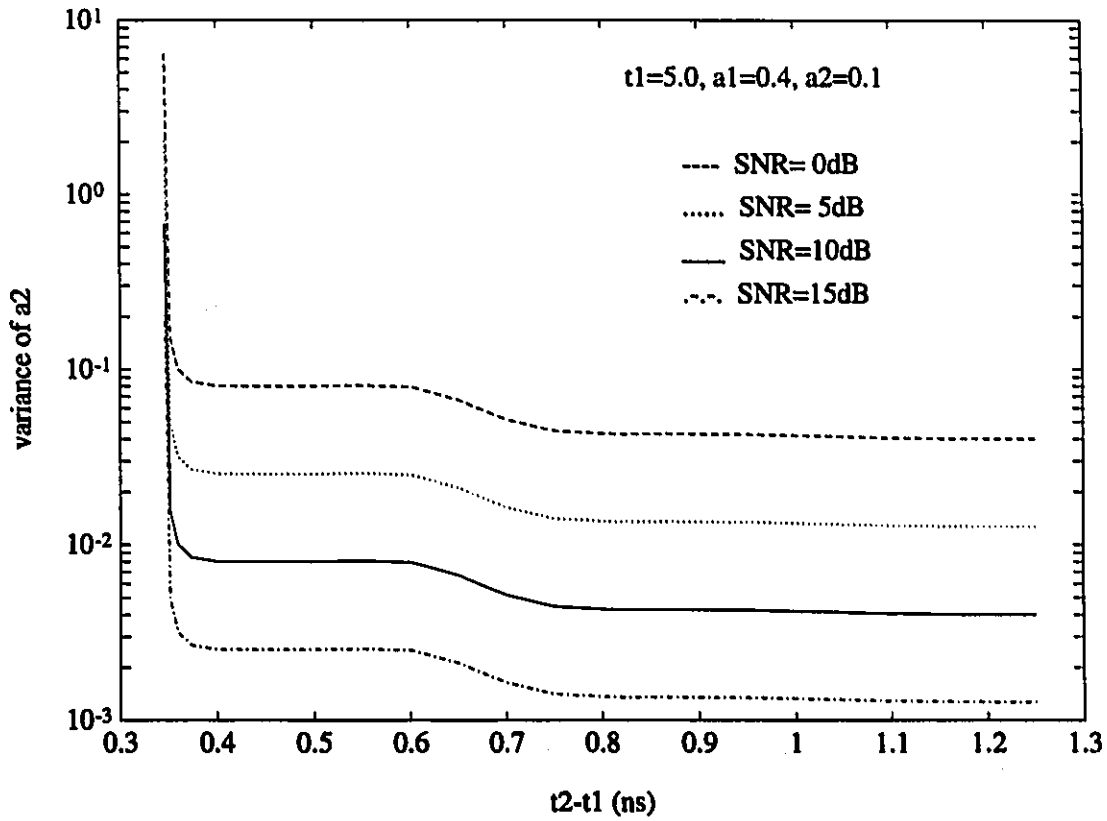

Figure A.3: Dependency of CRLB's upon $\Delta t = t_2 - t_1$: (b) CRLB on $\mathrm{Var}[\hat{a}_2]/a_2^2$.

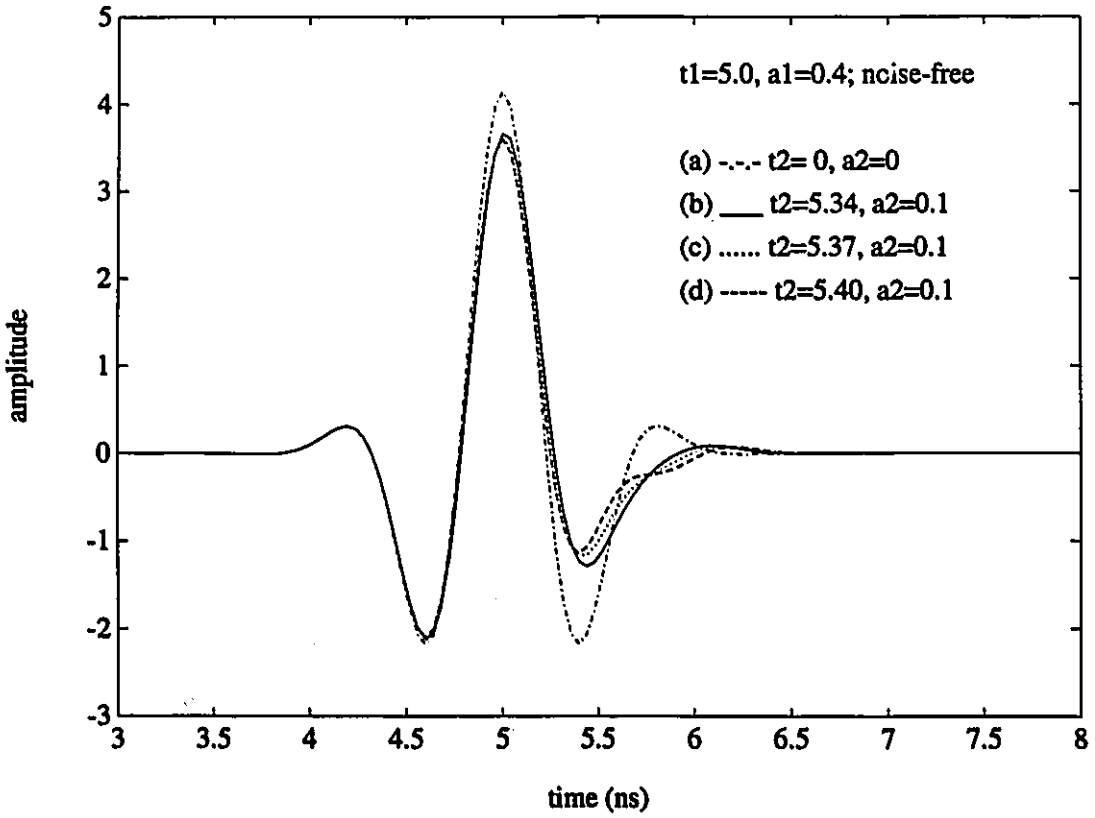

Figure A.4: Reflected signals with two closely spaced arrivals.

Bibliography

ARYA, V. K.; and Holden, H. D. (1987), "Deconvolution of Seismic Data — An Overview," *IEEE Trans. Geosci. Elec.*, Vol. GE-16, No. 2, April 1978, pp. 95–98.

BHASKAR, D. RAO; and Hari, K. V. S. (1989), "Performance Analysis of Root-MUSIC," *IEEE Trans. ASSP*, Vol. 37, No. 12, December 1989, pp. 1939–1949.

BERES, M.; and Haeni, F. P. (1991), "Application of Ground-Penetrating-Radar Methods in Hydrogeological Studies," *Ground Water*, Vol. 29, No. 3, May-June 1991, pp. 375–386.

BURRELL, G. A.; and Peters, L. (1979), "Pulse Propagation in Lossy Media Using the Low-Frequency Window for Video Pulse Radar Application," *Proc. IEEE*, Vol. 67, No. 7, July 1979, pp. 981–990.

CALDECOTT, R.; Poirier, M.; Scofea, D.; Svoboda, D. E.; and Terzuoli, A. J. (1988), "Underground Mapping of Utility Lines Using Impulse Radar," *IEE Proc.*, Vol. 135, Pt. F, No. 4, August 1988, pp. 343–353.

CARTER, C. R.; Chung, T.; Holt, F. B.; and Manning, D. G. (1986), "An Automated Signal Processing System for the Signature Analysis of Radar Waveform from Bridge Deck," *Can. Elec. Eng. J.*, Vol. 11, No. 3, 1986, pp. 128–137.

CHAN, L. C.; Moffatt, D. L.; and Peters, L. (1979), "A Characterization of Subsurface Radar Targets," *Proc. IEEE*, Vol. 67, No. 7, July 1979, pp. 991–1000.

CHEN, C. T. (1970), *Introduction to Linear System Theory*, Holt, New York, 1970.

CHENG, DAVID, K. (1989), *Field and Wave Electromagnetics*, 2nd Edition, Addison-Wesley, Reading, Massachusetts, 1989.

CHUNG, T.; Carter, C. R.; Masliwec, T.; and Manning, D. G. (1992), "Impulse Radar Evaluation of Asphalt-Covered Bridge Decks," *IEEE Trans. Aerospace and Elec. Systems*, Vol. 28, No. 1, January 1992, pp. 125–137.

DANIELS, D. J. (1980), "Short Pulse Radar for Stratified Lossy Dielectric Layer Measurement," *IEE Proc.*, Vol. 127, Pt. F, No. 5, October 1980, pp. 384–388.

DANIELS, D. J.; Gunton, D. J.; and Scott, H. F. (1988), "Introduction to Subsurface Radar," *IEE Proc.*, Vol. 135, Pt. F, No. 4, August 1988, pp. 278–320.

DELAUDER, D. M.; and Constantine, A. B. (1982), "Microwave Short-Pulse Generator for Bed-Level Detection," *IEEE Trans. Instrumentation and Measurement*, Vol. IM-31, No. 4, December 1982, pp. 274–278.

EVENS, J. E.; Johnson, J. R.; and Sun, D. F. (1981), "High Resolution Angular Spectrum Estimation Techniques for Terrain Scattering Analysis and Angle of Arrival Estimation," *Proc. 1st ASSP Workshop Spectral Estimation*, Hamilton, Ont., Canada, 1981, pp. 134–139.

FOKKEMA, J. T.; and Ziolkowski, A. (1987), "The Critical Reflection Theorem," *Geophysics*, Vol. 52, No. 7, July 1987, pp. 965–972.

GOLDBERG, D. E. (1989), *Genetic Algorithm in Search, Optimization and Machine learning*, Addison-Wesley, Reading, Massachusetts, 1989.

GOLUB, GENE H.; and Van Loan, Charles F. (1990), *Matrix Computations*, 2nd Edition, The John Hopkins University Press, Baltimore, Maryland, 1990.

GRADSHTEYN, I. S.; and Ryzhik, I. M. (1965), *Tables of Integrals, Series, and Products*, Academic Press, New York, 1965.

HAYKIN, SIMON (1991), *Adaptive Filter Theory*, 2nd Edition, Prentice-Hall, Englewood Cliffs, New Jersey, 1991.

HAYKIN, SIMON (1983), *Communication Systems*, 2nd Edition, John Wiely & Sons, New York, 1983.

IIZUKA, KEIGO (1984), "Subsurface radar," in *Noise and Clutter Rejection in Radars and Imaging Sensors*, Musha, T.; Suzuki, T.; and Ogura, H., Ed., *Proc. of the 1984 International Symposium on Noise and Clutter Rejection in Radars and Imaging Sensors*, IECE, Tokyo, Japan, October 1984,

pp. 15–24.

IMSL INC. (1990), *IMSL Math/Library User's Manual*, Volume 3, IMSL Inc., Houston, Texas, 1990.

JUSTICE, J. H. (1985), "Array Processing in Exploration Seismology," in *Array Signal Processing*, Haykin, S., Ed., Prentice-Hall, Englewood Cliffs, New Jersey, 1985.

JURKEVIS, A.; and Wiggins, R. (1984), "A Critique of Seismic Deconvolution," *Geophysics*, Vol. 49, No. 12, December 1984, pp. 2109–2116.

KAILATH, THOMAS (1980), *Linear Systems*, Prentice-Hall, Englewood Cliffs, New Jersey, 1980.

KENDALL, MAURICE G.; and Stuart, Allen (1973), *The Advanced Theory of Statistics, Volume 2: Inference and Relationship*, 3rd Edition, Charles Griffin, London, 1973.

KIRKPATRICK, S.; Gelatt, C. D.; and Vecchi, M. P. (1983), "Optimization by Simulated Annealing," *Science*, Vol.220, No. 4598, May 13, 1983, pp. 671–680.

KRAUS, D. J. (1991), *Electromagnetics*, 4th Edition, McGraw-Hill, New York, 1991.

LAARHOVEN, J. P. M. VAN; and Aarts, E. H. L. (1987), *Simulated Annealing: Theory and Applications*, D. Reidel, Boston, Masssachusetts, 1987.

LANCASTER, PETER (1985), *The Theory of Matrices with applications*, 2nd Edition, Academic Press, Orlando, Florida, 1985.

LEGGO, P. J. (1982), "Geological Application of Ground Impulse Radar," *Trans. Inst. Mining and Metallurgy*, Section B, Applied Earth Sciences, Vol. 91, February 1982, pp. B1–B5.

LEHMANN, E. L. (1983), *Theory of Point Estimation*, John Wiley & Sons, New York, 1983.

MARPLE, S. L. (1987), *Digital Spectral Analysis with Applications*, Prentice-Hall, Englewood Cliffs, New Jersey, 1987.

MCCANN, D. M.; Jackson, P. D.; and Fenning, P. J. (1988), "Comparison of the Seismic and Ground Probing Radar Methods in Geological Surveying," *IEE Proc.*, Vol.135, Pt. F, No. 4, August 1988, pp. 380–390.

MENDEL, JERRY M. (1983), *Optimal Seismic Deconvolution: an Estimation-Based Approach*, Aca-

demic Press, New York, New York, 1983.

MENDEL, JERRY M. (1986), "Some Modeling Problems in Reflection Seismology," *IEEE ASSP Magazine*, April 1986, pp. 4–17.

MENDEL, JERRY M.; and Habibi-Ashrafi, F. (1980), "A Survey of Approaches to Solving Inverse Problems for Lossless Layered Media Systems," *IEEE Trans. Geoscience and Remote Sensing*, Vol. GE-18, No. 4, October 1980, pp. 320–330.

MOFFATT, D. L.; and Puskar, R. J. (1979), "A Subsurface Electromagnetic Pulse Radar," *Geophysics*, Vol. 41, No. 3, June 1976, pp. 506–518.

NICKEL, U. (1987), "Angular Superresolution with Phased Array Radar: a Review of Algorithms and Operational Constrains," *IEE Proc.*, Vol. 134, Pt. F, No. 1, February 1987, pp. 53–59.

OPPENHEIM, A. V.; and Schafer, R. W. (1975), *Digital Signal Processing*, Prentice-Hall, Englewood, Cliffs, New Jersey, 1975.

OSWALD, G. K. A. (1988), "Geophysical Radar Design," *IEE Proc.*, Vol. 135, Pt. F, No. 1, August 1988, pp. 317–379.

PAPOULIS, A. (1984), *Probability, Random Variables, and Stochastic Process*, 2nd Edition, McGraw-Hill, New York, 1984.

PAPOULIS, A. (1977), *Signal Analysis*, McGraw-Hill, New York, 1977.

PEACOCK, K. L.; and Treitel, S. (1969), "Predictive deconvolution: Theory and Practice," *Geophysics*, Vol. 34, No. 2, April 1969, pp. 155–169.

PILLAI, S. U.; and Kwong, B. H. (1989), "Forward/Backward Spatial Smoothing Techniques for Coherent Signal Identification," *IEEE Trans. ASSP*, Vol. 37, No. 1, January 1989, pp. 8–15.

POZAR, DAVID M. (1990), *Microwave Engineering*, Addison-Wesley, Reading, Massachusetts, 1990.

REDDI, SEENU S. (1987), "On a Spatial Smoothing Technique for Multiple Source Location," *IEEE Trans. ASSP*, Vol. ASSP-35, No. 5, May 1987, pp. 709.

ROBINSON, ENDERS A. (1957), "Predictive Decomposition of Seismic Traces," *Geophysics*, Vol. 22, No. 4, October 1957.

ROBINSON, ENDERS A. (1980), *Geophysical Signal Analysis*, Prentice-Hall, Englewood Cliffs, New Nersey, 1980.

ROBINSON, ENDERS A. (1984a), *Seismic Inversion and Deconvolution, Part A: Classical Methyods*, Geophysical Press, London, 1984.

ROBINSON, E. A. (1984b), "Statistical Pulse Compression," *Proc. IEEE*, Vol. 72, No. 10, October 1984, pp. 1276–1289.

SCHMIDT, RALPH O. (1986), "Multiple Emitter Location and Signal Parameter Estimation," *IEEE Trans. AP*, Vol. ASSP-34, No. 3, March 1986, pp. 276–280.

SHAN, T.J.; Wax, M.; and Kailath, T. (1985), "On Spatial Smoothing for Direction-of-Arrival Estimation of Coherent Signals," *IEEE Trans. ASSP*, Vol. ASSP-33, No. 4, August 1985, pp. 806–811.

SILVIA, M. T.; and Robinson, E. A. (1979), *Deconvolution of Geophysical Time Series in the Exploration for Oil and Natural Gas*, Elsevier, Armsterdam, 1979.

STEINBERG, BERNARD D. (1976), *Principles of Aperture and Array System Design*, John Wiley & Sons, New York, 1976.

STOICA, PETRE; and Nehorai, Arye (1989), "MUSIC, Maximum Likelihood, and Cramer-Rao Bound," *IEEE Trans. ASSP*, Vol. 37, No. 5, May 1989, pp. 720–741.

ULRIKEN, C. PETER F. (1983), *Application of Impulse Radar to Civil Engineering*, Doctoral Thesis, Lund University of Technology, Lund, Sweden, 1983.

VAN TREES, HARRY L. (1968), *Detection, Estimation, and Modulation Theory, Part I: Detection, Estimation, and Linear Modulation Theory*, John Wiley & Sons, New York, 1968.

VELLIDIS, G.; Smith, M. C.; Thomas, D. L.; and Asmussen, L. E. (1990), "Detecting Wetting Front Movement in a Sandy Soil with Ground-Penetrating Radar," *Trans. American Society of Agriculture Engineers*, Vol. 33(6), November/December 1990, pp. 1867–1874.

WADSWORTH, G. P.; Robinson, E. A.; Bryan, J. G.; and Hurley, P. M. (1953), "Detection of Reflections on Seismic Records by Linear Operators," *Geophysics*, Vol. 18, No. 3, July 1953.

WALDEN, A. T.; and Hosken, J. W. J. (1985), "An Investigation of the Spectral Properties of

Primary Reflection Coefficients," *Geophysical Prospecting*, Vol. 33, 1985, pp. 400–435.

WALDEN, A. T.; and White, R. (1988), "Discussion on 'The Critical Reflection Theorem' by Fokkema and Ziolkowski," *Geophysics*, Vol. 53, No. 11, November 1988, pp. 1490–1491.

WANG, R. J. (1969), "The Determination of Optimal Gate Length for time-varying Wiener Filtering," *Geophysics*, Vol. 34, No. 5, May 1969, pp. 683–695.

WAX, MATI; and Kailath, Thomas (1985), "Detection of Signals by Information Theoretic Criteria," *IEEE Trans. ASSP*, Vol. ASSP-33, No. 2, April 1985, pp. 387–392.

WAX, MATI; and Ziskind, Ilan (1989), "Detection of the Number of Coherent Signals by the MDL Principle," *IEEE Trans. ASSP*, Vol. 37, No. 8, August 1989, pp. 1190–1196.

WONG, K. M.; Walker, R. S.; and Niezgoda, G. (1988), "Effects of Random Sensor Motion on Bearing Estimation by the MUSIC Algorithm," *IEE Proc.*, Vol. 135, Pt. F, No. 3, June 1988, pp. 233–249.

WONG, K. M.; Reilly, J. P.; Wu, Q.; and Qiao, S. (1992), "Estimation of the Directions of Arrival of Signals In Unknown Correlated Noise, Part I: The MAP Approach and its Implementation," *IEEE Trans. SP*, Vol. 40, No. 8, August 1992, pp. 2007–2017.

ZACK, SHELEMYAHU (1971), *The Theory of Statistical Inference*, John Wiley & Sons, New York, 1971.